CALT-68-1150

A STUDY OF THE $\psi''(3770)$ USING THE CRYSTAL BALL DETECTOR

Thesis by

Richard Allan Partridge

In Partial Fulfillment of the Requirements

for the Degree of

Doctor of Philosophy

California Institute of Technology

Pasadena, California

1984

(submitted February 8, 1984)

ABSTRACT

The properties of the $\psi''(3770)$ were studied by an experiment performed at the SPEAR e^+e^- colliding beam facility using the Crystal Ball detector. The unique abilities of the Crystal Ball, a highly segmented NaI detector that specializes in precisely measuring the energy and direction of photons, were used to make several new measurements.

The hadron cross section was measured at 23 different center of mass energies in the vicinity of the ψ''. The ψ'' is clearly visible as a peak in the cross section near E_{cm}=3770 MeV. The ψ'' resonance parameters were determined by fitting a modified Breit-Wigner line shape to the observed hadron cross section. The ψ'' mass, partial width to e^+e^-, and total width were measured to be 3768±5 MeV, 283±70 eV, and 34±8 MeV, respectively.

The inclusive photon spectrum of the ψ'' was examined for structure. Narrow peaks were observed in the spectrum due to the radiative production of ψ and ψ' mesons. The integrated hadron cross sections were measured to be 16±5 nb-GeV and 5.2±1.7 nb-Gev for the ψ and ψ', respectively. No other statistically significant structure was observed.

The decays of the ψ'' were used to search for D^0 mesons decaying into four-photon and six-photon final states. No evidence for these decays was found, and the following branching ratio limits were set (90% CL): $BR(D^0\to\pi^0\pi^0)<0.28\%$, $BR(D^0\to\eta\pi^0)<0.74\%$, $BR(D^0\to\eta\eta)<1.0\%$, $BR(D^0\to\pi^0\pi^0\pi^0)<1.6\%$, $BR(D^0\to\eta\pi^0\pi^0)<6.6\%$, and $BR(D^0\to\bar{K}^0\pi^0)<7.6\%$.

ACKNOWLEDGMENTS

It might be said that I took the scenic route through graduate school. After many twists and turns, a few detours, and one or two U-turns, I have finally come to the end of the road. I am deeply indebted to my friends, family, and colleagues for their patience and support along the way.

This thesis could not have been written without the hard work and dedication of my colleagues on the Crystal Ball: Dikran Antreasyan, David Aschman, Elliott Bloom, Fatin Bulos, Toby Burnett, Matteo Cavalli-Sforza, Ron Chestnut, Ray Cowan, Don Coyne, Chad Edwards, John Gaiser, David Gelphman, Gary Godfrey, Roland Horisberger, Bob Hofstadter, Achim Irion, Chris Kiesling, Ian Kirkbride, Herman Kolanoski, Wolf Kollman, Kay Königsmann, Roger Lee, Art Liberman, Bill Lockman, Cathy Newman-Holmes, Mark Oreglia, Jack O'Reilly, Al Osterheld, Charlie Peck, Brian Pollock, Frank Porter, Peter Ratoff, Mark Richardson, Hartmut Sadrozinski, Karl Strauch, John Tompkins, Klaus Wacker, and Alan Weinstein. Not only did these people do a superb job of building and running the experiment, they also provided a friendly and helpful environment that was a pleasure to be part of. Thank you one and all!

Special thanks go to Charlie Peck for teaching me the technique and joy of experimental physics, directing my research, allowing me to explore alternatives to a career in physics, and showing extraordinary patience with me over the years. I would also like to give special

thanks to Frank Porter for his generous contributions of advice and help.

I feel very lucky to have received so much support and encouragement from my friends and family during my long career as a graduate student. Their contribution to this thesis was substantial, albeit indirect. My deepest gratitude and appreciation are reserved for Kathryn Green; her love, companionship, and many sacrifices will always be remembered.

This research was made possible by the generous support of Caltech, SLAC, and the Department of Energy.

CONTENTS

LIST OF TABLES

LIST OF FIGURES

Chapter I

INTRODUCTION

The discovery of the $\psi(3095)$ in 1974 revealed the existence of an entirely new regime of particle physics.[1] At the time of its discovery, the ψ was unique in having a very large mass and an extremely narrow width. Since then several other states have been found with similar properties: the $\psi'(3684)$,[2] $\chi_0(3415)$,[3] $\chi_1(3510)$,[4] $\chi_2(3555)$,[5] $\eta_c(2980)$,[6] and $\eta_c'(3590)$.[7] These states are presumably close relatives since they have similar masses, narrow widths, and make radiative transitions from one to another as shown in figure 1.[8]

A very successful theory which explains the existence and properties of these states is the "charmonium theory."[9] This theory presumes the existence of a new kind of quark, the "charmed quark," which is heavy and carries a new quantum number, "charm."[10] The charmonium theory predicts the existence of bound states in which the strong interaction binds a charm quark and a charm antiquark together. These states will be isosinglets with a net charm quantum number of 0. There is a strong parallel between these charmonium bound states and those of the positronium system. In particular, the spectroscopy of the charmonium states should be qualitatively similar to the spectroscopy of the positronium system. Thus, charmonium is expected to have both a spin triplet and a spin singlet ground state, as well as orbital and radial excitations of the ground states.[11]

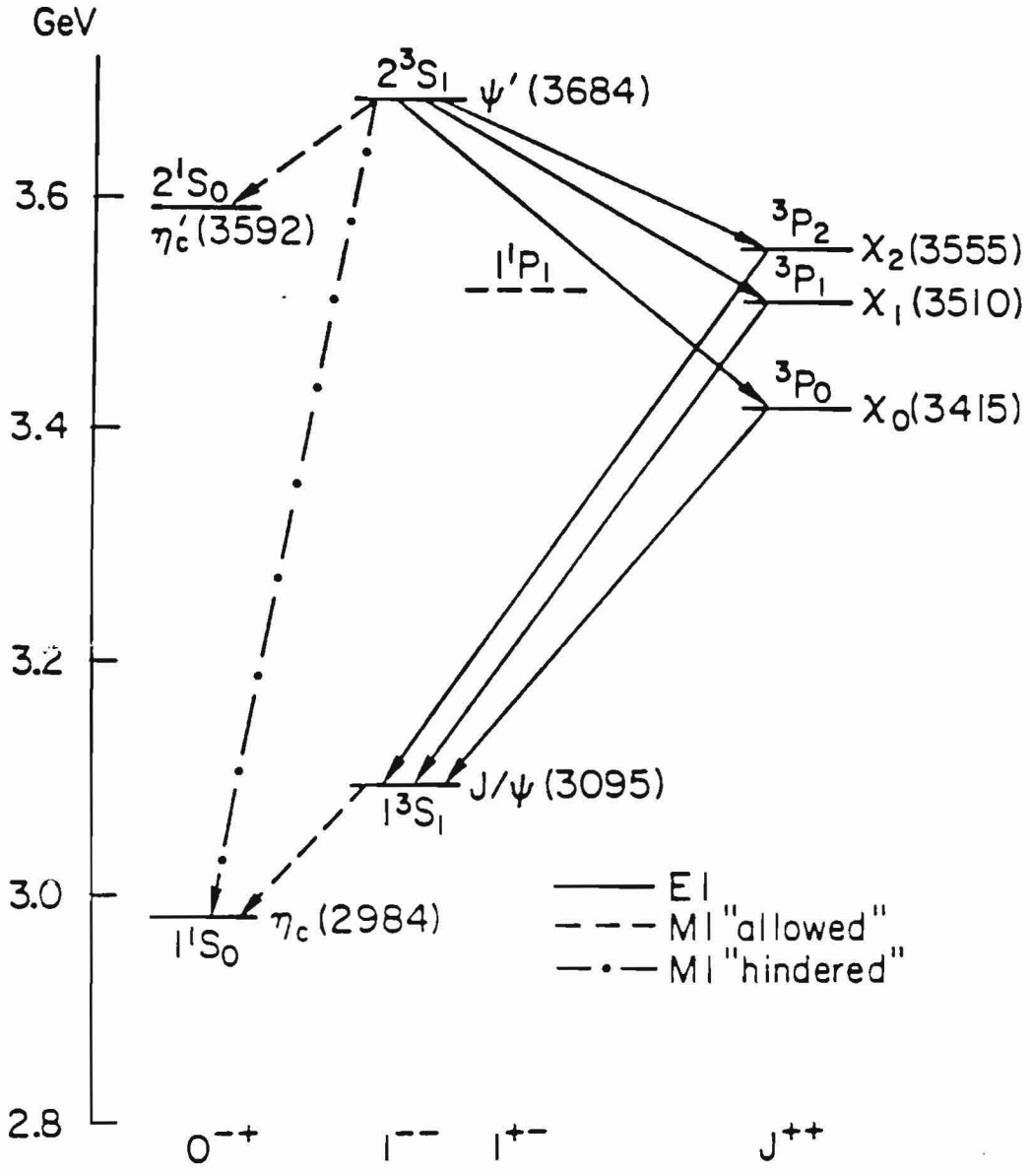

Figure 1: Spectroscopy of the charmonium system.

The spectroscopy of charmonium states below charm threshold is shown, including all radiative transitions that have been observed. Note that the 1^1P_1 state has not yet been discovered.

The most striking features of the ψ are its large mass and narrow width. These and other properties of the ψ are explained if it is "orthocharmonium," the spin triplet (1^3S_1) ground state of charmonium. In the charmonium theory, the mass of the ψ comes mostly from the rest mass of the charmed quarks. This implies that the charm quark mass is $\approx$1.5 GeV, which agrees with early expectations that it would be a "few GeV."[12] The narrow width of the ψ is explained by the "OZI rule,"[13] which says that hadronic decays are strongly suppressed when the quarks of the initial state do not appear in the final state. Since the ψ is below threshold for a final state containing the charm quarks (i.e., below the $D\bar{D}$ threshold at E_{cm}=3727 MeV), the OZI rule will suppress the hadronic decay modes of the ψ. This suppression accounts for the extremely narrow width of the ψ relative to typical hadronic widths.

The discovery of the ψ' shortly after the ψ was discovered aroused the suspicion that there might be many of these new states to be found. The ψ' has properties very similar to the ψ, and was quickly recognized as a likely candidate for the first radial excitation of the ψ (2^3S_1). From the first orbital excitation of the ψ, the charmonium theory predicts the existence of 1^3P_0, 1^3P_1, and 1^3P_2 states. The χ_0, χ_1, and χ_2 have the expected properties for the 1^3P_0, 1^3P_1, and 1^3P_2 states, respectively. The η_c is a candidate for "paracharmonium," the spin singlet ground state (1^1S_1), and the η_c' is a candidate for the first radial excitation of the η_c (2^1S_1). The only bound state predicted but not yet found is the first orbital excitation of the η_c (1^1P_1), which is expected to be very difficult to find.

Charmonium states with masses greater than 3727 MeV are above threshold for OZI allowed decay modes. This threshold is determined by twice the mass of the charmed D mesons.[14] The $D^0(1863)$ is composed of a charm quark and an up antiquark, giving it a net charm quantum number of 1. The isodoublet partner of the D^0 is the $D^+(1868)$, which has a down antiquark instead of an up antiquark. The decay of a charmonium state into $D\bar{D}$ is allowed by the OZI rule since the charm quarks of the initial state appear in the final state. Charmonium states above $D\bar{D}$ threshold should decay predominantly into OZI allowed final states and have a significantly larger width than those below threshold.

Four such broad states have been observed[15,16]: the $\psi''(3770)$, $\psi(4030)$, $\psi(4160)$, and $\psi(4415)$. Like the ψ and ψ', these states are observed as resonances in the cross section $\sigma(e^+e^-\rightarrow\text{hadrons})$. As expected, these states have much larger widths than the charmonium states below $D\bar{D}$ threshold. The narrowest one, the ψ'', is more than 100 times as wide as the ψ', although the masses are only 85 MeV apart. The properties of the ψ'' are the focus of the remainder of this thesis.

To better understand how these broad states fit into the charmonium theory requires a quantitative model for the charmonium system. Such a model can be devised by inventing a potential for the interaction between a charm quark and a charm antiquark. The Schrödinger equation is then solved for the wave function of the charmonium state. This results in predictions of the charmonium mass splittings (neglecting the spin dependent hyperfine splitting), leptonic widths, and radiative transition rates.

The choice of a potential is somewhat arbitrary because the strong interaction is not well understood. A potential consisting of a Coulombic interaction term and a linear confinement term has been thoroughly studied.[17] This model has three parameters: the charm quark mass, the strength of the Coulombic potential, and the strength of the linear potential. These parameters were adjusted to yield the observed bound state mass splittings and the observed leptonic width of the ψ. This set of parameters gives a charm quark velocity which is reasonably non-relativistic: $\langle v^2/c^2 \rangle = .20$ for the ψ. Most of the predictions of the model are in reasonably good agreement with experimental observations. The major exceptions are the radiative transition rates, which are a factor of 2-3 too large. However, recent attempts to incorporate relativistic effects give good agreement with experiment.[18]

Once the potential is determined, the model predicts the masses of charmonium states above $D\bar{D}$ threshold. In particular, it predicts that the 1^3D_1 state will be only slightly heavier than the ψ'. To first order, the amplitude for producing a charmonium state in e^+e^- annihilations is proportional to the state's wave function at the origin. Since a 1^3D_1 wave function is zero at the origin, this state would not ordinarily be produced by e^+e^- annihilations. However, the proximity of the 1^3D_1 to the ψ' (which is mostly 2^3S_1) allows the possibility that the 1^3D_1 and 2^3S_1 states will mix, giving

$$|\psi'\rangle = \cos\theta|2^3S_1\rangle - \sin\theta|1^3D_1\rangle$$

$$|\psi''\rangle = \sin\theta|2^3S_1\rangle + \cos\theta|1^3D_1\rangle$$

where θ is a mixing angle. The charmonium model predicts a substantial mixing due to virtual intermediate states, such as $D\bar{D}$, $D\bar{D}^*$, etc., that

couple to both the 1^3D_1 and 2^3S_1 states.[17] Also, the presence of a tensor force in the strong interaction is expected to make a small contribution to the mixing. This mixing allows the ψ'' to be produced in e^+e^- annihilations through its 2^3S_1 component. In addition, relativistic effects[19] allow the coupling of the ψ'' to e^+e^- with an amplitude proportional to the second derivative of the 1^3D_1 wave function at the origin. These effects led to the prediction that a new resonance would be found just above the ψ', which was confirmed by the discovery of the $\psi''(3770)$[15] in 1977.

This thesis reports the results of an experiment that was done to study the properties of the ψ''. The experiment was performed at the SPEAR e^+e^- colliding beam facility where the Crystal Ball detector was used to measure the products of e^+e^- annihilations. The Crystal Ball is unique in its ability to measure accurately photons of all energies over a large solid angle. This capability makes it orthogonal to conventional detectors that primarily measure charged particles. This difference allows the Crystal Ball to examine the ψ'' from a new perspective, where the emphasis is on measuring the photons from ψ'' decays.

Three different aspects of the ψ'' are studied. First, the ψ'' resonance itself is measured. Because the Crystal Ball has a large solid angle coverage, good calorimetry, and loose trigger requirements, it is an excellent detector for measuring the hadronic cross section from e^+e^- annihilation, $\sigma(e^+e^-\rightarrow\text{hadrons})$. The ψ'' is clearly visible as a resonance in this cross section. A fit of the theoretical shape for the resonance to the cross section gives a measurement of the ψ'' mass, leptonic width, and total width.

The second topic of this thesis is a search for structure in the inclusive photon spectrum. The Crystal Ball has demonstrated a high sensitivity for detecting structure in this spectrum. Radiative transitions from the ψ' to the χ_0, χ_1, χ_2, η_c, and η_c' have previously been observed by the Crystal Ball as bumps in the inclusive photon spectrum from the ψ'.[7] The charmonium model predicts that the ψ'' will decay predominantly into $D\bar{D}$ and have a very small branching ratio for radiative transitions. This prediction is tested by searching for unexpected structure in the inclusive photon spectrum of the ψ''.

The final topic uses the ψ'' as a clean source of slow moving D^0 mesons. The D^0 mesons are produced by the reaction $\psi'' \rightarrow D^0\bar{D}^0$, and have a fixed kinetic energy of only 22 MeV (the ψ'' is below threshold for more complicated decay modes such as $D\bar{D}\pi$ or $D\bar{D}^*$). The decay of a D meson does not conserve the charm quantum number, so it is forbidden by the strong and electromagnetic interactions and must be mediated by the weak interaction. One way to learn about the weak coupling of the charm quark to other quarks is by studying the decay modes of the D. Previous experiments have focused on D meson final states which are composed mostly of charged particles.[19,20,21] By contrast, the only D meson final states which the Crystal Ball can fully reconstruct are those composed of particles that decay into photons. This thesis searches for D^0 decays into two and three body final states composed of π^0 and η mesons.

Chapter II

EXPERIMENTAL APPARATUS

2.1 THE SPEAR FACILITY

The experiment was performed at the SPEAR e^+e^- colliding beam facility of the Stanford Linear Accelerator Center (SLAC). This section describes those aspects of SPEAR which are relevant to the present experiment. In the SPEAR ring (see figure 2), electrons and positrons are guided in a roughly circular orbit by a lattice of dipole bending magnets and quadrupole focusing magnets. Electrons from the SLAC linac are injected into the ring at the nominal beam energy to form a single "bunch" of electrons that circles the ring every 780 ns. Similarly, positrons are injected into the ring to form a single bunch that circulates in the opposite direction. The electron and positron bunches collide at the two "interaction regions," where elaborate detectors are set up to measure the products of e^+e^- collisions. The beams collide at a 0° crossing angle, so the center of mass for the e^+e^- collisions is at rest in the laboratory.

As the electrons and positrons orbit the ring, they lose energy because of synchrotron radiation. To compensate for this loss, energy is pumped back into the beams by 4 rf cavities. This causes the beams to be "cigar shaped": very thin transverse to the beam direction ($\sigma_\perp < 1$ mm), but elongated in the beam direction ($\sigma_\parallel \approx 3.2$ cm). The size of the luminous region is a factor of $\sqrt{2}$ smaller than the beam size. Fluctua-

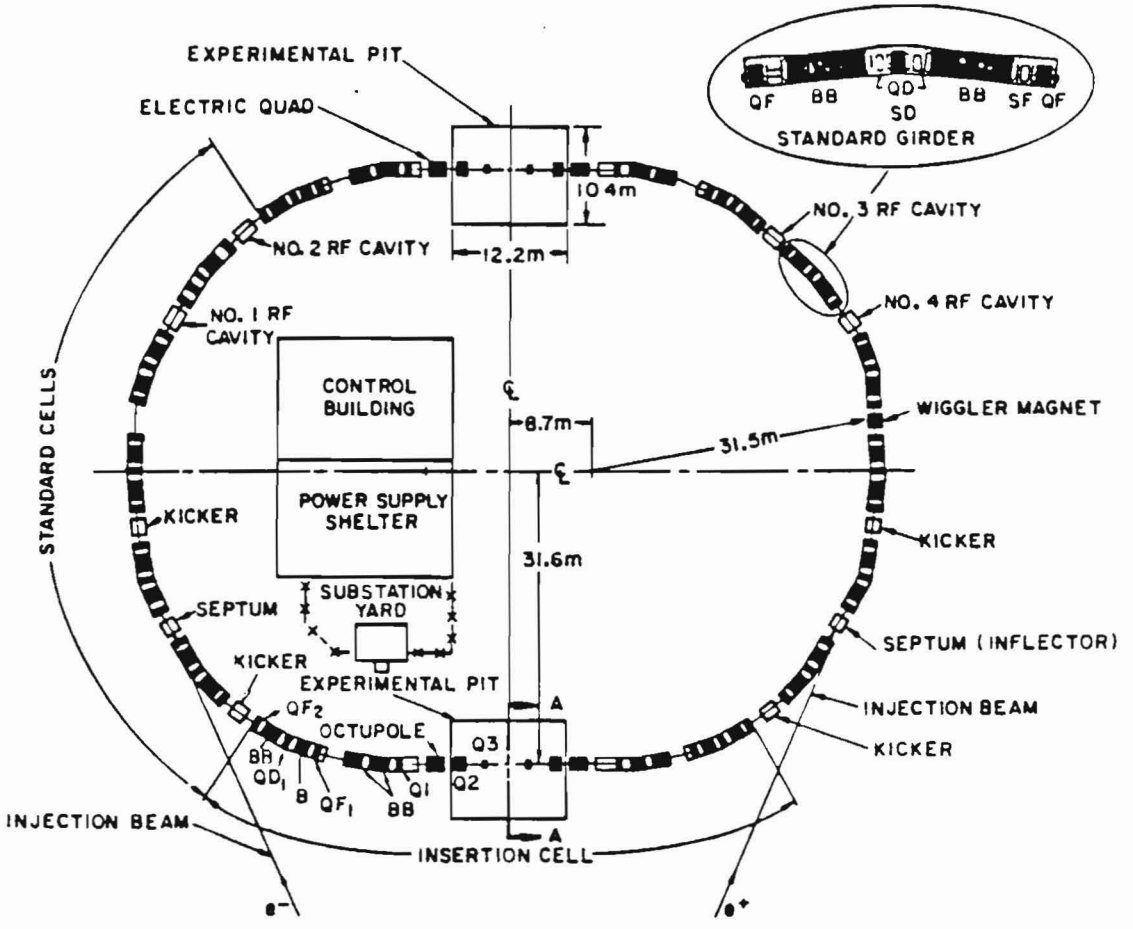

Figure 2: Layout of SPEAR.

tions in the synchrotron radiation cause an energy spread in the beams, which is calculated to be ±1 MeV at the ψ''.[22] There is also a .1% uncertainty in the absolute energy calibration of SPEAR.[23]

The data sample for this experiment was collected during five weeks of running in the winter of 1979. Four weeks were spent at a center of mass energy of 3771 MeV, which is near the peak of the ψ'' resonance, yielding an integrated luminosity of 1765 nb^{-1}. An additional week was spent gathering 383 nb^{-1} in a detailed scan across the resonance. Under typical operating conditions, the beams had lifetimes of 4-6 hours, and SPEAR was refilled with electrons and positrons every 2-3 hours. During most of the running a wiggler magnet was turned on to provide a synchrotron radiation beam for the Stanford Synchrotron Radiation Laboratory. This provided an improvement in the average luminosity with a small increase in the beam energy spread. The average luminosity over the run was 8×10^{29} $cm^{-2}sec^{-1}$, with a peak luminosity of 2.5×10^{30} $cm^{-2}sec^{-1}$.

2.2 THE CRYSTAL BALL DETECTOR

The remainder of this chapter is devoted to a description of the Crystal Ball detector. The Crystal Ball was designed to be the "state of the art" for measuring photons in the energy range 10-4000 MeV. This was achieved by using a highly segmented array of NaI(Tl) crystals to provide accurate measurements of the energy and direction of photons. Using the algorithms described in chapter 3, an energy resolution of

$$\sigma_E/E = .026/E(GeV)^{1/4}$$

was achieved for cleanly identified photons. The high segmentation allows measurement of the photon direction to within ≈2.5°, and provides

separation of nearby photons when they are more than ≈8° apart. To reduce the probability for a photon's escaping detection, 98% of the solid angle was covered by NaI crystals. Additional design goals for the detector included identification of charged particles, measurement of the charged particle trajectories, an accurate determination of the machine luminosity, and the identification of energetic muons.

Figure 3 shows a schematic diagram of the Crystal Ball detector. The diagram shows the major components of the detector:

(1) The Crystal Ball Proper - A highly segmented array of NaI crystals that accurately measures the energy and direction of photons over 93% of 4π sr.

(2) The Central Tracking Chambers - Spark chambers and proportional wire chambers that identify charged particles and measure their trajectories.

(3) The Endcap Detector - Additional NaI crystals and spark chambers that increase the solid angle coverage to 98% of 4π sr.

(4) The Luminosity Monitor - A low angle Bhabha event counter that is used to measure the integrated luminosity.

These components are discussed in more detail in the following sections. Not shown in figure 3 is an external muon identifier made of slabs of iron sandwiched between proportional wire chambers. The muon identifier was not used in this experiment and is not discussed further.

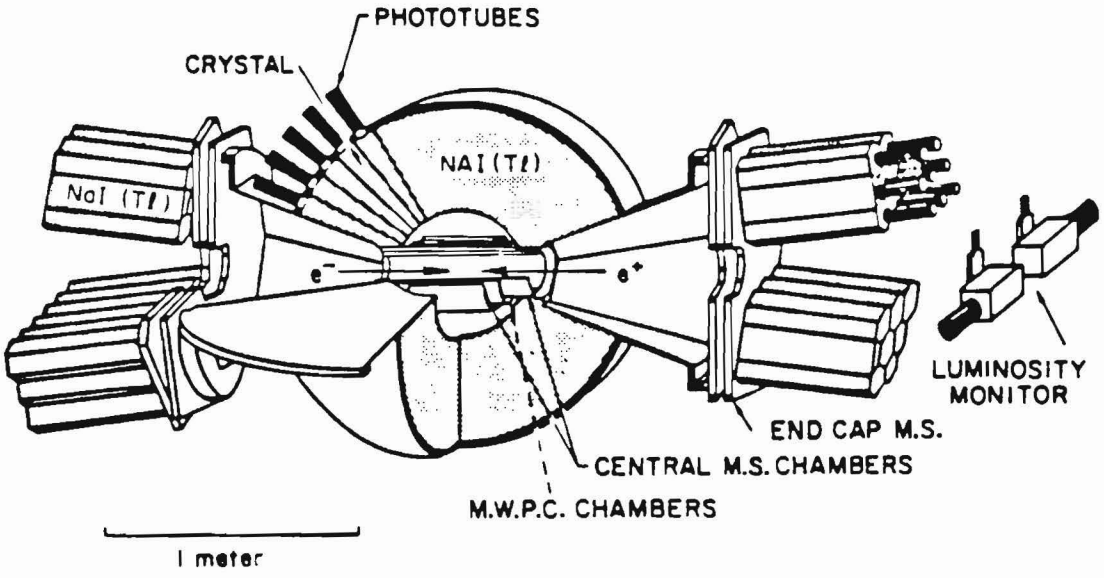

Figure 3: Schematic diagram of the Crystal Ball detector.

2.2.1 The Crystal Ball proper

The Crystal Ball proper is the main component of the Crystal Ball detector. This is no common glass sphere in the hands of an amateur fortuneteller, used to conjure visions of minor matters such as life, death, and the mass of the Higgs. Rather, this Crystal Ball is a spherical array of 672 NaI(Tl) crystals. Its purpose is to accurately measure the energy and direction of photons resulting from e^+e^- annihilations that occur at the center of the detector.

When a photon enters a NaI crystal, an electromagnetic cascade shower is created by the processes of pair production, bremsstrahlung, and Compton scattering. As the shower proceeds, energy is transferred to the NaI crystal by ionization loss and the photoelectric effect. Eventually, the secondary particles drop below the critical energy, at which point the electrons and positrons quickly lose their remaining energy to ionization, while the photons can either interact further or escape the detector. The critical energy for NaI(Tl) is ≈13 MeV. Since NaI is an efficient scintillator, roughly 10% of the original photon energy is converted into low energy photons with wavelengths in the range 320-530 nm.[29] The amount of scintillation light produced by the NaI is directly proportional to the energy of the incident photon, and can be measured by a photomultiplier tube.

The geometry of the Crystal Ball is based upon the geometry of the icosahedron, a 20-sided regular solid. Each face of the icosahedron is an identical equilateral triangle, which will be referred to as a "major triangle" (see figure 4a). In order to achieve the fine granularity desired for this experiment, each of the 20 major triangles is divided

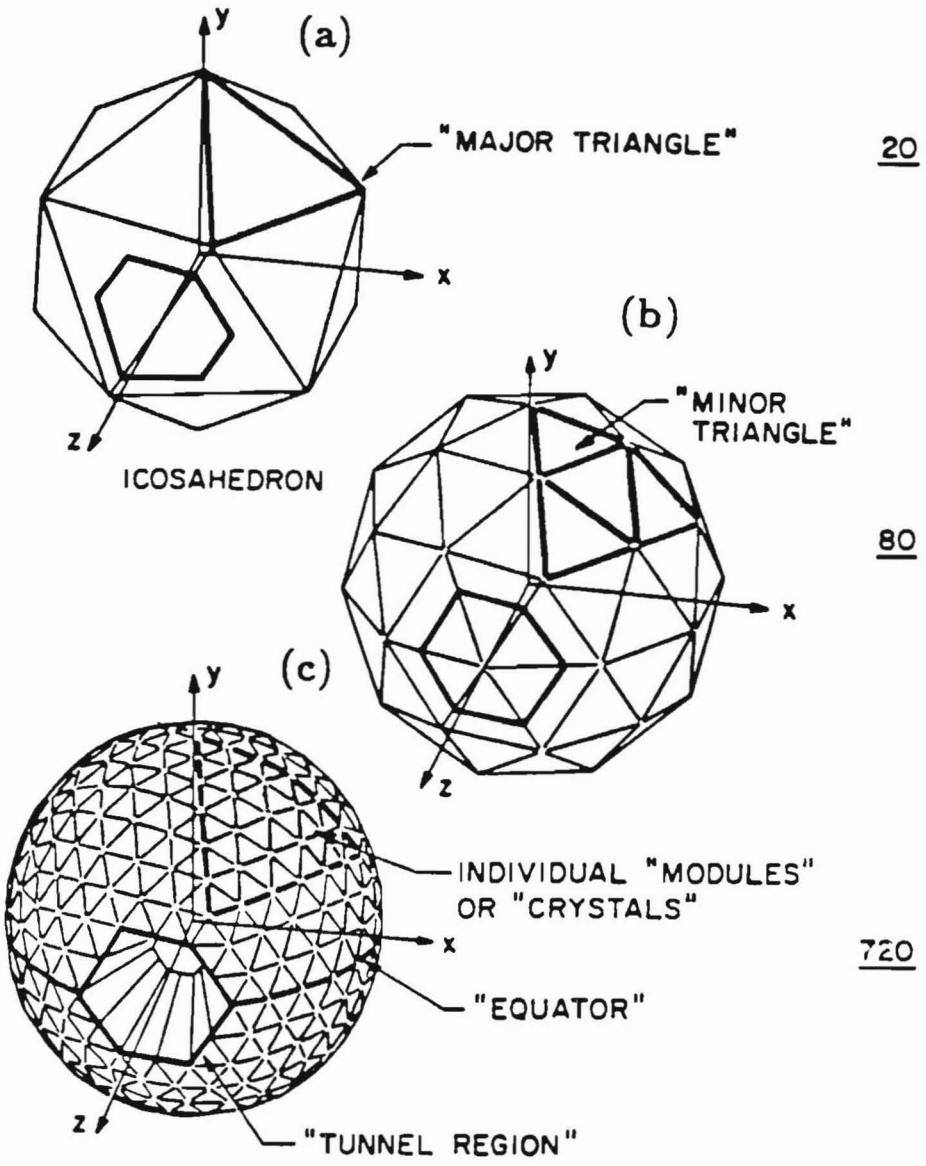

Figure 4: Geometry of the Crystal Ball.

(a) Division into 20 major triangles; (b) division into 80 minor triangles; (c) division into 720 modules.

into 36 smaller triangles. First, each major triangle is divided into 4 "minor" triangles (see figure 4b). This is done by bisecting each side of the major triangle and projecting the new vertices to a uniform distance from the center of the icosahedron. Then, each minor triangle is divided into 9 individual modules by trisecting each side of the minor triangle and again projecting the new vertices (see figure 4c). The result is a nearly spherical object which resembles two "geodesic domes" joined together. This design has the following features: it can be cleanly split into two hemispheres at the "equator," it uses only 11 different module shapes, and each module covers nearly the same solid angle: $\Delta\Omega=0.018\pm.002$ sr.

The above geometry is projected to a radius of 26", with each triangular module forming the outer face of an NaI(Tl) crystal. The inner face of each crystal is determined by shrinking the geometry down to a radius of 10". Figure 5 shows a schematic diagram of a typical crystal. The crystals are 16" long, which corresponds to roughly 16 radiation lengths for showering particles (γ,e), 1 interaction length for strongly interacting hadrons (π,K,p,n), and 210 MeV of energy loss for charged particles at minimum ionization. This length is sufficient to contain nearly all secondaries produced by electromagnetic showers for photon and electron energies attainable at SPEAR. Each crystal was individually "compensated" to give uniform response to energy deposited at any point along the length of the crystal, and optically isolated to prevent "crosstalk" between crystals.

The crystals were stacked into two hemispheres, each with 336 crystals (48 crystals were removed from the above geometry to make room for

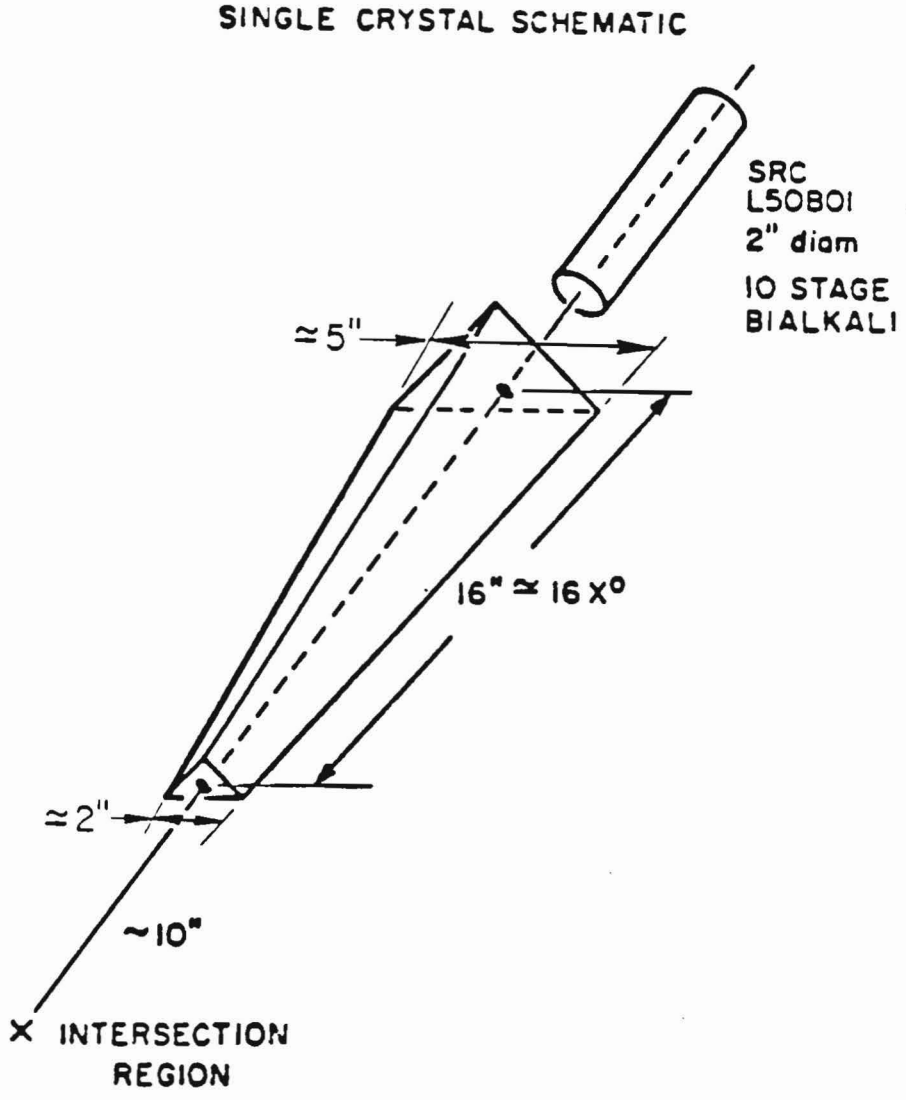

Figure 5: A single crystal and its photomultiplier tube.

the beam pipe). To protect the crystals from hydration, the hemispheres were enclosed in hermetically sealed containers. Each crystal has its own photomultiplier tube to measure the amount of scintillation light produced by the crystal. A scintillation photon must escape through a 2" diameter polished area centered on the outer face of the crystal and then travel through an air gap, a glass window in the container, and finally another air gap before reaching the photomultiplier tube.

2.2.2 Central tracking chambers

The central tracking chambers are designed to fit within the 10" inner radius of the Crystal Ball proper. Their purpose is to identify which energy deposits in the NaI are due to charged particles and accurately measure their trajectories. No measurement is made of the charged particle's momentum or mass. As shown in figure 6, the central tracking system consists of three concentric cylindrical chambers mounted on the beam pipe. The inner and outer chambers are wire spark chambers; a multi-wire proportional chamber is in the middle. The spark chambers produce an accurate measurement of the charged particle's trajectory. Although the proportional chambers are less accurate, they are very efficient and provide fast information to the trigger electronics.

The inner and outer spark chambers have a similar design, differing only in their dimensions and orientation of the wires. These "wires" were formed by etching insulating lines into a copper coated sheet of Mylar. Two sheets of wires were formed into concentric cylinders with wires facing each other and a 9 mm gap between the wires. One sheet contains "straight wires" oriented parallel to the beam direction, while

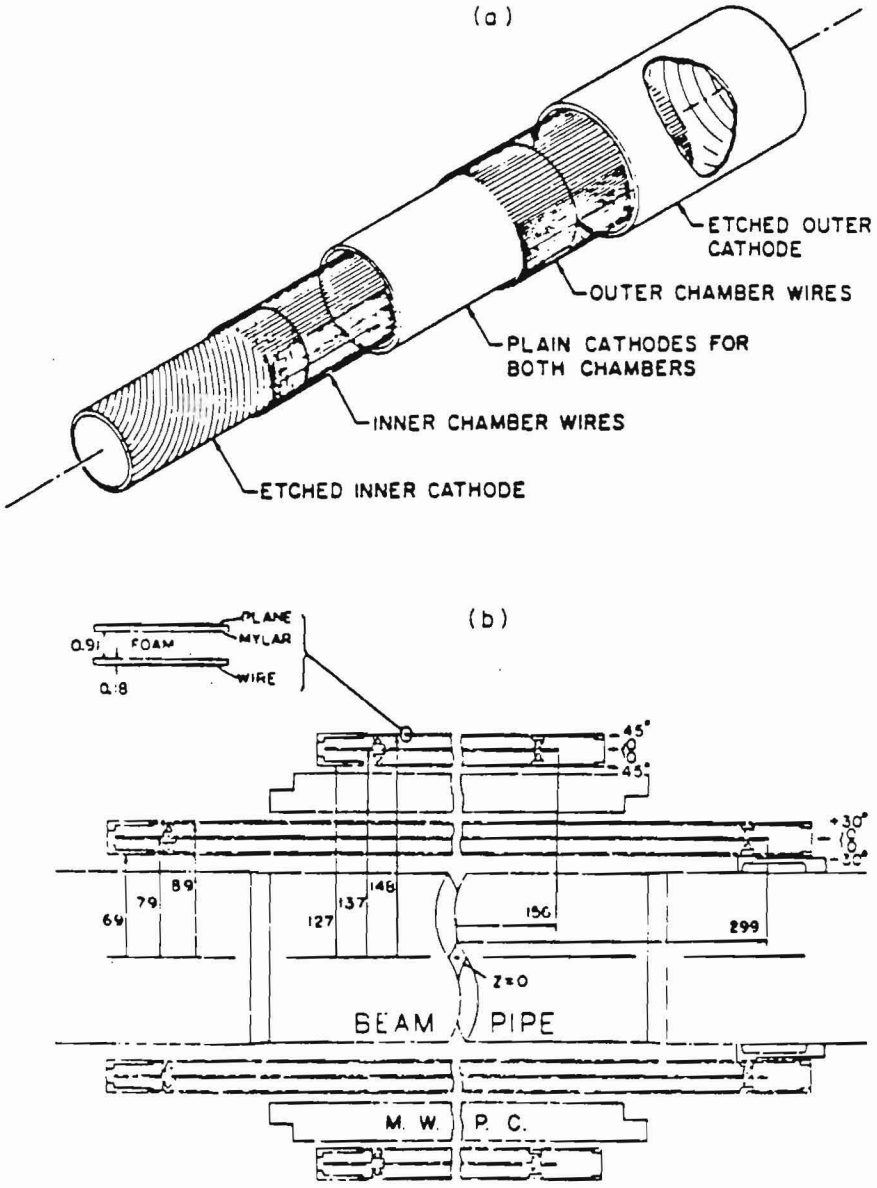

Figure 6: The central tracking chambers.

(a) Exploded view of the multi-wire proportional chamber; (b) detail of the spark chambers (dimensions in mm).

the other sheet is made of "cross wires" that wind in a helix around the beam direction. A charged particle passing through the chamber will register a "hit" on the pair of opposing straight and cross wires closest to the charged particle's trajectory. The location of the straight wire hit determines the ϕ angle of the hit, while the cross wire location can be matched with the ϕ angle to determine the z coordinate of the hit. The inner spark chamber has two such gaps and covers 94% of 4π sr. The outer spark chamber also has two gaps, but covers only 70% of 4π sr because of limited space inside the detector. A gas mixture of 90% Ne/10% He was used in the gap between wires.

A charged particle passing through the spark chambers will leave a hit in each gap (assume for a moment that the chambers are 100% efficient). What happens is that the charged particle leaves a path of ionization along its trajectory through the spark chamber gap. If the detector is triggered, the straight wires are pulsed with 9 kV. The intense electrical field will breakdown in the vicinity of the ionization, causing a small spark to bridge the gap at the point the charged particle passed through the chamber. A wire on each side of the gap will carry the current from the spark, and the magnetostrictive readouts sense this current; the location of the wire is determined from the timing of the magnetostrictive pulse.

Sandwiched between the inner and outer spark chambers is a double-gap multi-wire proportional chamber. Each gap is made from two concentric cylinders of aluminum-coated Mylar separated by 1 cm. One cylindrical wall of each gap was etched into 36 electrically isolated strips. The strips wind in a helix around the beam axis for the inner gap; they

encircle the beam for the outer gap. Gold-plated tungsten wires with a diameter of 0.02 mm were strung through the middle of each gap parallel to the beam direction. The wires were used to determine the ϕ angle of a hit while the strips were used to determine the z coordinate of the hit. Since the strips for the outer gap are at fixed z coordinates, only the inner strips needed to be matched with the ϕ angle to determine the z coordinate. The proportional chamber was operated with the strips at -1.7 kV with respect to the wires and a 90% Ar/10% CO_2 gas mixture was used in the gap.

When a charged particle passes through the proportional chamber, it leaves a trail of ionization in the gas. The ionized electrons drift along the electric field lines towards the nearest positively charged wire. As an electron enters the intense fields close to the wire, it picks up enough energy between collisions with gas atoms to knock additional electrons out of the gas atoms. The result is an "avalanche" that produces thousands of electrons for every electron ionized by the charged particle. The electrons are collected by the wire, causing a small current that is detected by the electronics. The positive ions induce a charge on the nearby strips, which is measured by the electronics. The voltage on the chamber is kept well below the point where the avalanche could develop into a spark, and the chamber quickly recovers.

2.2.3 Endcap detector

The endcap detector is designed to increase the solid angle coverage to 98% of 4π sr. Although the endcaps cover only 5% of the solid angle, they greatly reduce the chance that a particle escapes the detec-

tor. The endcap detector consists of four similar segments. Each segment has 15 hexagonal NaI(Tl) crystals and two sets of double gap magnetostrictive readout spark chambers. Two segments are placed at each tunnel opening of the Crystal Ball proper, one above the beam pipe and one below. Refer to figure 3 for a schematic drawing of the endcap detector.

2.2.4 Luminosity monitor

The luminosity monitor measures the luminosity of the SPEAR machine integrated over the time the detector was ready to take data. An accurate determination of the integrated luminosity is required for calculating cross sections in later chapters. The luminosity monitor operates by counting the number of Bhabha events using small counters located at an angle of 4.25° from the beam direction. The integrated luminosity can be calculated from the number of such events by using the QED cross section for Bhabha scattering, integrated over the acceptance of the counter.

The luminosity monitor is made of four separate arms, as shown in figure 7. Each arm consists of three scintillation counters and a shower counter. The scintillation counters define the acceptance of the arm and the shower counter measures the energy of the electron. For each arm, a Bhabha event was counted if the shower counter and the "P" scintillation counter were in coincidence with the opposing shower counter and the "C" scintillation counter. The "C" counter is somewhat larger than the "P" counter to take into account the spread in the beam position. The counting rate of any single arm is dependent on the beam

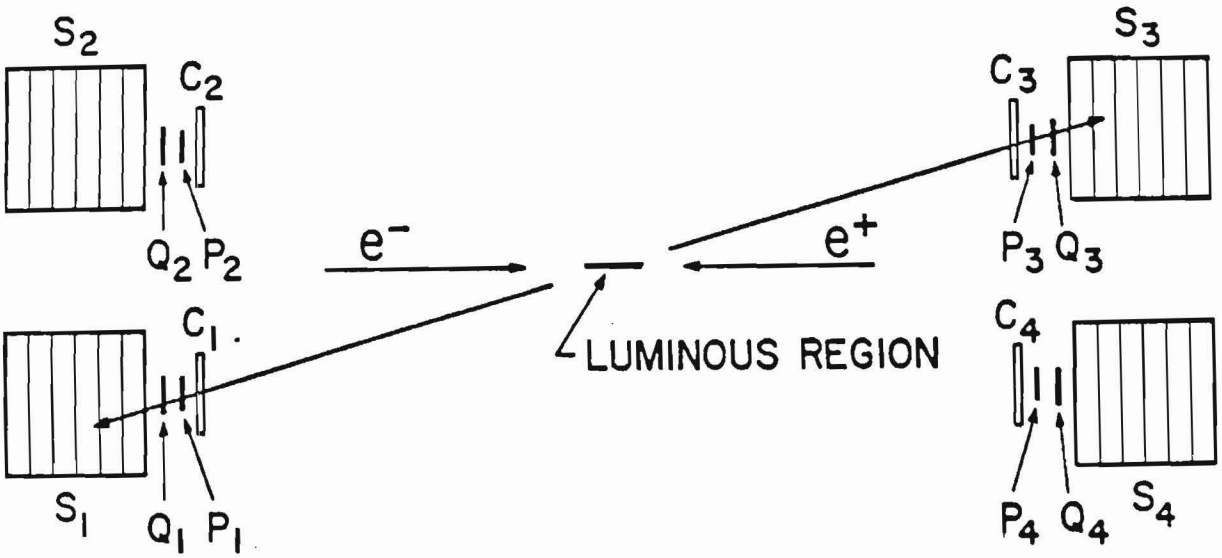

Figure 7: Schematic diagram of the luminosity monitor.

angle and position; however, the sum of all four arms is almost completely independent of the beam angle and position. By comparing the luminosity monitor to a measurement of the luminosity using wide-angle Bhabha events detected by the Crystal Ball proper, the accuracy of the luminosity monitor has been determined to be better than ±3%.

2.2.5 Trigger conditions

At each beam crossing, it is necessary to decide if the detector should be triggered. A trigger causes the spark chambers to be pulsed, the electronics to be read out, and the data written on tape. This decision is based on hardware sums of the energy deposited in the Crystal Ball and the presence of charged particles passing through the proportional chamber.

The following four trigger conditions were established:

(1) At least 1100 MeV of energy deposit in the Crystal Ball proper.

(2) At least 144 MeV in each hemisphere of the ball, including crystals in the tunnel region, and a total energy greater than 775 MeV.

(3) At least two major triangles with energy deposits greater than 140 MeV and at least one charged particle detected by the proportional chamber.

(4) At least 70 MeV of energy deposited in each of two opposing minor triangles.

A trigger was generated if at least one of the trigger conditions was satisfied. Except for the second trigger condition, the crystals in the tunnel region were excluded from the energy sums. (The tunnel region is

the first layer of crystals surrounding the openings for the beam pipe. See figure 4.) The above trigger is very efficient for hadronic events produced at the ψ'' resonance; it is much less stringent than the software cuts made in the hadron selection stage of the data analysis (see section 3.3). The trigger rate was usually in the range 2-3 Hz, which produced a 10% deadtime.

2.2.6 Electronics and data acquisition

Several racks of electronics were used to convert the raw signals from the detector into digitized data that could be understood by the online computer. Whenever a trigger occurred, the electronics:

(1) Integrated and digitized the signal from each photomultiplier tube.
(2) Digitized the timing of sparks detected by the magnetostrictive readouts.
(3) Recorded the locations of wire hits in the proportional chamber.
(4) Digitized the strip signals from the proportional chamber.
(5) Digitized miscellaneous signals such as trigger timings.

Under the control of the online computer, the above information was stored on magnetic tape for later analysis.

Chapter III

DATA ANALYSIS

The ultimate achievement in data analysis would be to select only ψ'' events and determine the four-vector for every particle in the final state. Unfortunately, the limitations of the Crystal Ball detector necessitate a more modest goal. Although it is usually possible to eliminate background events (e.g., cosmic rays, beam-gas interactions, and QED processes), there is no obvious way to distinguish ψ'' events from non-resonant events of the type $e^+e^-\rightarrow$hadrons. Another problem is that the Crystal Ball detector can measure complete four-vectors only for showering particles (γ,e); the energy and mass are unmeasured for long-lived charged particles (μ,π,K,p). Long-lived neutral particles (ν,K_L,n) are either unmeasured or misidentified as photons. To make matters worse, particles can escape the detector because of the incomplete solid angle coverage or be misidentified when the reconstruction algorithms attempt to unscramble a complex event. Nevertheless, it is the task of the analysis program to do the best possible job of selecting and reconstructing the hadronic events.

The data analysis can be divided into four stages:

(1) Calibration - Each NaI crystal is calibrated to accurately convert the pulse height from the photomultiplier tube into the energy deposited in the crystal. Each magnetostrictive readout is calibrated to accurately position the spark chamber wires with respect to the coordinate system of the Crystal Ball proper.

(2) Offline Analysis - Each event is processed by the Crystal Ball "offline analysis" program. This program attempts to reconstruct the four-vector of every particle in the final state.

(3) Hadron Selection - Only events which are consistent with coming from the reaction $e^+e^- \rightarrow$ hadrons are selected. Background events that originate from cosmic rays, beam-gas interactions, or QED processes are removed from the data sample.

(4) PIFIT Analysis - Each event is checked to see if there are any π^0 decays which were misidentified due to overlapping energy deposits of the π^0 decay photons. This stage substantially increases the efficiency for reconstructing π^0 decays when the π^0 energy exceeds 700 MeV.

Each stage of the data analysis is discussed in more detail below.

3.1 CALIBRATION

Calibrations were done every 1-2 weeks to correct for long-term changes in the detector or the associated electronics. The primary goal of a calibration was to update the constants used to calculate the energy depositions in the NaI crystals. The performance of the detector depends crucially on these constants, and even small miscalibrations of ≈2% would seriously degrade the performance of the detector. Each calibration also updated the calibration constants for the magnetostrictive readouts of the central spark chambers.

The energy deposited in an NaI crystal is very nearly proportional

to the photomultiplier tube pulse height.[25] If we assume proportionality, we can relate the energy to the pulse height as follows:

$$H = p + sE$$

where H is the pulse height, E is the energy deposit, p is the pedestal, and s is the slope (the electronics was designed such that the pedestal and slope are both positive). The pedestal and slope will be different for each channel of the electronics and must be determined by the calibration procedure. The NaI electronics incorporates two separate channels for each photomultiplier tube: a low channel for measuring energies in the range 0-160 MeV and a high channel for energies in the range 160-3200 MeV. Thus, we need to determine two pedestals and two slopes for each NaI crystal.

The low channel pedestals, high channel pedestals, and the ratios between the low channel slope and the high channel slope were determined by studying the NaI pulse heights in a portion of the data sample. The pedestals are simply the pulse heights recorded when no energy is deposited in the crystal (a typical event will deposit energy in only 10-20% of the crystals). The ratio between the low channel slope and high channel slope was determined from events which deposited less than 160 MeV in the crystal. For these events the low channel range and the high channel range overlap; the ratio of slopes was determined by requiring that both channels measure the same energy.

To complete the NaI calibration, it is necessary to measure either the low channel slopes or the high channel slopes. A preliminary estimate of the low channel slopes was made by using the 661 keV photon line of a ^{137}Cs source. For each crystal, the low channel pulse height spec-

trum was fit to determine the pulse height that corresponds to 661 keV. The low channel slope was then determined by subtracting the pedestal and dividing by the energy of the photon line. A more accurate determination of the low channel slope was then made using the 6.13 MeV photon line from the following reaction:

$$p + {}^{19}F \rightarrow {}^{20}Ne^* \rightarrow {}^{16}O^* + \alpha$$
$$\hookrightarrow {}^{16}O + \gamma.$$

A small Van de Graaff accelerator supplied the 340 keV protons needed to excite the $^{20}Ne^*$ resonance.[26] Although a 6.13 MeV photon will deposit most of its energy in the crystal it enters, a small amount of energy will usually "leak" into the neighboring crystals. We can measure the amount of leakage energy, and thus correct for it, by using the low channel slopes obtained from the ^{137}Cs calibration. The low channel slope for each crystal was recomputed by requiring that the $^{16}O^*$ line, after correcting for leakage, was centered at 6.13 MeV.

The low channel slopes obtained from the Van de Graaff calibration are much more accurate than those from the ^{137}Cs calibration, but we can do better still by using Bhabha events. It takes ≈1 week of data taking to collect enough Bhabha events to calibrate the detector. The procedure is similar to that used in the Van de Graaff calibration except that we are measuring the high channel slope instead of the low channel slope (this is equivalent since the ratio between slopes was accurately measured). Again, leakage is a significant factor and the Van de Graaff calibration was used to correct for it. The resulting slopes are quite accurate, giving a resolution of $\sigma_E/E=1.9\%$ for 1.886 GeV Bhabha electrons.

The magnetostrictive readouts of the spark chambers must also be calibrated periodically. These calibrations determine constants which are used in converting the readout timings into the locations of the wires that were hit. Bhabha events were selected and the calibration constants were adjusted until the locations of the wires hit were both internally consistent and also consistent with the direction of the Bhabha electron as determined by the Crystal Ball proper. The constants for the central spark chambers were updated after every NaI calibration to maintain the accuracy of the charged particle tracking.

3.2 OFFLINE ANALYSIS

The offline analysis program attempts to reconstruct the final state for each event. The analysis program is divided into five major subroutines:

(1) ENERGY - Calculates the energy deposited in each NaI crystal.

(2) CONREG - Finds "connected regions" of energy deposit. A connected region is a set of contiguous crystals that have energy deposited in them.

(3) BUMPS - Finds "bumps" within each connected region. A bump is a crystal with a sufficiently large energy deposit to indicate that a photon or charged particle entered the crystal.

(4) CHGTKS - Reconstructs the trajectories of charged tracks and determines which bumps were caused by charged particles. Any bump which is not caused by a charged particle is assumed to be caused by a photon.

(5) ESORT - Computes the energy associated with each bump and estimates the direction cosines for the photons in the final state.

The algorithms used in these subroutines are described below.

The ENERGY subroutine uses the photomultiplier tube pulse heights and the calibration constants to make a straight-forward calculation of the energy deposited in each NaI crystal. The CONREG subroutine groups crystals that have more than 10 MeV of energy into "connected regions": sets of crystals that are contiguous with one another. The easiest way to define a connected region is to describe the algorithm used by CONREG. If CONREG finds a crystal with more than 10 MeV that is not already a member of a connected region, a new connected region is formed. The 12 nearest neighbors of this crystal are checked and any neighbors which have more than 10 Mev are included in the connected region.[27] The search proceeds until the neighbors of every crystal in the connected region have been checked and are either in the connected region or have less than 10 MeV of energy.

The BUMPS subroutine uses a pattern recognition algorithm to find one or more "bumps" in each connected region. A bump is a crystal with a sufficiently large energy deposit to indicate that a photon or charged particle probably entered the crystal. The crystal with the highest energy in the connected region is a bump by definition. The remaining crystals in the connected region are candidates for becoming additional bumps. Every candidate is then checked to see if it has an energy deposit which can be attributed to the bump just found. This is done by comparing the candidate crystal's energy against the threshold set by the "bump discriminator." Those candidates with an energy below the

threshold are eliminated from further consideration. If one or more candidates exceeds the threshold, the candidate with the highest energy is added to the list of bumps and the above process is repeated until no more candidates remain. The bump discriminator is a function which depends on the energy of the most recently found bump as well as the distance between this bump and the candidate crystal. The discriminator is somewhat biased against finding additional bumps unless there is clearly an excess of energy well separated from the already existing bumps. This bias prevents interacting charged particles from creating numerous spurious bumps.

The CHGTKS subroutine identifies charged particles and measures their trajectories. The CHGTKS routine uses two different algorithms to reconstruct charged tracks: the first algorithm finds the charged tracks which can be reconstructed using only the information obtained from the central tracking chambers and the endcap chambers; the second algorithm "tags" additional charged tracks by matching hits in the central tracking chambers with bumps in the Crystal Ball proper.

The algorithm for measuring a charged particle's trajectory through the central tracking chambers requires that the charged particle pass through both layers of the spark chamber and fires at least one gap in each layer. The tracking routine first matches the straight wire hits that have similar values for the ϕ angle. The ϕ hits are then matched with various combinations of the cross wire hits to search for reasonable trajectories. The best matches are found and straight line trajectories are fit to the hits in the spark chambers. The z coordinate of the interaction point is determined by assuming that the tracks origi-

nate from x=y=0. If more than one charged track is found, the trajectories are refit using a common interaction point. This algorithm gives an accurate measurement of the charged particle direction and the z coordinate of the interaction point:

$$\sigma_\phi = 20 \text{ mrad}$$

$$\sigma_\theta = 30 \sin^2\theta \text{ mrad}$$

$$\sigma_z \simeq 1 \text{ cm.}$$

A similar algorithm is used to determine the trajectories of charged particles which pass through the endcap chambers.

The above algorithm is unable to determine the trajectory of a charged particle which misses the outer spark chamber or fails to leave sufficient hits because of chamber inefficiency. To identify as many charged particles as possible, a less demanding algorithm is used to "tag" charged particles missed by the first algorithm. The tagging algorithm assumes that a particle, either charged or neutral, entered each crystal which is identified as a bump. An estimate of the particle's trajectory is made by joining the interaction point and the center of the bump crystal. If there are several hits near the points where the trajectory intersects the chambers, the bump is tagged as charged. The criteria for how close the hits must be, the number of hits required, and the relative weight given each chamber were determined empirically. These criteria strike a balance between "undertagging" and "overtagging": the small probability (≈7%) that a charged particle will be misidentified as a photon is approximately equal to the probability that a photon will be misidentified as a charged particle.[28] This algor-

ithm gives a relatively poor resolution for the charged particle direction:

$$\sigma_\phi = 60/\sin\theta \text{ mrad}$$

$$\sigma_\theta = 60 \text{ mrad.}$$

The ESORT subroutine assigns an energy to each bump and estimates the direction cosines for each reconstructed photon. For the purpose of assigning an energy, each bump is treated as a showering particle (γ,e). The energy deposits in the bump crystal and its 12 nearest neighbors are summed and corrected for losses in the material between crystals. This gives an energy resolution of

$$\sigma_E/E = .026/E(\text{GeV})^{1/4}$$

for showering particles with energies in the range 100-1000 MeV. If the bump is caused by a non-showering particle ($\mu,\pi^\pm,K,p,n$), the energy assigned to the bump will usually be quite different from the energy of the particle.

To complete the reconstruction of the final state, it is necessary to measure the direction cosines of the reconstructed particles. The direction cosines of the charged particles were measured by the CHGTKS subroutine; the direction cosines of particles associated with neutral bumps can be estimated under the assumption that they are photons. Since photons nearly always deposit the most energy in the crystal they enter, a first estimate of the photon direction is that it entered the bump crystal. A more accurate estimate can be made by dividing the bump crystal into 16 hypothetical submodules, as shown in figure 8, and finding the submodule which the photon most likely entered. The ESORT routine uses an algorithm which compares the energy deposit in each crystal

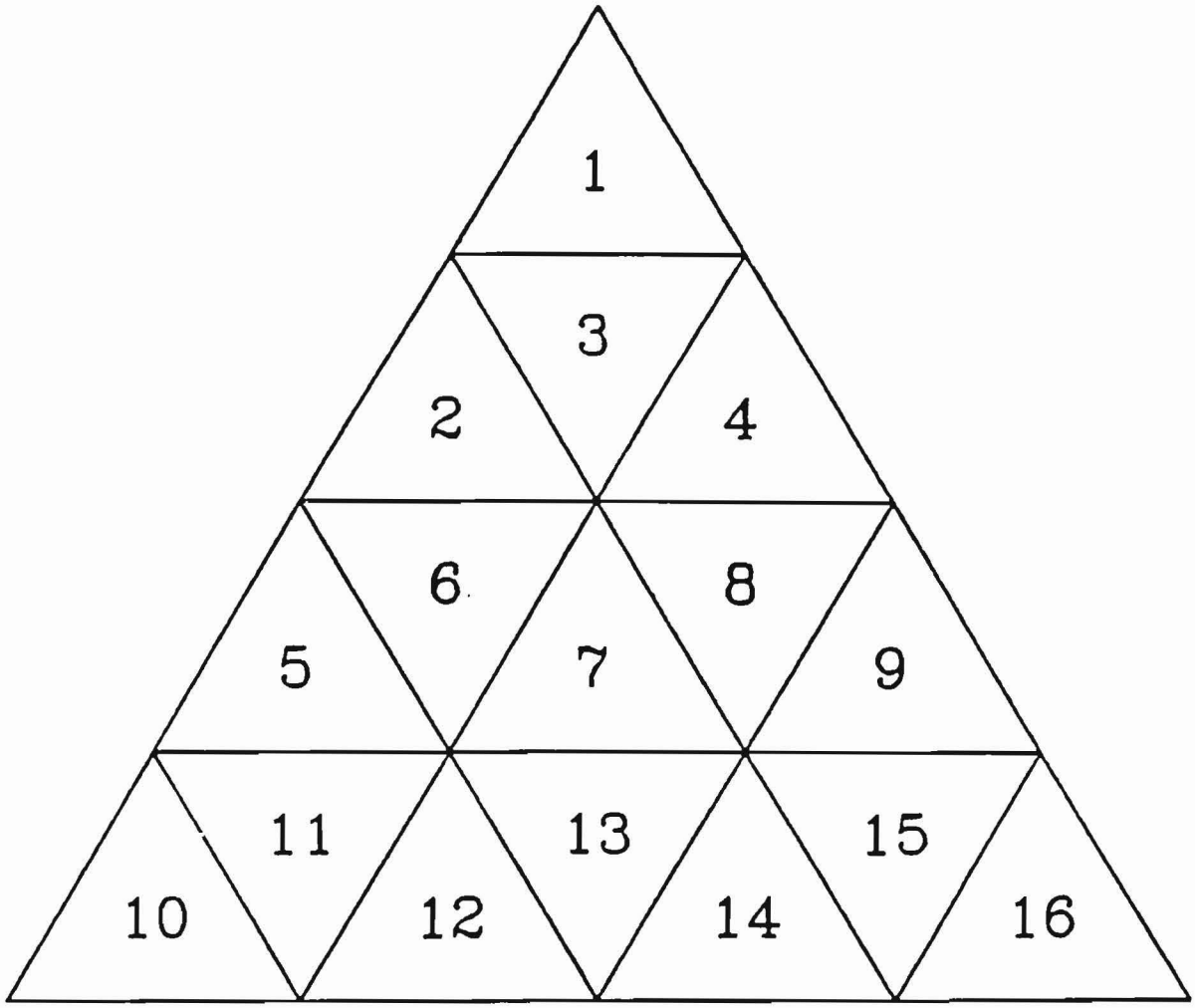

Figure 8: Division of a module into 16 submodules.

with the average energy deposit that would be expected due to a photon in a particular submodule.[29] This algorithm finds the submodule for which the energy deposits are closest to the expected averages; the photon is assigned directions cosines which point at the center of this submodule. The angular resolution for photons obtained from this algorithm is given by:

$$\sigma_\phi = \sigma_0/\sin\theta$$

$$\sigma_\theta = \sigma_0$$

where σ_0 is between 25 and 40 mrad, depending on the photon energy.[30] Although this algorithm is not as accurate as the one described in appendix A, it is used because it requires less computer time.

The results of the offline analysis are summarized by a collection of "tracks" in the "track bank." A track is the collection of attributes that have been measured for a particular particle in the final state. These attributes include the measured energy and direction cosines, as well as an indication of whether the particle was charged or neutral. The track bank forms the basis for most of the analysis that follows.

3.3 HADRON SELECTION

Most of the events recorded on tape were not from the reaction $e^+e^-\rightarrow$hadrons. These background events have many sources: cosmic rays, beam-gas interactions, and QED processes such as $e^+e^-\rightarrow e^+e^-$. Most of the background events can be clearly distinguished from hadronic events by the topology of the event. For example, Bhabha scattering events have two tracks with energies equal to beam energy; no hadronic final state

would have this characteristic. By making a series of cuts on the data, it is possible to remove nearly all of the background events while keeping almost all of the hadronic events. This process is referred to as "hadron selection."

The cuts used to select hadronic events are nearly the same as the cuts developed for measuring the hadronic cross section.[31,32] These cuts, which are described in detail by reference 31, are summarized below:

(1) QED events are removed. This cut removes events which have 2 or more tracks with greater than 55% of the beam energy. Also, events which have fewer than 4 connected regions and one track with greater than 75% of the beam energy are removed.

(2) Beam-gas scattering events are removed. An event is due to beam-gas scattering if it has a low transverse momentum with respect to the beam axis (i.e., $\sum p_t^2$ is small).

(3) Cosmic ray events are removed. Cosmic ray muons which pass through the detector leave energy along the straight-line path of the muon. The cosmic ray events which are not removed by other cuts are the ones that graze the detector, passing through many NaI crystals. If the energy deposits are consistent with a straight-line path and there is a large asymmetry in the energy deposit, the event is removed.

(4) General purpose cuts remove events with fewer than 3 connected regions or a large asymmetry in the energy deposit.

3.4 PIFIT ANALYSIS

The offline analysis program often misidentifies an energetic π^0 as a single photon when the π^0 decay photons are "merged" into a single connected region. The misidentification occurs if the BUMPS algorithm fails to find a second bump associated with the smaller of the two photons. The π^0 decay photons can merge into a single connected region when the π^0 energy exceeds 500 MeV; misidentification becomes a serious problem when the π^0 energy exceeds 700 MeV. Most such misidentifications were corrected by the PIFIT program (see appendix A for a description of the PIFIT program).

A connected region was analyzed by PIFIT if the following criteria were satisfied:

(1) The connected region energy was greater than 500 MeV.
(2) There were no charged tracks in the connected region.
(3) There were no more than two bumps in the connected region.
(4) None of the bumps in the connected region came from an endcap crystal.

Figure 9 is a histogram of the photon-photon mass, $m_{\gamma\gamma}$, obtained from the PIFIT analysis. The histogram shows a large peak at low mass due to single photons, an obvious peak at the π^0 mass, and a smooth background under the π^0 peak due to the random overlap of two photons. A connected region was identified as a π^0 if $m_{\gamma\gamma}$ was in the range 80-180 MeV and at least 95% of the energy in the connected region could be attributed to the π^0 (this cut eliminates connected regions which have additional energy deposits beyond those expected for two photons). The PIFIT anal-

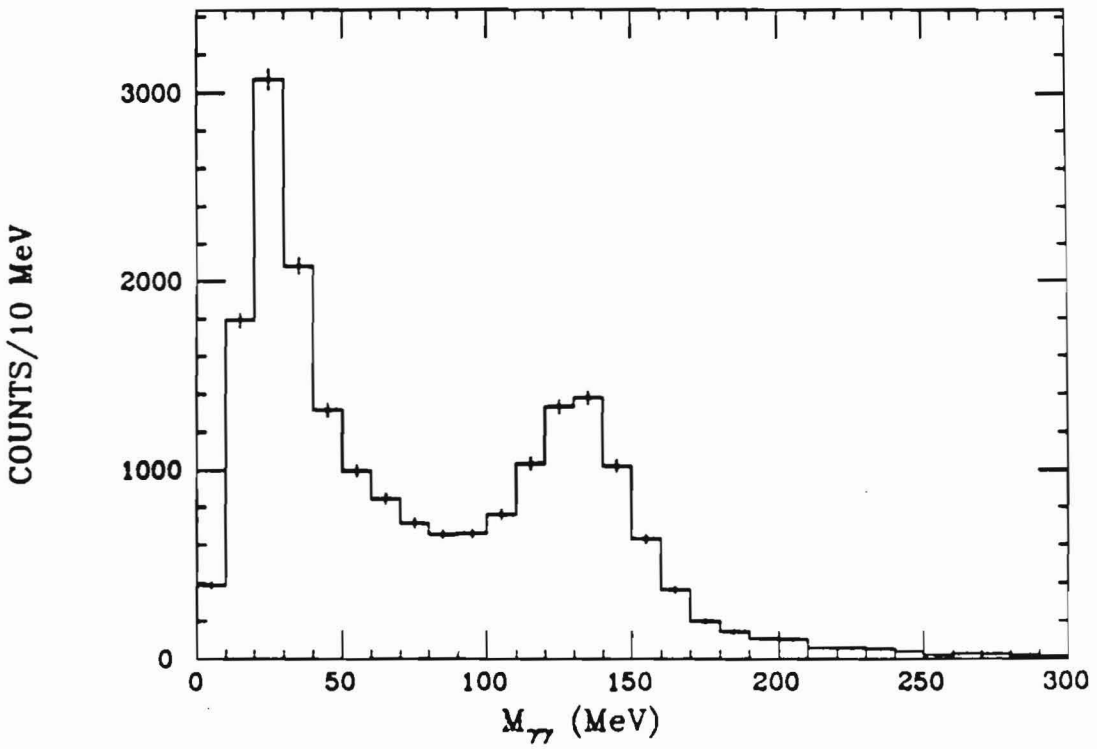

Figure 9: Mass distribution obtained from PIFIT.

ysis greatly increases the efficiency for finding energetic π^0 decays, which is an important part of reconstructing neutral decay modes of the D^0 meson.

Chapter IV

THE ψ'' RESONANCE

The ψ'' resonance is clearly visible as an enhancement in the hadron cross section, $\sigma(e^+e^-\rightarrow hadrons)$, at a center of mass energy of approximately 3770 MeV. Such a resonance is characterized by three resonance parameters[33]: the mass of the resonance, the total width of the resonance, and the partial width for the decay of the resonance to e^+e^-. This chapter describes a measurement of the ψ'' resonance parameters made by fitting a modified Breit-Wigner line shape to the enhancement in the hadron cross section.

An accurate measurement of the ψ'' resonance parameters is important for two reasons: to test the predictions of the charmonium theory and to measure the cross section for D meson production. The ψ'' is usually interpreted as a predominantly 1^3D_1 charmonium state with a small admixture of the 2^3S_1 charmonium state. This interpretation is based upon the predictions of the potential model, so an accurate determination of the ψ'' resonance parameters provides an important test for the model. Of particular interest is the leptonic width, Γ_{ee}, which is sensitive to the amount of mixing between the 1^3D_1 and the 2^3S_1 charmonium states. The D meson cross section near the peak of the ψ'' resonance is needed to calculate branching ratios for exclusive decay channels of the D mesons. Under the assumption that the ψ'' decays predominantly to $D\bar{D}$ and that non-resonant D production is small, the cross section for D meson pro-

duction is simply twice the ψ'' cross section. The basis for these assumptions is discussed below.

4.1 THE HADRON CROSS SECTION

This measurement of the ψ'' resonance parameters is based upon 23 measurements of the hadron cross section made in the vicinity of the ψ'' resonance. Data samples of 200-500 hadronic events were acquired for 22 different center-of-mass energies in the range 3670-3872 MeV. In addition, a large data sample with ≈40K hadronic events was acquired near the peak of the ψ'' resonance. For each data sample, the hadronic events were counted and a measurement of the hadron cross section was made.

Several selection criteria were used to determine which events should be counted as hadronic events. The initial hadron selection cuts were described in section 3.3. These cuts were deliberately kept loose to avoid losing rare decay modes of the D mesons, with the result that a significant fraction (≈15%) of the events passing the initial cuts originate from beam-gas interactions. To remove as many beam-gas events as reasonably possible, two additional cuts were imposed:

(1) At least 20% of the center-of-mass energy must be deposited in the NaI crystals, excluding the endcap crystals and those crystals nearest the beam openings.

(2) At least one charged track must be reconstructed from the hits in the central spark chambers (a bump identified as being charged by the tagging algorithm is insufficient).

These cuts remove most of the cosmic ray and beam-gas events from the data sample: the cosmic ray contamination is less than 1% and the beam-

gas contamination is less (probably much less) than 5%. These additional cuts are not expected to reduce significantly the detection efficiency for $D\bar{D}$ events since these events nearly always contain at least 2 charged particles and deposit more than 20% of the center of mass energy in the NaI crystals.

Another source of background is events from the process $e^+e^-\to\tau^+\tau^-$ that are misidentified as hadronic events. The probability of a $\tau\tau$ event being misidentified as a hadronic event was determined by a Monte Carlo simulation of these events in the Crystal Ball detector. After applying the hadron selection cuts, (42±4)% of the simulated $\tau\tau$ events survived.[39] This probability was found to be constant over the energy range encompassed by the data samples. For each data sample, the expected number of misidentified $\tau\tau$ events was calculated and subtracted from the observed number of hadronic events (the lowest order QED calculation of the $\tau\tau$ cross section was used to compute the number of produced $\tau\tau$ events).

The observed hadron cross section was determined for each data sample by taking the number of hadron events (after τ subtraction) and dividing by the integrated luminosity. These results can be restated in terms of R, the ratio of the hadron cross section to the $e^+e^-\to\mu^+\mu^-$ cross section:

$$R \equiv \frac{\sigma(e^+e^-\to\text{hadrons})}{\sigma(e^+e^-\to\mu^+\mu^-)}$$

where the $\mu\mu$ cross section is given by

$$\sigma(e^+e^-\to\mu^+\mu^-) = 86.8/[E_{cm}(\text{GeV})]^2 \text{ nb}.$$

Table 1 summarizes the results of the hadron cross section measurements.

It should be noted that the observed hadron cross sections are not efficiency corrected (see section 4.4).

TABLE 1

Observed Hadron Cross Section Measurements

E_{cm} (MeV)	σ_{obs} (nb)	R_{obs}
3670	13.2±0.8	2.05±0.12
3692	41.1±2.1	6.45±0.34
3704	24.1±1.4	3.81±0.23
3716	19.7±1.3	3.13±0.20
3728	17.5±1.2	2.79±0.19
3740	16.7±1.0	2.69±0.16
3746	18.5±1.0	2.99±0.16
3752	20.3±1.0	3.29±0.16
3758	19.1±1.0	3.11±0.16
3764	20.1±1.4	3.28±0.23
3770	20.1±1.3	3.29±0.21
3771	20.8±0.4	3.40±0.07
3776	21.9±1.4	3.60±0.23
3782	19.3±1.2	3.18±0.20
3788	16.9±1.1	2.79±0.18
3794	14.5±1.1	2.40±0.18
3800	15.4±1.1	2.55±0.19
3812	14.5±1.1	2.43±0.18
3824	14.2±1.1	2.38±0.19
3836	17.1±1.2	2.90±0.20
3848	12.8±1.0	2.18±0.18
3860	14.7±1.1	2.52±0.19
3872	13.8±1.1	2.38±0.19

The error in the cross section measurements contains a small point-to-point systematic error (0.07 units of R) added in quadrature with the statistical error. The point-to-point error was determined by

dividing the largest data sample (≈40K hadrons at E_{cm}=3771 MeV) into 37 subsamples with ≈1000 hadrons apiece. A point-to-point error of 0.07 units of R was necessary to bring the observed cross sections for the 37 subsamples into agreement. Since these subsamples span a month of running time with differing beam and detector conditions, this method is expected to give a good estimate of the point-to-point error for different data samples.

4.2 A MODEL FOR THE HADRON CROSS SECTION

This section describes a model for the hadron cross section in the vicinity of the ψ'' resonance. The model has several free parameters, including the ψ'' resonance parameters, which were determined by fitting the model to the data (see section 4.5). The "naive" form of the model, which neglects radiative corrections and efficiency corrections, is given by:

$$\sigma_{naive} = \sigma_{NC} + \sigma_{\psi} + \sigma_{\psi'} + \sigma_{\psi''}$$

where σ_{NC} is the contribution from non-charm processes and σ_{ψ}, $\sigma_{\psi'}$, and $\sigma_{\psi''}$ are resonance terms for the ψ, ψ', and ψ'', respectively. The radiative and efficiency corrections to the naive model are discussed in sections 4.3 and 4.4, respectively. Note that the ψ and ψ' terms are included because radiative corrections cause these narrow resonances to have "radiative tails" that contribute to the measured hadron cross section.

The non-charm background is taken to be a constant value of R, independent of the center of mass energy[35]:

$$\sigma_{NC} = R_{NC} \cdot \sigma(e^+e^- \rightarrow \mu^+\mu^-)$$

where R_{NC} is a constant that was allowed to vary in the resonance parameter fit. This form is motivated by the quark-parton model, which predicts that non-charm processes contribute ≈2 units of R.

The ψ is sufficiently narrow that it can be approximated by a δ function:

$$\sigma_\psi = A_\psi \cdot \delta(E_{cm} - M_\psi)$$

where M_ψ is the mass and A_ψ is the integrated hadron cross section of the ψ resonance. For a Breit-Wigner line shape, the integrated hadron cross section is given by:

$$A_\psi = \frac{6\pi^2}{M_\psi^2} \frac{\Gamma_{ee}\,\Gamma_{had}}{\Gamma_{tot}}$$

where Γ_{ee} is the partial width to e^+e^-, Γ_{had} is the partial width to hadrons, and Γ_{tot} is the total width of the ψ. For the resonance parameter fit, the ψ mass was fixed at its "SPEAR value" of 3095 MeV. The standard values[36] of Γ_{ee}, Γ_{had}, and Γ_{tot} were used to determine A_ψ. The ψ' term is the same as the ψ term except that the mass of the ψ' is 3684 MeV and the integrated hadron cross sections is somewhat smaller. Since the radiative tail of the ψ' is a prominent feature of the data, $A_{\psi'}$ was allowed to vary in the resonance parameter fit.

The final term in the model is $\sigma_{\psi''}$, the line shape for the ψ'' resonance. It is clear from the hadron cross section measurements that the ψ'' is a fairly wide state, ≈100 times as wide as the ψ', though only slightly higher in mass. This suggests that the ψ'' decays predominantly to the OZI allowed final state $D\bar{D}$. For the remainder of this thesis, it is assumed that the $D\bar{D}$ decay mode predominates.

Since the ψ'' is only ≈40 MeV above $D\bar{D}$ threshold, it is necessary to include threshold effects in the ψ'' line shape. This is done by using an energy dependent width in the Breit-Wigner line shape[37]:

$$\sigma_{\psi''} = \frac{3\pi}{E_{cm}^2} \frac{\Gamma_{ee}\,\Gamma(E_{cm})}{(E_{cm}-M_{\psi''})^2 + (\Gamma(E_{cm})/2)^2}$$

where $M_{\psi''}$ is the mass, Γ_{ee} is the partial width to e^+e^-, and $\Gamma(E_{cm})$ is the total width of the resonance.

The energy dependent width incorporates phase space and centrifugal barrier effects into the line shape. For the $D\bar{D}$ decay, the phase space is proportional to the momentum of the D. The effect of the p-wave centrifugal barrier is approximated by using the centrifugal barrier factor derived for a square well potential.[37] Aside from phase space and centrifugal barrier effects, the ψ'' should decay equally to $D^0\bar{D}^0$ and D^+D^-. Including these effects, the two decay modes no longer make equal contributions to the ψ'' width:

$$\Gamma(E_{cm}) \propto \frac{p_0^3}{1 + (rp_0)^2} + \frac{p_+^3}{1 + (rp_+)^2}$$

where p_0 (p_+) is the momentum of the D^0 (D^+) and r is the radius of interaction. The proportionality constant is determined by defining Γ_{tot} to be the value of the energy dependent width at the resonance mass. As in previous measurements of the ψ'' resonance parameters,[15] the radius of interaction was taken to be 2.5 fm.[38] The values of $M_{\psi''}$, Γ_{ee}, and Γ_{tot} were allowed to vary in the resonance parameter fit.

4.3 RADIATIVE CORRECTIONS

It is necessary to apply radiative corrections to each term of the model before comparing the model with the data. The most important of these corrections is due to the radiation of a photon by the initial state electron or positron, thereby reducing the effective center of mass energy. This correction is responsible for the radiative tails of the ψ and ψ' in the data. To distinguish the naive cross section from the radiatively corrected cross section, the following notation is used: naive cross sections are denoted by the symbol σ; radiatively corrected cross sections are denoted by $\bar{\sigma}$. The radiative corrections were done according to the following formula[39]:

$$\bar{\sigma}(E_{cm}) = \eta\sigma(E_{cm}) + t\int_0^E \frac{dk}{k}\left[\frac{k^t}{E^t} - \frac{k}{E} + \frac{k^2}{2E^2}\right]\sigma(2\sqrt{E^2-Ek})$$

$$t = \frac{2\alpha}{\pi}(2\ln(2E/m_e) - 1)$$

$$\eta = \frac{2\alpha}{\pi}\left[\frac{\pi^2}{6} - \frac{17}{36}\right] + \frac{13}{12}t$$

where E is the beam energy ($E_{cm}/2$), α is the fine structure constant, and m_e is the electron mass. This formula includes all first-order QED corrections and the effect of multiple soft photon emission.

4.4 EFFICIENCY CORRECTIONS

The hadron selection criteria misidentify a small fraction of the hadron events as background events. The misidentified hadron events are rejected from the data sample, causing the observed hadron cross section to be somewhat less than the true hadron cross section. Since the model

is to be compared with the observed hadron cross section, the naive model must be corrected for the hadron detection efficiency. The corrected model, $\bar{\sigma}_{cor}$, is obtained by applying radiative and efficiency corrections to the naive model:

$$\bar{\sigma}_{cor} = \epsilon_{NC}\bar{\sigma}_{NC} + \epsilon_{\psi}\bar{\sigma}_{\psi} + \epsilon_{\psi'}\bar{\sigma}_{\psi'} + \epsilon_{\psi''}\bar{\sigma}_{\psi''}$$

where ϵ_{NC}, ϵ_{ψ}, $\epsilon_{\psi'}$, and $\epsilon_{\psi''}$ are the hadron detection efficiencies for the non-charm, ψ, ψ', and ψ'' processes, respectively. These efficiencies are not expected to vary significantly over the energy range of the data sample.[50]

It is not necessary to know ϵ_{NC} or $\epsilon_{\psi'}$ since the magnitudes of the non-charm and ψ' terms were allowed to vary in the resonance parameter fit. Furthermore, the contribution from the radiative tail of the ψ is so small (R_{ψ}=0.1) that only a rough estimate of ϵ_{ψ} is necessary. The hadron detection efficiency is estimated to be 0.9±0.1 for these terms.

The value of $\epsilon_{\psi''}$ was determined by a Monte Carlo simulation of $D^0\bar{D}^0$ and D^+D^- events in the Crystal Ball detector. The Monte Carlo produced $D\bar{D}$ initial states with the expected angular distribution for a pair of pseudoscaler mesons:

$$\frac{dN}{d(\cos\theta)} \propto \sin^2\theta$$

where θ is the angle between the D meson and the beam axis. The D mesons were decayed according to a model described in appendix B, and the response of the detector to the decay products was simulated.[51] Finally, the offline analysis and hadron selection procedures were applied to the Monte Carlo events.

The hadron detection efficiency is the fraction of simulated events that survive the hadron selection cuts. The hadron detection efficiency was determined to be 0.89±0.05 for the $D^0\bar{D}^0$ decay mode and 0.85±0.05 for the D^+D^- decay mode. The ψ'' resonance is expected to have approximately equal decay rates to $D^0\bar{D}^0$ and D^+D^-, yielding an average efficiency of $\epsilon_{\psi''}$=0.87±0.05. The error in these efficiencies is almost entirely due to the uncertainty in the branching ratios used in the model for D meson decay (see appendix B).

4.5 THE RESONANCE PARAMETER FIT

The resonance parameters were determined by a least squares fit of the corrected model to the observed hadron cross section. The following parameters were allowed to vary in the fit: the ψ'' resonance parameters, $M_{\psi''}$, Γ_{ee}, and Γ_{tot}; the magnitude of the non-charm term, R_{NC}; and the magnitude of the ψ' radiative tail, $A_{\psi'}$. The results of the fit are shown in figure 10, where the data points are the observed hadron cross section measurements (in units of R) and the solid curve is the corrected model. Figure 11 shows the same data with the non-charm contribution and the radiative tails of the ψ and ψ' subtracted. The corrected model gives a reasonably good fit to the data points (x^2=23 for 18 degrees of freedom).

The ψ'' resonance parameters were determined from the fit:

$M_{\psi''}$ = 3768± 2 MeV

Γ_{ee} = 283±70 eV

Γ_{tot} = 34± 8 MeV

where there is an additional ±4 MeV systematic error in the ψ'' mass due

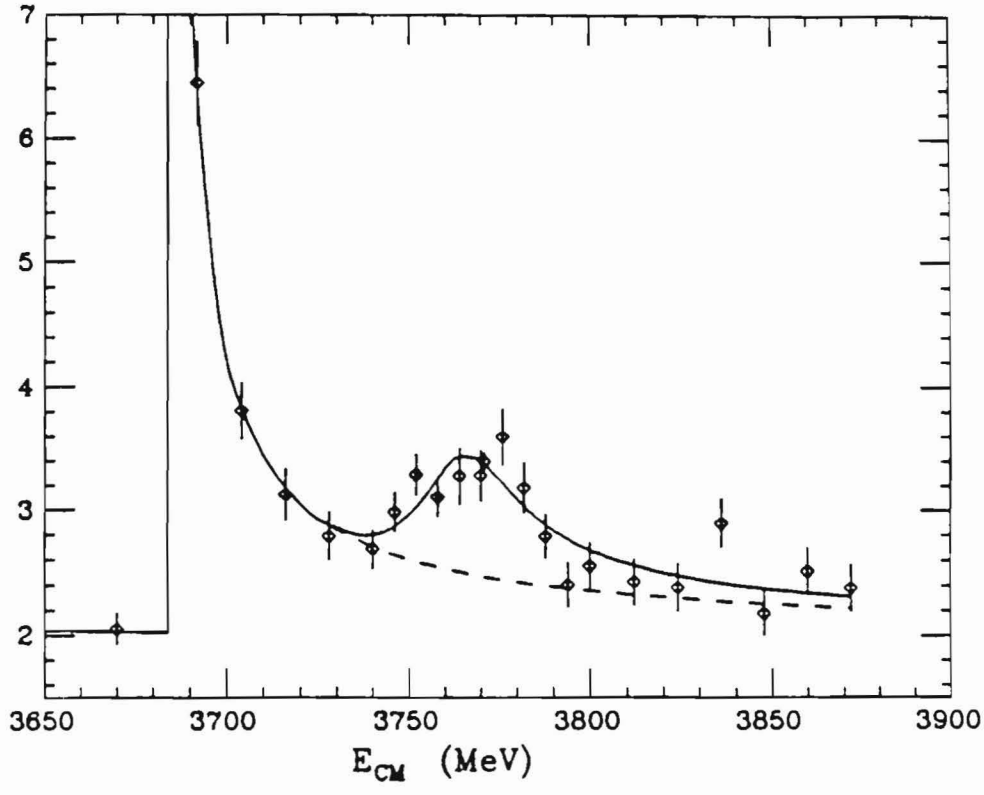

Figure 10: ψ'' resonance fit.

The solid curve shows the results of the resonance parameter fit; the dashed curve shows the nonresonant contribution to R.

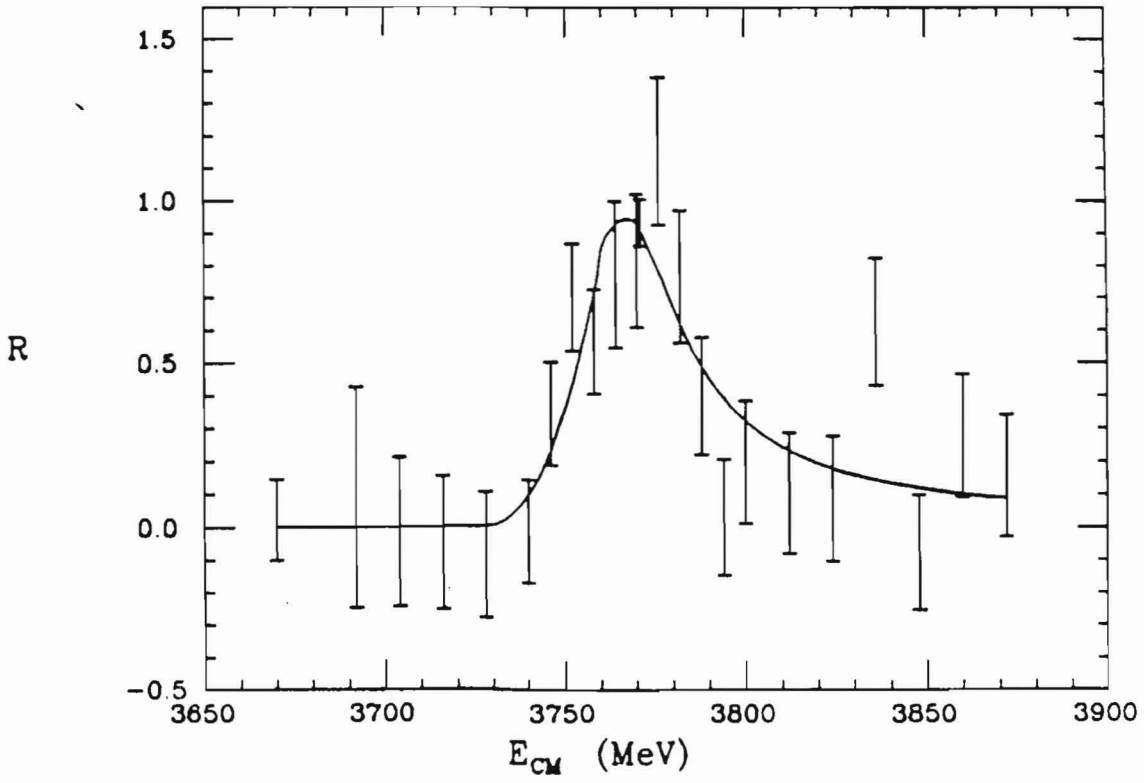

Figure 11: ψ'' resonance fit - background subtracted.

The dashed curve shows the ψ'' line shape, including radiative corrections, that was determined by the fit.

to the uncertainty in the SPEAR energy calibration. The fitted magnitudes of the non-charm and ψ' terms are consistent with previous measurements: $R_{NC}\simeq 2$ and $A_{\psi'}\simeq 5$ nb-GeV.

The resonance parameter fit was used to determine the ψ'' and D meson cross sections. The ψ'' cross section was determined to be 6.7±0.9 nb at the ψ'' mass (E_{cm}=3768 MeV). For the large data sample at E_{cm}=3771 MeV, the ψ'' cross section was determined to be 6.4±0.9 nb. In determining the D meson cross sections, it is assumed that the ψ'' decays almost entirely to $D\bar{D}$ final states, as suggested by the relatively large width of the ψ''. Making the additional assumption that non-resonant D production is small (see cross check (4) below), the total D meson cross section is then twice the ψ'' cross section. Taking into account the unequal phase space and centrifugal barrier factors for the $D^0\bar{D}^0$ and the D^+D^- final states, the D meson cross sections at E_{cm}=3771 MeV were determined to be 6.8±1.2 nb and 6.0±1.1 nb for the D^0 and $D^\pm$ mesons, respectively.

To verify that these results do not depend on the choice of hadron selection criteria or the details of the model, several cross checks were made:

(1) A measurement of the hadron cross section was made using significantly different hadron selection criteria. Fitting the model to this alternative measurement of the hadron cross section yielded ψ'' resonance parameters in good agreement with the above results.

(2) The point-to-point systematic error in the hadron cross section measurements was estimated using the large data sample taken at E_{cm}=3771 MeV. Although not expected, there could be a somewhat

larger point-to-point error between different data samples. A larger point-to-point error does not significantly change the above results.

(3) The centrifugal barrier factor in the ψ'' line shape depends upon the radius of interaction. The above results use a radius of 2.5 fm, but similar results are obtained for any radius greater than 1 fm.

(4) There could be a large contribution to the hadron cross section from the non-resonant production of $D\bar{D}$ final states. Several different forms for a non-resonant $D\bar{D}$ term were included in the model; none of them significantly improved the fit or made a significant change in the ψ'' resonance parameters. This suggests that non-resonant $D\bar{D}$ production is small at these energies.

(5) A potential model calculation of the $D\bar{D}$ cross section predicts a ψ'' line shape that is distorted by momentum dependent decay amplitudes[17] (i.e., form factors). To check whether the above results are dependent on the line shape, the resonance parameter fit was redone using a Gaussian line shape; both fits gave very similar values for the ψ'' resonance parameters even though the two line shapes are quite different. This cross check indicates that these results are reasonably independent of the assumptions which have been made regarding the line shape.

4.6 COMPARISON WITH OTHER EXPERIMENTS

The ψ'' resonance parameters have been measured by three previous experiments[15]: Delco, Lead Glass Wall, and Mark II. The Crystal Ball results are compared to these other experiments in table 2. All of the

experiments use the same technique and very similar ψ'' line shapes to determine the ψ'' resonance parameters. Also included in table 2 are the predictions of a potential model calculation.[17]

TABLE 2

ψ'' Resonance Parameters

Experiment	$M_{\psi''}-M_{\psi'}$ (MeV)	Γ_{ee} (eV)	Γ_{tot} (MeV)	$\bar{\sigma}_{\psi''}$ (nb)
Crystal Ball	84±3	283±70	34±8	6.7±0.9
Delco	86±2	180±60	24±5	≈6
Lead Glass Wall	88±3	345±85	28±5	≈10
Mark II	80±2	276±50	24±5	9.3±1.4
Potential Model	71	230	30	

Table 2 shows that this measurement of the ψ'' resonance parameters is in reasonably good agreement with the previous measurements. There is moderate disagreement among the previous measurements of the ψ'' mass: the Mark II experiment measures a mass which is 6-8 MeV lower than the values measured by Delco and the Lead Glass Wall. The Crystal Ball measurement of the ψ'' mass is only slightly lower (2-4 MeV) than the values measured by the Delco and Lead Glass Wall experiments; given the size of the experimental errors, this measurement is consistent with all previous measurements. The Crystal Ball measurement of the total width is somewhat larger than previous measurements, but the difference is not statistically significant. A simple comparison of the leptonic width

measurements is misleading. The resonance parameter fit accurately determines the ψ'' peak cross section, which is approximately proportional to Γ_{ee}/Γ_{tot}. This causes the fit to have a large correlation between the leptonic width and the total width, whereas a determination of the ψ'' peak cross section is nearly independent of the total width. Table 2 compares the measurements of $\bar{\sigma}_{\psi''}$, the ψ'' cross section at the resonance mass.[12] The Crystal Ball and Delco measurements of the ψ'' cross section are in good agreement, but the Lead Glass Wall and Mark II experiments measure a substantially larger cross section. No explanation for this discrepancy is offered except to note that the Crystal Ball measurement is relatively free of systematic uncertainties due to an accurate measurement of the integrated luminosity, a small point-to-point error in the cross section, and a high efficiency for detecting hadron events.

The potential model predictions given in table 2 are in very good agreement with the Crystal Ball measurements of the ψ'' resonance parameters. Although the potential model predicts that the ψ'' mass lies $\simeq$13 MeV lower than is observed, the authors of reference 17 note that the ψ'' mass prediction is sensitive to the details of their model. The potential model prediction of the total width of the ψ'' is relatively free of uncertainty and is in excellent agreement with the Crystal Ball measurement. The potential model prediction of the leptonic width includes contributions from both 1^3D_1-2^3S_1 mixing and relativistic corrections to the 1^3D_1 wave function. These two contributions are predicted to be approximately equal, which precludes a reliable calculation of the 1^3D_1-2^3S_1 mixing angle based upon the ψ'' leptonic width measurement.

Although the potential model prediction of the leptonic width is in agreement with the Crystal Ball measurement, a more precise comparison can be made by using the ratio Γ_{ee}/Γ_{tot}. The potential model predicts a value of 7.7×10^{-6} for this ratio, which is in very good agreement with the Crystal Ball measurement of $(8.3\pm1.3)\times10^{-6}$. Such good agreement between the predictions of the potential model and the Crystal Ball measurements is strong support for the interpretation of the ψ'' as the predominantly 1^3D_1 charmonium state.

Chapter V

THE ψ'' INCLUSIVE PHOTON SPECTRUM

The resonant production of a charmonium state by e^+e^- colliding beams is the cleanest laboratory for studying such a state. Unfortunately, only the $J^{PC}=1^{--}$ states (e.g., ψ, ψ', ψ'') can be produced directly by e^+e^- annihilation; the study of charmonium states with quantum numbers other than 1^{--} requires a different production mechanism. One such mechanism utilizes radiative transitions from an 1^{--} state to produce lower mass, positive C-parity charmonium states. The states produced in this manner can be identified by detecting the monochromatic photon which results from the transition.[1,3] The excellent photon energy resolution of the Crystal Ball detector makes it well suited for observing these transition photons in the inclusive photon spectrum. A previous work[8] has used the Crystal Ball detector to make an exhaustive study of radiative transitions from the ψ and ψ' states. This work found evidence for transitions from the ψ' to the χ_0, χ_1, χ_2, η_c and η_c' charmonium states. Evidence was also found for transitions from the ψ to the η_c and from the χ states to the ψ. In this chapter, the study of radiative transitions from charmonium states is extended to include transitions from the ψ''.

The ψ'' can make radiative transitions to any of the positive C-parity charmonium states which are lower in mass. Thus, transitions from the ψ'' to the χ_0, χ_1, χ_2, η_c, and η_c' states are allowed. Furthermore,

transitions to the 1^1D_2 charmonium state are allowed if it has a lower mass than the ψ''. Table 3 gives the predicted rates for these transitions based upon potential model calculations.[11,19,44] These calculations assume the ψ'' is a pure 1^3D_1 charmonium state; including a small admixture of the 2^3S_1 state does not significantly change the predicted transition rates. Table 3 also gives the predicted branching ratios for the radiative transitions. These branching ratios were calculated by dividing the predicted transition rates by the total width of the ψ'', which was taken to be 30 MeV. The branching ratios in table 3 are all quite small, the largest being 0.7% for the transition from the ψ'' to the χ_0 state. Transitions with such small branching ratios are not expected to be observable by this experiment given the size of the data sample (see section 5.2). Nevertheless, searching for such transitions provides a test of the charmonium theory since the observation of an anomalously large branching ratio would pose difficulties for the theory.

TABLE 3

Predicted ψ'' Radiative Transition Rates

Decay	E_γ (MeV)	Γ_γ (keV)	BR (%)
$1^3D_1 \rightarrow \gamma 1^3P_0$	338	221	0.7
$1^3D_1 \rightarrow \gamma 1^3P_1$	251	68	0.2
$1^3D_1 \rightarrow \gamma 1^3P_2$	208	3	0.01
$1^3D_1 \rightarrow \gamma 1^1D_2$	?	≈2	0.01
$1^3D_1 \rightarrow \gamma 1^1S_0$	707	small	-
$1^3D_1 \rightarrow \gamma 2^1S_0$	176	small	-

5.1 PHOTON SELECTION CRITERIA

The data sample for the inclusive photon analysis consists of 8401 hadron events taken near the peak of the ψ'' resonance (1755 nb^{-1} at E_{cm}=3771 MeV). The hadron events were selected by applying the restrictive hadron selection criteria described in section 4.1 to the data. In addition, events with fewer than four regions of energy deposit were eliminated from the data sample. The inclusive photon spectrum for these low multiplicity events is strongly influenced by the hadron selection cuts that remove radiative QED events. Removing these events prevents them from generating spurious peaks in the inclusive photon spectrum. Nearly all the events that survive these cuts are hadron events, ≈30% of which are ψ'' decays. Since this experiment has no way of distinguishing ψ'' events from non-resonant hadron events, the ψ'' inclusive photon spectrum will have a large background due to photons from non-resonant events. The effect of this background is to reduce the sensitivity of the experiment to radiative transitions from the ψ'' and introduce structure which is associated with the background events.

Each of the hadron events was examined for tracks which were cleanly identified as direct photons (as opposed to photons from π^0 decays). A track was identified as a direct photon if it satisfied the following requirements:

(1) The track was well contained within the Crystal Ball proper. This cut required $|\cos\theta|<0.85$, where θ is the angle between the track direction and the positron beam direction.

(2) The track was identified as neutral by the charged particle identification algorithms.

(3) The track was well separated from other tracks in the detector. This cut required $\cos\theta_{\gamma x} < 0.90$, where $\theta_{\gamma x}$ is the angle between the photon track and any other track.

(4) The track was a direct photon, not a π^0 decay photon. For each event, a global π^0 recognition algorithm was used to identify which pairs of neutral tracks, if any, were likely to be the decay photons of π^0s. The tracks identified as π^0 decay photons were eliminated from further consideration.

(5) The track had a pattern of energy deposit in the NaI crystals which was consistent with the expected pattern for a single photon. This requirement rejects tracks that have patterns usually associated with minimum ionizing charged particles, interacting hadrons, or overlapping photon showers.

These photon selection criteria are nearly identical to those used in reference 8; further details regarding the π^0 removal algorithm and the shower pattern cuts may be found in this reference.

5.2 INCLUSIVE PHOTON SPECTRUM

The inclusive photon spectrum is formed by making a histogram of the photon energy for all photons which pass the photon selection criteria described in section 5.1. Before considering the ψ'' inclusive photon spectrum, it is instructive to look at the photon spectrum of the ψ'. Since the ψ' spectrum has been thoroughly studied by a previous experiment,[8] it can be used to roughly calibrate the sensitivity of this experiment to structure in the ψ'' spectrum. To facilitate comparison of the two spectra, a subset of the ψ' data sample was used which contains

the same number of hadron events as the ψ'' data sample ($\simeq$ 40k hadron events). Figure 12 shows the ψ' inclusive photon spectrum for this subset of the data sample. Note that the photon energies in figure 12 are binned logarithmically, each bin covering a 3% interval in the photon energy. With this binning, the bin width is roughly equal to the detector resolution over most of the spectrum.

Several prominent peaks are visible in figure 12. The narrow peaks for photon energies of 125 MeV, 170 MeV, and 260 MeV are caused by radiative transitions from the ψ' to the χ_2, χ_1, and χ_0 states, respectively. The somewhat broader accumulation near 410 MeV is due to the doppler broadened transitions from the χ_1 and χ_2 states to the ψ in the cascade decay $\psi'\rightarrow\gamma\chi\rightarrow\gamma\gamma\psi$. The fractions of ψ' events which make these transitions have been measured to be (8.0±0.5)%, (9.0±0.5)%, (9.9±0.5)%, and (3.6±0.2)% for the peaks at 125 MeV, 170 MeV, 260 MeV, and 410 MeV, respectively.[8] These four peaks in the ψ' spectrum are unmistakable, which indicates that this experiment can easily detect transitions which occur in $\simeq$3% of the events. Figure 12 shows no significant structure for photon energies of 90 MeV or 630 MeV, where transitions from the ψ' to the η_c' and η_c states produce narrow peaks in larger data samples. The fraction of ψ' events which make transitions to the η_c and η_c' have been measured to be (0.28±0.06)% and (0.5-1.2)%. Thus, transitions which occur in less than $\simeq$1% of the events are not expected to be observed by this experiment. It should be noted that the above estimate of the experimental sensitivity is only a rough guideline; determining the actual sensitivity requires a careful analysis of the ψ'' spectrum.

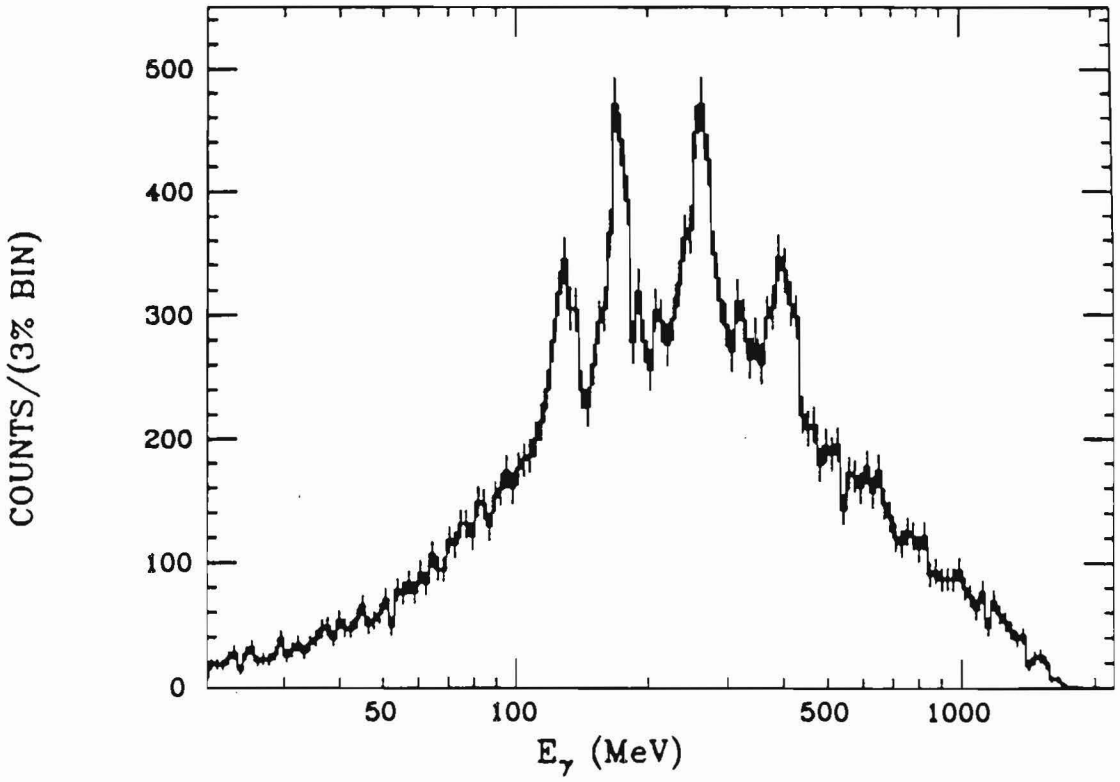

Figure 12: The inclusive photon spectrum of the ψ'.

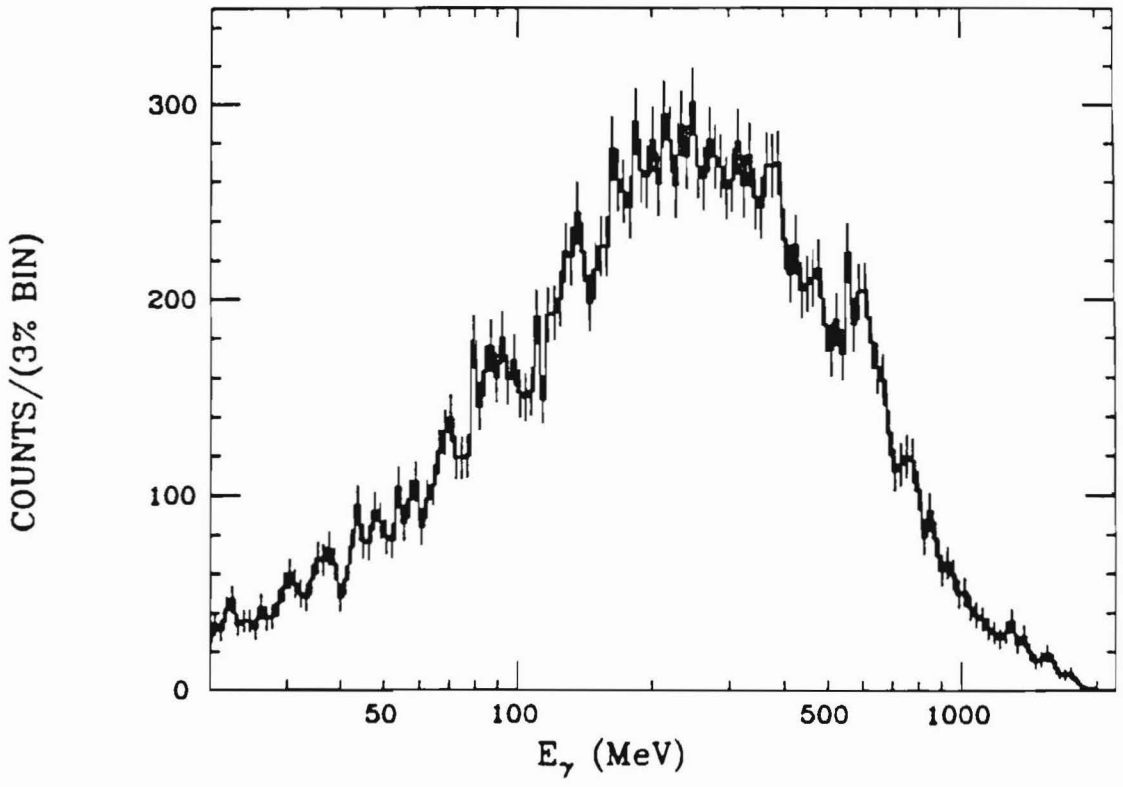

Figure 13: The inclusive photon spectrum of the ψ''.

The ψ'' inclusive photon spectrum is shown in figure 13. Two statistically significant structures are evident in this spectrum: an obvious peak at an energy of ≈600 MeV and a somewhat less pronounced peak at ≈90 MeV. The mean and amplitude of each peak were determined by fitting a gaussian line shape and an incoherent background to the region of the photon spectrum surrounding the peak. Figure 14 shows the result of a fit to the 600 MeV region. For this fit, the width of the gaussian line shape was fixed at the known detector resolution (σ_E=18 MeV for E_γ=600 MeV) and a second-order polynomial was used for the background shape. The fit gave a mean photon energy of 605±8 MeV and an amplitude of 115±33 counts for the signal (χ^2=24 for 21 degrees of freedom). A fit to the 90 MeV region of the photon spectrum is shown in figure 15. Once again, the width of the gaussian line shape was fixed at the detector resolution (σ_E=4.3 MeV for E_γ=90 MeV). Note that figure 15 is binned in 4% energy intervals to maintain a bin width which is approximately equal to the detector resolution. A good fit was obtained using a third-order polynomial background shape (χ^2=16 for 17 degrees of freedom). The fit gave a mean photon energy of 86.5±1.3 MeV and an amplitude of 156±38 counts for the signal. Since the center of mass energy is well known, the mass recoiling against the photons in each peak can be calculated. The recoil masses were determined to be 3107±15 MeV and 3683±3 MeV for the peaks at 605 MeV and 86.5 MeV, respectively.[45]

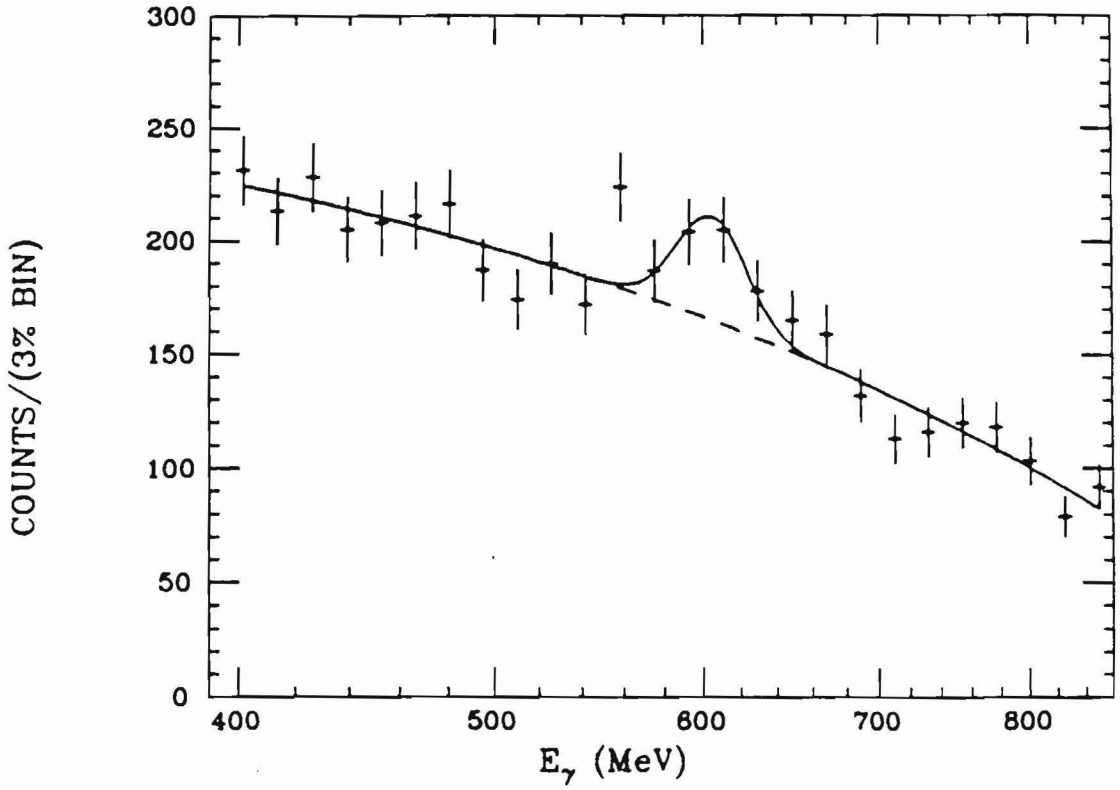

Figure 14: The ψ'' Inclusive Photon Spectrum for E_γ near 600 MeV.

The solid curve is the result of a fit to the spectrum using a gaussian line shape and a second-order polynomial background.

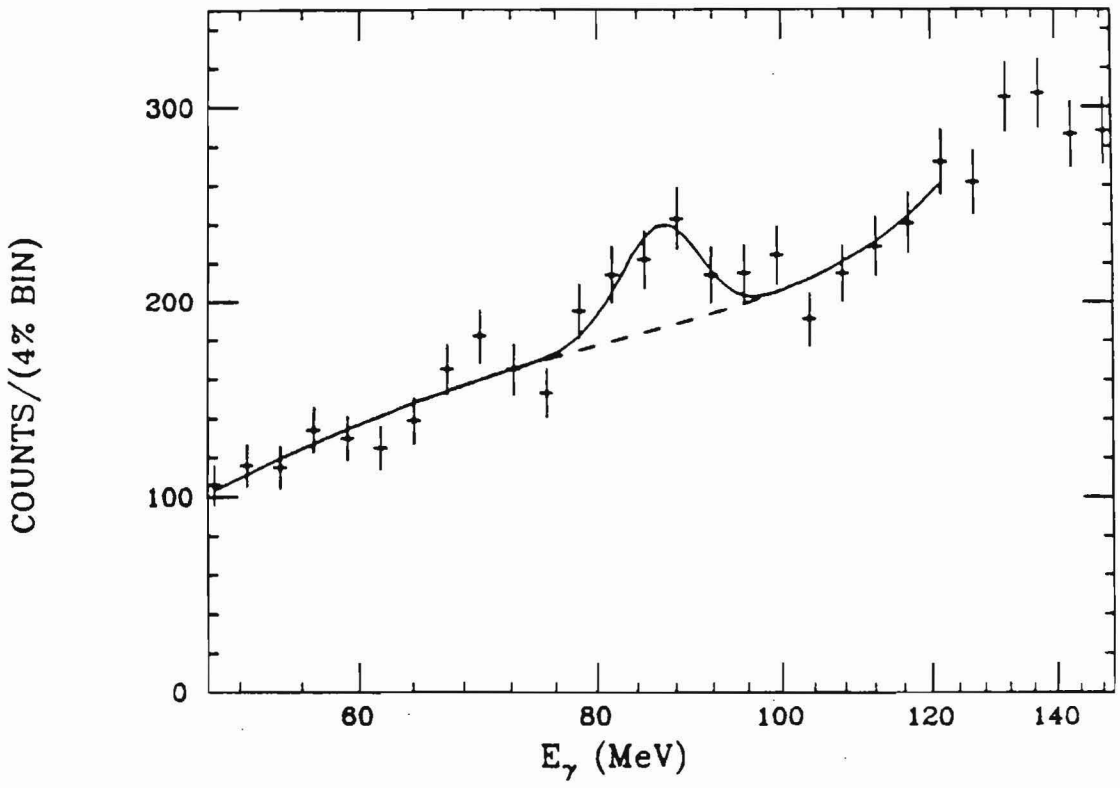

Figure 15: The ψ'' inclusive photon spectrum for E_γ near 90 MeV.

The solid curve is the result of a fit to the spectrum using a gaussian line shape and a third-order polynomial background.

5.3 INITIAL STATE RADIATION EFFECTS

The peaks in the inclusive photon spectrum at 90 MeV and 605 MeV cannot be identified with any allowed transition between known charmonium states. Although the recoil masses (3107±15 MeV and 3683±3 MeV) are very close to the ψ and ψ' masses (M_ψ=3095 Mev and $M_{\psi'}$=3684 MeV), radiative transitions from the ψ'' to the ψ or ψ' are forbidden because they do not conserve C-parity. There is, however, another way to produce a final state of a photon and a ψ or ψ' which has nothing to do with the ψ''. As discussed in section 4.3, one of the initial state electrons can radiate a photon and thereby lower the effective center of mass energy. The annihilation cross section increases by an enormous factor when the effective center of mass energy is equal to the ψ or ψ' mass, causing two narrow peaks in the spectrum of radiated photons. Since the ψ'' data sample contains a substantial number of radiative ψ and ψ' events, it is not surprising that these radiative photons appear as peaks in the photon spectrum.

The number of radiatively produced ψ or ψ' events is proportional to the integrated hadron cross section of the resonance, $A_\psi \equiv \int \sigma(e^+e^- \to \psi \to \text{hadrons}) dE_{cm}$. Thus, the number of photons in the peaks at 605 MeV and 86.5 MeV can be used to measure the integrated hadron cross sections of the ψ and ψ' resonances. Note that this method is quite different from the standard method for measuring the integrated hadron cross section of a narrow resonance. The standard method is to measure the hadron cross section across the resonance and fit the cross section to a radiatively corrected line shape, which tends to probe the soft photon radiative corrections, while this method probes the hard photon

corrections. If the current understanding of radiative corrections is accurate, the two methods should agree. For narrow resonances, the number of radiative photons is given by:

$$N_\gamma(\text{produced}) = \frac{tA\mathcal{L}}{k}\left[\frac{kt}{E^t} - \frac{k}{E} + \frac{k^2}{2E^2}\right]\left[\frac{E-k}{E}\right]^{1/2}$$

where k is the photon energy, t is a constant defined in section 4.3, A is the integrated hadron cross section of the resonance, $\mathcal{L}$ is the integrated luminosity, and E is the beam energy. The number of observed radiative photons is related to the number of produced photons as follows:

$$N_\gamma(\text{produced}) = \frac{N_\gamma(\text{observed})}{\epsilon_{had}\epsilon_{geom}\epsilon_\gamma}$$

where ϵ_{had}, ϵ_{geom}, and ϵ_γ are described below.

The hadron detection efficiency, ϵ_{had}, is the probability that a hadronic decay of the ψ or ψ' will pass the hadron selection cuts. A previous Crystal Ball study[8] found the hadron detection efficiency to be 0.94±0.05 for both the ψ and ψ'. With the slightly more restrictive hadron selection criteria used in the present analysis, the hadron detection efficiency is estimated to be ϵ_{had}=0.9±0.1.

The geometrical acceptance, ϵ_{geom}, is the fraction of radiative photons that enter the Crystal Ball detector and satisfy the solid angle cut in the photon selection criteria. Only a small fraction of the radiative photons enter the detector because the angular distribution for these photons is strongly peaked along the beam direction[39]:

$$\frac{dN}{d(\cos\theta)} \propto \frac{\sin^2\theta}{1-\beta^2\cos^2\theta}$$

where θ is the angle between the photon direction and the beam direction and β is the velocity of the electrons in the center of mass (β=1). The geometrical acceptance was determined to be ϵ_{geom}=0.15 by integrating the above angular distribution over the allowed region of solid angle ($|\cos\theta|<0.85$).

The photon detection efficiency, ϵ_γ, is the probability that a radiative photon within the geometrical acceptance was counted when the peak in the inclusive photon spectrum was fit. For a photon to be counted, it must pass the photon selection criteria (see section 5.1) and it must have a properly measured energy.[96] The photon detection efficiency was determined by a Monte Carlo technique that simulates the inclusive photon analysis.[97] For a given photon energy, a sample of Monte Carlo photon showers was generated using the Electron-Gamma Shower (EGS) program.[98] Radiative events were simulated by adding the Monte Carlo generated showers to events from the ψ data sample. These events were then mixed into a much larger sample of events that did not contain a Monte Carlo photon, to produce an inclusive photon spectrum with an additional structure due to the Monte Carlo photons. The number of photons in the peak was determined by fitting the inclusive spectrum, and the photon detection efficiency is the fraction of the generated Monte Carlo photons counted in the peak after correcting for the 3.5% probability that a photon will convert in the beam pipe or tracking chambers and be misidentified as a charged particle. Figure 16 shows the photon detection efficiency as a function of the photon energy. Note that the measurement errors shown in figure 16 are the statistical errors, and do not include a common systematic error which is estimated to be ±15% of

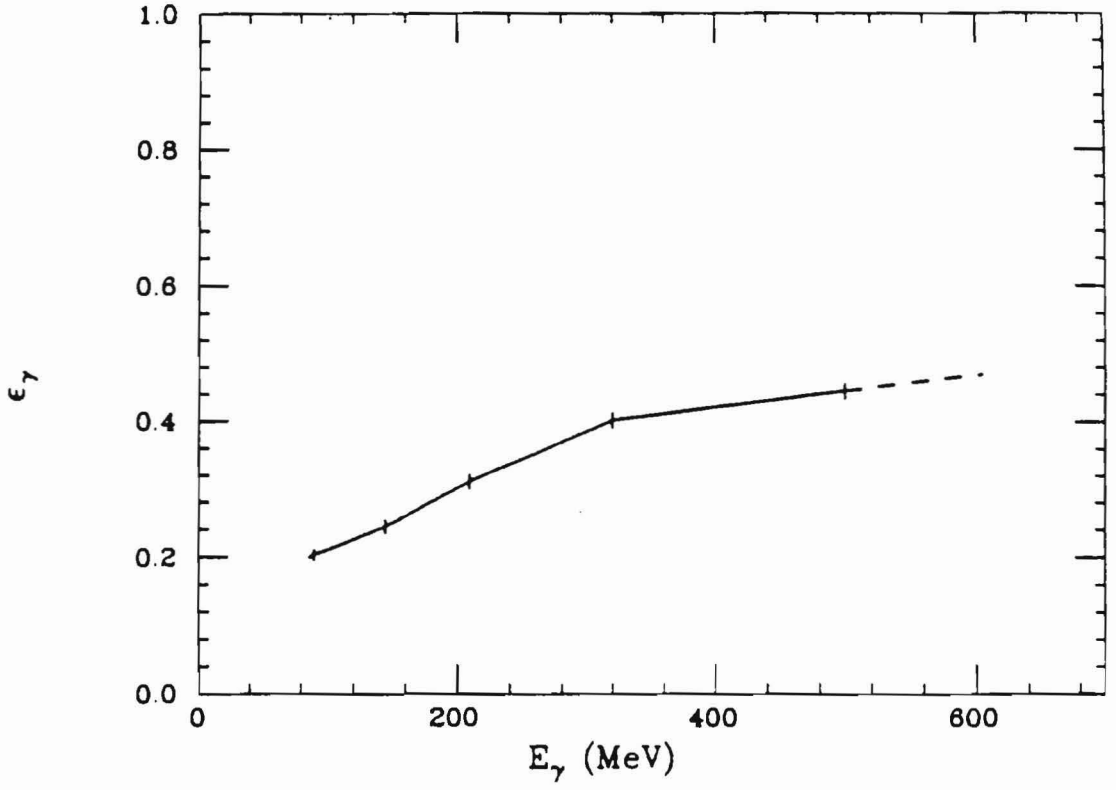

Figure 16: The photon detection efficiency.

The error bars are statistical only, and do not include the systematic error, which is estimated to be ±15% of the efficiency. The dashed line shows an extrapolation of the measurements to E_γ=605 MeV.

the efficiency. Extrapolating these measurements to 605 MeV gives a photon detection efficiency of ϵ_γ=0.47±0.07. A somewhat lower value is obtained for 86.5 MeV photons: ϵ_γ=0.19±0.03. The fall-off in efficiency for low energy photons is due to several factors: low energy photons are more frequently misidentified as π^0 decay photons, they are more likely to fail the pattern cut because of shower fluctuations, and a small energy mismeasurement is more likely to move the photons out of the peak.

Assuming that the peaks in the inclusive photon spectrum are due to radiative ψ and ψ' production, the integrated hadron cross sections can be measured for these resonances. For the ψ, 115±33 photons were detected with an overall efficiency of 0.063±0.012, giving an integrated hadron cross section of A_ψ=16±5 nb-GeV. For the ψ', 156±38 photons were detected with an overall efficiency of 0.026±0.005, giving $A_{\psi'}$=5.2±1.7 nb-GeV. Previous experiments have measured the leptonic width and the branching ratio to hadrons for these resonances, which are related to the integrated hadron cross section as follows:

$$A_\psi = \frac{6\pi^2}{M_\psi^2} \Gamma_{ee} BR(\psi \rightarrow \text{hadrons}).$$

Using the established values[36] for the leptonic width and the branching ratio to hadrons gives integrated hadron cross sections of A_ψ=9.6±0.8 nb-GeV and $A_{\psi'}$=3.4±0.3 nb-GeV. The established values for A_ψ and $A_{\psi'}$ are slightly lower than the above measurements, but the differences are not statistically significant.

The ψ'' photon spectrum in figure 13 doesn't show any other obvious structures. A 95% confidence level upper limit of 10% is obtained for

the branching ratio $BR(\psi'' \to \gamma X)$, where $E_\gamma > 100$ MeV and X is a narrow state.[99] Radiative transitions from the ψ'' are expected to have branching ratios that are much smaller than 10% (see table 3), so this limit is not in conflict with the charmonium model predictions.

Chapter VI

A SEARCH FOR NEUTRAL DECAY MODES OF THE D^0

The last two chapters have focused on specific properties of the ψ'', with emphasis placed upon testing the predictions of potential models. Although these chapters frequently assume that $D\bar{D}$ is the dominant decay mode of the ψ'', the properties of the D mesons have been largely ignored. This situation is reversed in the present chapter: the focus is on the D mesons themselves, with little consideration given to the properties of the ψ''. There is also a major difference in the underlying physics that is being studied. The D mesons are the lowest lying charmed particles, so their decays are mediated by the weak interaction (the strong and electromagnetic interactions conserve the charm quantum number). Thus, the properties of the D mesons are heavily influenced by the charm changing components of the weak interaction, whereas the properties of the ψ'' are determined by the quark-antiquark potential due to the strong interaction. One way to probe the charm changing components of the weak interaction is to study the rates for various D meson decay modes. The Crystal Ball has the unique ability to study D^0 final states composed entirely of photons; previous experiments have only searched for final states with at least two charged particles. This chapter uses the ψ'' data sample to search for several neutral decay modes of the D^0.

6.1 PRODUCTION OF D MESONS AT THE ψ''

There are several reasons why the ψ'' was chosen for a study of D meson properties:

(1) The decay $\psi''\rightarrow D\bar{D}$ is allowed by the OZI rule and is expected to predominate over radiative and OZI suppressed decay modes (see chapter 1). This expectation is supported by the large width of the ψ'' relative to the ψ' (see section 4.5) and previous observations[20] of copious D production at the ψ''.

(2) The ψ'' is below threshold for other OZI allowed decay modes (e.g., $D\bar{D}^*$, $D\bar{D}\pi$, $F\bar{F}$), making $D\bar{D}$ the only OZI allowed decay mode. This decay mode is the simplest and most direct source of D mesons.

(3) Since the ψ'' is at rest in the lab frame, the D mesons evenly split the center of mass energy. This leaves the D mesons with only $\approx$20 MeV of kinetic energy, which substantially reduces backgrounds for this experiment.

(4) Assuming that the decay $\psi''\rightarrow D\bar{D}$ is dominant, the D meson cross section is quite large: σ_D=12.8$\pm$1.8 nb at E_{cm}=3771 MeV (see section 4.5).

The above characteristics make the ψ'' an ideal place to study the properties of D mesons.

6.2 THEORETICAL MOTIVATION

For a D meson to decay, the weak interaction must couple to the charm quark and turn it into either a down quark or a strange quark.[50] In the "standard model," this coupling occurs at a vertex joining the quark lines to a W boson[10,51] (see figure 17 for examples of diagrams

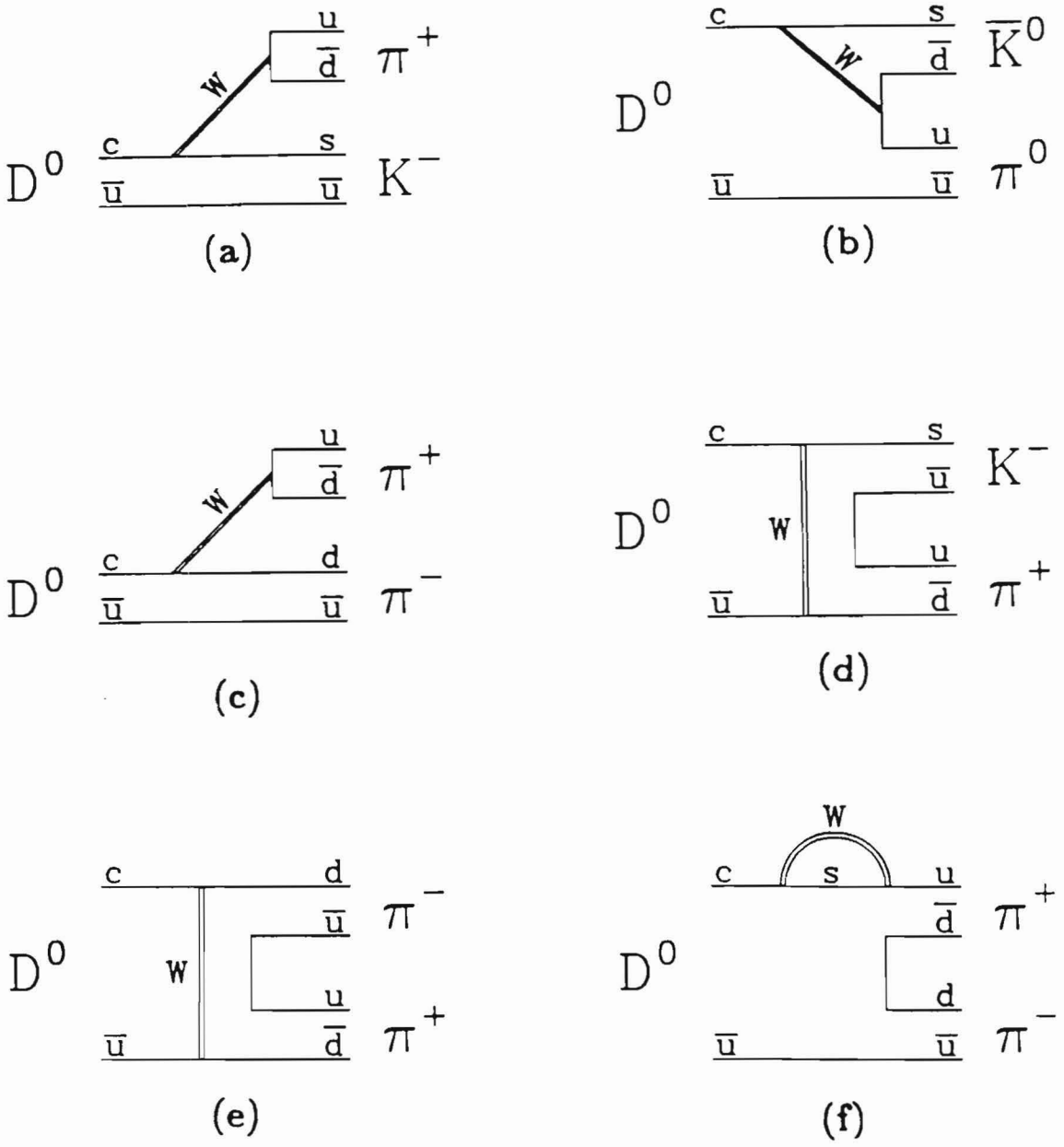

Figure 17: Examples of diagrams that contribute to D^0 decay.

(a) A spectator diagram for the decay $D^0 \to K^- \pi^+$; (b) a spectator diagram for the decay $D^0 \to \bar{K}^0 \pi^0$; (c) a spectator diagram for the decay $D^0 \to \pi^- \pi^+$; (d) an annihilation diagram for the decay $D^0 \to K^- \pi^+$; (e) an annihilation diagram for the decay $D^0 \to \pi^- \pi^+$; (f) a penguin diagram for the decay $D^0 \to \pi^- \pi^+$.

that contribute to D^0 decay). The physics associated with this vertex is contained in the hadronic component of the weak interaction "charged current":

$$J_\mu = \bar{u}\gamma_\mu\frac{(1-\gamma_5)}{2}d' + \bar{c}\gamma_\mu\frac{(1-\gamma_5)}{2}s' + \bar{t}\gamma_\mu\frac{(1-\gamma_5)}{2}b'$$

where $\bar{u}$, $\bar{c}$, and $\bar{t}$ are annihilation operators for the up, charm, and top quarks; d', s', and b' are creation operators for the weak interaction eigenstates; and the $\gamma_\mu(1-\gamma_5)$ factor causes the current to have a parity violating, V-A form. The d', s', and b' eigenstates are related to the down (d), strange (s), and bottom (b) quarks by a mixing matrix which must be determined experimentally. This mixing matrix can be written as follows:

$$\begin{pmatrix} d' \\ s' \\ b' \end{pmatrix} = \begin{pmatrix} V_{ud} & V_{us} & V_{ub} \\ V_{cd} & V_{cs} & V_{cb} \\ V_{td} & V_{ts} & V_{tb} \end{pmatrix} \begin{pmatrix} d \\ s \\ b \end{pmatrix}$$

where, for example, V_{ud} gives the strength of u-d coupling in the weak current. The elements of the mixing matrix that relate to D decay are V_{cd} and V_{cs}, the strengths of the c-d and c-s couplings (V_{cb} can be ignored since the D meson is below threshold for decays involving b quarks).

In the six-quark standard model, the mixing matrix is unitary and can be rewritten as

$$\begin{pmatrix} d' \\ s' \\ b' \end{pmatrix} = \begin{pmatrix} c_1 & s_1c_3 & s_1s_3 \\ -s_1c_2 & c_1c_2c_3+s_2s_3e^{i\delta} & c_1c_2s_3-s_2c_3e^{i\delta} \\ -s_1s_2 & c_1s_2c_3-c_2s_3e^{i\delta} & c_1s_2s_3+c_2c_3e^{i\delta} \end{pmatrix} \begin{pmatrix} d \\ s \\ b \end{pmatrix}$$

where θ_1, θ_2, θ_3, and δ are the Kobayashi-Maskawa[52] angles ($c_i=\cos\theta_i$, $s_i=\sin\theta_i$). Recent measurements indicate that the b quark has a relatively long lifetime, which implies that the b quark couples very weakly

to the u and c quarks.[53] By combining these lifetime measurements with several other experiments, fairly strict limits can be placed on three of the Kobayashi-Maskawa angles[54]:

$$\sin\theta_1 = 0.231\pm0.003$$
$$0.015 < \sin\theta_2 < 0.09$$
$$0.0 < \sin\theta_3 < 0.04.$$

Alternatively, these experiments can be used to determine the following 1 standard deviation intervals for V_{cd} and V_{cs}:

$$-0.234 < V_{cd} < -0.228$$
$$0.9704 < V_{cs} < 0.9726.$$

In the limit of a stable b quark, θ_2 and θ_3 are identically zero and the mixing matrix reduces to the Cabibbo mixing matrix,

$$\begin{pmatrix} d' \\ s' \\ b' \end{pmatrix} = \begin{pmatrix} \cos\theta_C & \sin\theta_C & 0 \\ -\sin\theta_C & \cos\theta_C & 0 \\ 0 & 0 & 1 \end{pmatrix} \begin{pmatrix} d \\ s \\ b \end{pmatrix}$$

where θ_C is the Cabibbo angle ($\theta_C \equiv \theta_1$). Taking $\sin\theta_C = 0.231\pm0.003$ gives values for V_{cd} and V_{cs} which are nearly identical to those obtained above using the Kobayashi-Maskawa mixing matrix. The Cabibbo mixing matrix is frequently used in this chapter because it shows more clearly how mixing affects D meson decay.

An important test of the standard model is to compare the predicted values for V_{cd} and V_{cs} with a direct measurement of these quantities. A large discrepancy could indicate a serious breakdown in the standard model, while a small disagreement could occur if the b quark lifetime experiments are incorrect or if there is a new quark flavor that couples to the charm quark. In principle, the ratio $|V_{cd}|/|V_{cs}|$ can be determined by measuring the branching ratios for various decay modes of the D mesons. The semileptonic decay modes may be particularly well suited to measuring this ratio, but this experiment is not sensitive to these

modes. Trying to measure this ratio using hadronic decay modes is complicated by the possibility that several diagrams could be contributing to the decay.[55]

Figure 17 shows the diagrams that can contribute to the $D^0 \to K^-\pi^+$ and $D^0 \to \pi^-\pi^+$ decay modes (strong interaction effects have been ignored in these diagrams). From these diagrams, it is clear that S=-1 final states of the D meson will have an amplitude proportional to $V_{cs}V_{ud}$, S=0 final states can have both $V_{cs}V_{us}$ terms and $V_{cd}V_{ud}$ terms in the amplitude, and S=1 final states have an amplitude proportional to $V_{cd}V_{us}$. The relative strength of these terms becomes clear if a Cabibbo mixing matrix is assumed. In this case, the S=0 final state will be suppressed by a factor of $\tan^2\theta_C$ relative to the S=-1 final states (the S=1 final states are so heavily suppressed they are not considered further). For a Cabibbo angle given by $\sin\theta_C=0.231$, the suppression factor is $\simeq 18$. The S=-1 final states of the D are often called "Cabibbo-favored," while the S=0 final states are "Cabibbo-suppressed." Measuring this suppression factor is one way to probe the ratio $|V_{cd}|/|V_{cs}|$.

The diagrams in figure 17 can be divided into three categories: the spectator diagrams, where the non-charmed quark of the D is a "spectator," and is not involved in the weak interaction; the annihilation diagrams, where a W is exchanged between the quarks in the D meson; and the penguin diagram, where a W boson couples twice to the same quark line and changes the charm quark to an up quark. Note that the penguin diagram can only contribute to the Cabibbo-suppressed decay modes; annihilation diagrams for the D^+ are also Cabibbo suppressed. Early attempts[56] to predict the relative rates for hadronic D decays focused

on the spectator diagram, since helicity arguments suggested that the annihilation diagram is heavily suppressed. More recent work[57] suggests that the effects of gluons may cause the annihilation diagram to be dominant. Establishing the relative importance of these three types of diagrams is an important goal in the study of D meson properties.

One way to clarify the role of these different diagrams is to measure several different decay modes of the D mesons and compare the relative rates with predictions based on the different diagrams. For example, the spectator model[56] can be used to predict the relative rates for the decay of a D^0 into various pairs of pseudoscalers. Definite predictions can be made by assuming SU(3) symmetry and the dominance of a particular piece of the weak interaction which may be responsible for the $\Delta I=1/2$ rule in K decay[58] (i.e., "sextet dominance"). Table 4 gives the relative rates predicted by the sextet dominance model for several decay modes relevant to this thesis. Note that these predictions will change if sextet dominance is invalid or non-spectator diagrams make important contributions. In particular, the decay rate for $D^0 \to \bar{K}^0\eta$ is expected to be highly suppressed if the annihilation diagram dominates.[59]

This experiment attempts to increase our understanding of D^0 decays by searching for previously unobserved decay modes of the D^0. Since the Crystal Ball does not measure the momentum of charged particles, it is necessary to restrict the analysis to D^0 final states composed entirely of photons. The following decay modes were searched for: $\pi^0\pi^0$, $\eta\pi^0$, $\eta\eta$, $\pi^0\pi^0\pi^0$, and $\eta\pi^0\pi^0$. The Crystal Ball is well suited to searching for these decay modes because of its excellent photon energy resolution, a

TABLE 4

Predictions of the Sextet Dominance Model

DECAY MODE	RELATIVE RATE
$K^-\pi^+$	1
$\bar{K}^0\pi^0$	1/2
$\bar{K}^0\eta$	1/6
K^+K^-	$1\ \tan^2\theta_C$
$\pi^+\pi^-$	$1\ \tan^2\theta_C$
$\pi^0\pi^0$	$1/2\ \tan^2\theta_C$
$\eta\pi^0$	$1/3\ \tan^2\theta_C$
$\eta\eta$	$1/2\ \tan^2\theta_C$

feature which is not matched by the more conventional magnetic detectors. The $\pi^0\pi^0$, $\eta\pi^0$, and $\eta\eta$ decay modes are necessarily Cabibbo-suppressed, and are expected to be fairly rare. The $\pi^0\pi^0\pi^0$ and $\eta\pi^0\pi^0$ decay modes are expected to have contributions from the Cabibbo-favored $K_S\pi^0$ and $K_S\eta$ decays, where the K_S decays to $\pi^0\pi^0$, as well as possible Cabibbo-suppressed contributions. Decays of the D^0 into other decay modes involving π^0, η, or η' mesons were not considered because the reconstruction efficiency is negligible.

6.3 π^0 AND η RECONSTRUCTION

All the D^0 decay modes being searched for contain π^0 and/or η mesons, so the first step in this search is to identify the photons in each event and determine which pairings of photons are consistent with a π^0 or η interpretation. Tracks that satisfied the following criteria were identified as photons:

(1) The track must have been identified as neutral by the charged particle reconstruction algorithms.

(2) The track must be within the Crystal Ball proper and have $|\cos\theta_\gamma| < 0.9$, where θ_γ is the angle of the track with respect to the beam direction.

(3) The track must have a measured energy greater than 20 MeV.

(4) The track must not lie in a connected region identified as a merged π^0 by the PIFIT algorithm (see section 3.4).

(5) The track must not lie in the same connected region as a charged particle. Furthermore, there must not be any other neutral tracks in the connected region with $\cos\theta_{\gamma\gamma} > 0.85$, where $\theta_{\gamma\gamma}$ is the angle between the track under consideration and another neutral track.

Photons which lie in a connected region identified as a merged π^0 by the PIFIT algorithm were treated separately.

If two or more photons were found, a search was made for pairs of photons that could be reconstructed to form π^0 or η mesons. Figure 18 shows the $\gamma\gamma$ mass spectrum for all pairs of photons. A prominent peak is observed at the π^0 mass, but the η signal is buried under a combinatoric background caused by incorrect pairings of π^0 photons. To demonstrate that there are η mesons in the data, all photons which could be paired with another photon to form a mass consistent with the π^0 mass were eliminated; the $\gamma\gamma$ mass spectrum for the remaining photons shows a clear peak near the η mass (see figure 19). A preliminary identification of π^0 and η candidates was made by making loose cuts on the $\gamma\gamma$ mass:

$$|M_{\gamma\gamma} - M_{\pi^0}| < 60 \text{ MeV} \quad \text{for } \pi^0\text{s}$$
$$|M_{\gamma\gamma} - M_{\eta}| < 90 \text{ MeV} \quad \text{for } \eta\text{s}.$$

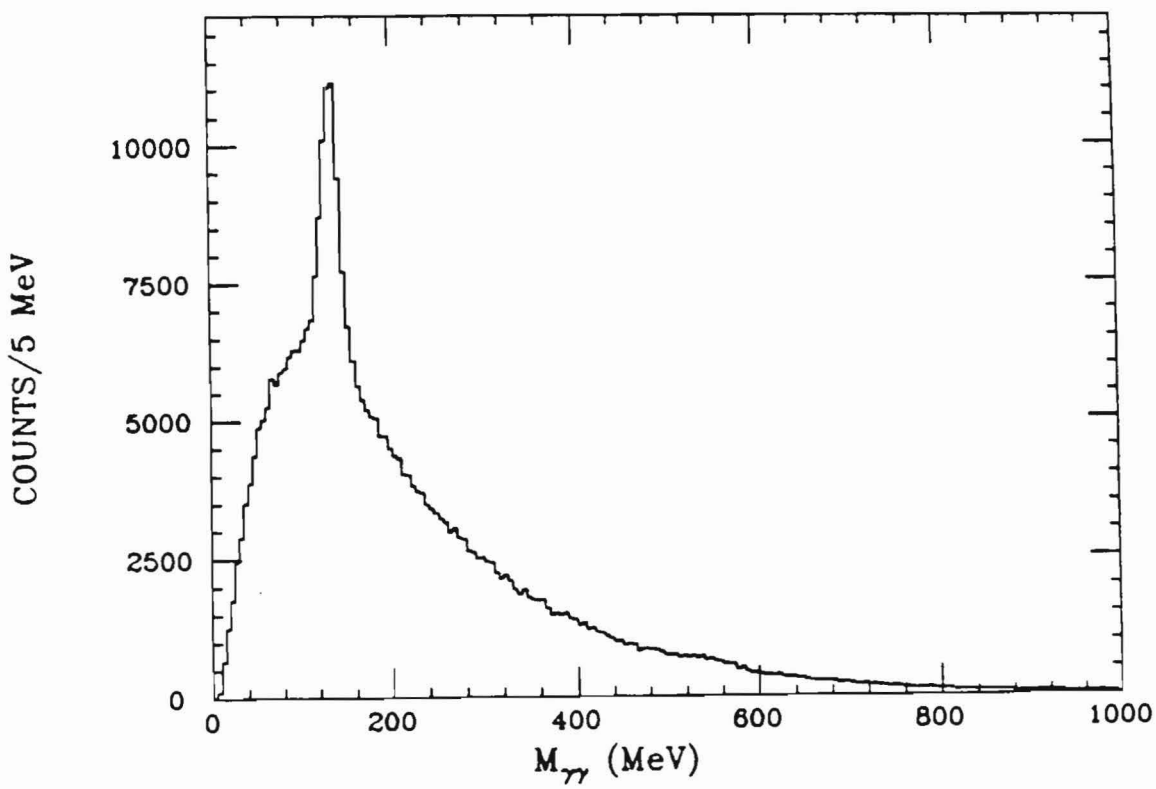

Figure 18: $M_{\gamma\gamma}$ for all pairs of photons.

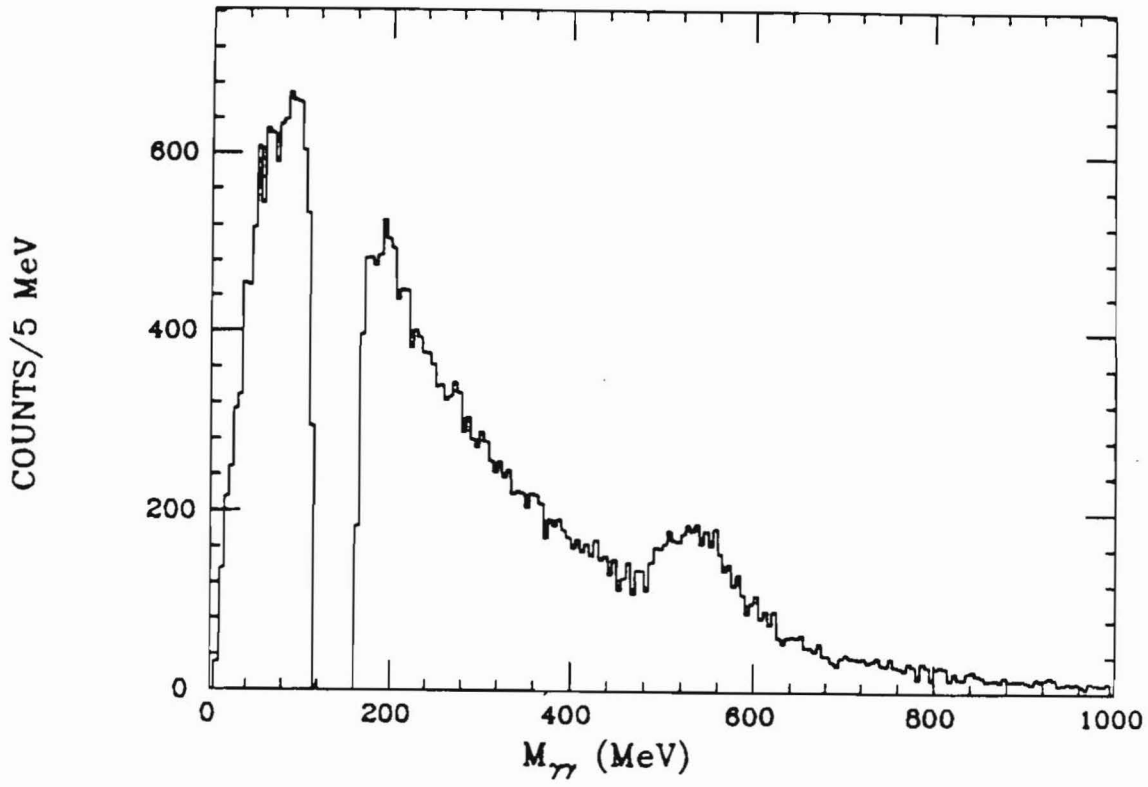

Figure 19: $M_{\gamma\gamma}$ after π^0 removal.

Those pairs that were identified as π^0 candidates were kinematically fit by minimizing a χ^2 given by

$$\chi^2 = \frac{(E^f_1-E^m_1)^2}{\sigma_{E_1}{}^2} + \frac{(E^f_2-E^m_2)^2}{\sigma_{E_2}{}^2} + \frac{(\theta^f_{12}-\theta^m_{12})^2}{\sigma_{\theta_{12}}{}^2}$$

subject to a constraint on the $\gamma\gamma$ mass

$$2E^f_1E^f_2(1-\cos\theta^f_{12}) = M^2$$

where:
- E^f_1 is the fitted energy for γ_1
- E^f_2 is the fitted energy for γ_2
- θ^f_{12} is the fitted opening angle between γ_1 and γ_2
- E^m_1 is the measured energy for γ_1
- E^m_2 is the measured energy for γ_2
- θ^m_{12} is the measured opening angle between γ_1 and γ_2
- σ_{E_1} is the measurement error in E^m_1
- σ_{E_2} is the measurement error in E^m_2
- $\sigma_{\theta_{12}}$ is the measurement error in θ^m_{12}
- M is the mass of the π^0 meson.

Each measurement error was set equal to the detector resolution for the quantity (see section 3.2).[60] If the χ^2 for the fit was less than 20, the pairing was entered into a list of π^0 mesons. The above kinematic fitting procedure was also applied to the η meson candidates, and candidates that had a χ^2 less than 20 were entered into a list of η mesons.

Several of the D^0 decay modes being studied in this chapter generate π^0 mesons with energies up to ≈1100 MeV. If the π^0 energy is above ≈700 MeV, the decay photons frequently have overlapping shower patterns which are not properly reconstructed by the offline analysis code. The PIFIT algorithm was developed to solve the problem of identifying and reconstructing these merged π^0s (see appendix A). All connected regions identified as merged π^0s using the criteria listed in section 3.4 were entered into the list of π^0s.

A χ^2 was calculated for each merged π^0 as follows[61]:

$$\chi^2 = \frac{(M_{\gamma\gamma}-M_{\pi^0})^2}{\sigma_{\gamma\gamma}^2}$$

where $M_{\gamma\gamma}$ is the connected region mass determined by PIFIT, M_{π^0} is the π^0 mass, and $\sigma_{\gamma\gamma}$ is the mass resolution for merged π^0s (see appendix A). This χ^2 is used below to aid in rejecting connected regions misidentified as merged π^0s.

6.4 A SEARCH FOR NEUTRAL DECAYS OF THE D^0

6.4.1 The analysis technique

This section describes the results of a search for D^0 mesons that decay into final states composed of π^0 and η mesons. The following Cabibbo-suppressed final states were investigated: $\pi^0\pi^0$, $\pi^0\eta$, $\eta\eta$, $\pi^0\pi^0\pi^0$, and $\pi^0\pi^0\eta$. In addition, the $\pi^0\pi^0\pi^0$ final state was used to search for the Cabibbo-favored decay $D^0\rightarrow K_S\pi^0$, where $K_S\rightarrow\pi^0\pi^0$. The analysis technique was essentially the same for all decay modes. Events were eliminated if there were insufficient π^0 and η mesons reconstructed to form the desired final state. For the surviving events, all possible combinations of π^0 and η mesons that gave the desired final state were made (combinations that used the same photon twice were eliminated).

To help decide which combinations were consistent with D^0 decay, the following quantities were calculated:

$$E_{tot} = \sum_i E_i$$

$$P_{tot} = \left|\sum_i \vec{p}_i\right|$$

$$\chi^2_{tot} = \sum_i \chi^2_i$$

where the sum is over the π^0 and η mesons in the combination and E_i, $\vec{p}_i$, and χ^2_i are the reconstructed energy, momentum, and χ^2 for the ith π^0 or η. It was noted above that the D^0 mesons have an energy equal to the beam energy, so combinations which are due to D^0 decay should have E_{tot}=1885.5 MeV. Note that a kinematic fit could have been done to constrain E_{tot} to the beam energy, but this would have made it very difficult to do a background subtraction. Since the D^0 has a fixed energy, the total momentum is related to the mass by

$$P_{tot} = \sqrt{E^2 - M_{D^0}^2}$$

where E=1885.5 MeV is the beam energy and M_{D^0}=1863.5 MeV is the D^0 mass.[62] Thus, D^0 final states should have P_{tot}=287 MeV. The third quantity calculated, the total χ^2 from the reconstructed π^0 and η mesons, is used to reject those combinations which are likely to have one or more misidentified π^0 or η mesons. The expected χ^2 distributions are somewhat different for 4-photon and 6-photon final states, so the confidence level was calculated from the χ^2 and the number of degrees of freedom[63] (4-photon final states have 2 degrees of freedom; 6-photon final states have 3). Properly reconstructed D^0 final states should have a uniform confidence level distribution, whereas combinations using misidentified

π^0 or η mesons should have a confidence level distribution strongly peaked at zero. In the analysis technique used below, combinations with a low confidence level are rejected, and a scatterplot is made of P_{tot} versus E_{tot} for the surviving combinations. A clustering of events with E_{tot}=1886 MeV, P_{tot}=287 MeV would indicate the presence of the D^0 final state being searched for.

6.4.2 The Monte Carlo

A Monte Carlo simulation was done for each decay mode to check the analysis procedure and calculate the efficiencies. The Monte Carlo was programmed to generate $\psi'' \to D^0\bar{D}^0$ events with the angular distribution appropriate for spin 0 D mesons (see section 4.4). One of the D^0 mesons was allowed to decay according to a model described in appendix B, while the other was forced to decay into the final state being searched for. A full detector simulation was done, and the events were analyzed in the same manner as the data, including the calculation of E_{tot}, P_{tot}, and the confidence level for the combination of π^0 and η being searched for. In the analysis that follows, the observed distributions are frequently compared with the same distributions for the Monte Carlo simulated events to demonstrate what the expected distributions should be. The simulated events were also used to determine the location of cuts on the data and to measure the efficiency for reconstructing the various decay modes.

6.4.3 An illustration: $\chi_0 \to \pi^0\pi^0$

Before using the above technique to search for various D^0 final states, it is useful to illustrate the technique by reconstructing $\chi_0 \to \pi^0\pi^0$ decays, where the χ_0 is produced by the reaction $\psi' \to \gamma\chi_0$.[64] The usefulness of this illustration lies in the fact that a reasonably large sample of $\chi_0 \to \pi^0\pi^0$ decays can be easily identified, with almost no background from other sources. These χ_0 mesons have a fixed energy and momentum (E_χ=3420 MeV, P_χ=260 MeV), so the above analysis technique can be applied to the χ_0 decays. The only significant difference between reconstructing $\chi_0 \to \pi^0\pi^0$ and $D^0 \to \pi^0\pi^0$ decays is that the χ_0 energy is almost twice as large as the D^0 energy, which causes almost all of the π^0s to be merged.

Events were selected if they contained a photon, two merged π^0s, and satisfied a cut on energy and momentum balance. Both the χ_2 and χ_0 mesons have $\pi^0\pi^0$ decay modes; χ_2 events were eliminated by rejecting events with $105 < E_\gamma(\text{MeV}) < 145$, where E_γ is the energy of the radiative photon ($E_\gamma \approx 125$ MeV for χ_2 events, $E_\gamma \approx 260$ MeV for χ_0 events). The confidence level, E_{tot}, and P_{tot} were calculated for the surviving events. For the purposes of comparison, $\psi' \to \gamma\chi_0$, $\chi_0 \to \pi^0\pi^0$ Monte Carlo events were generated and the response of the detector to these events was simulated[41]. The Monte Carlo events were analyzed the same way as the actual data, and the confidence level, E_{tot}, and P_{tot} were calculated for the events that passed all the cuts. Figure 20 shows the confidence level distribution for Monte Carlo events and for the data. Both distributions appear to be fairly constant, indicating that the correct error was used in calculating the χ^2 for PIFIT π^0s. Figure 21(b) shows

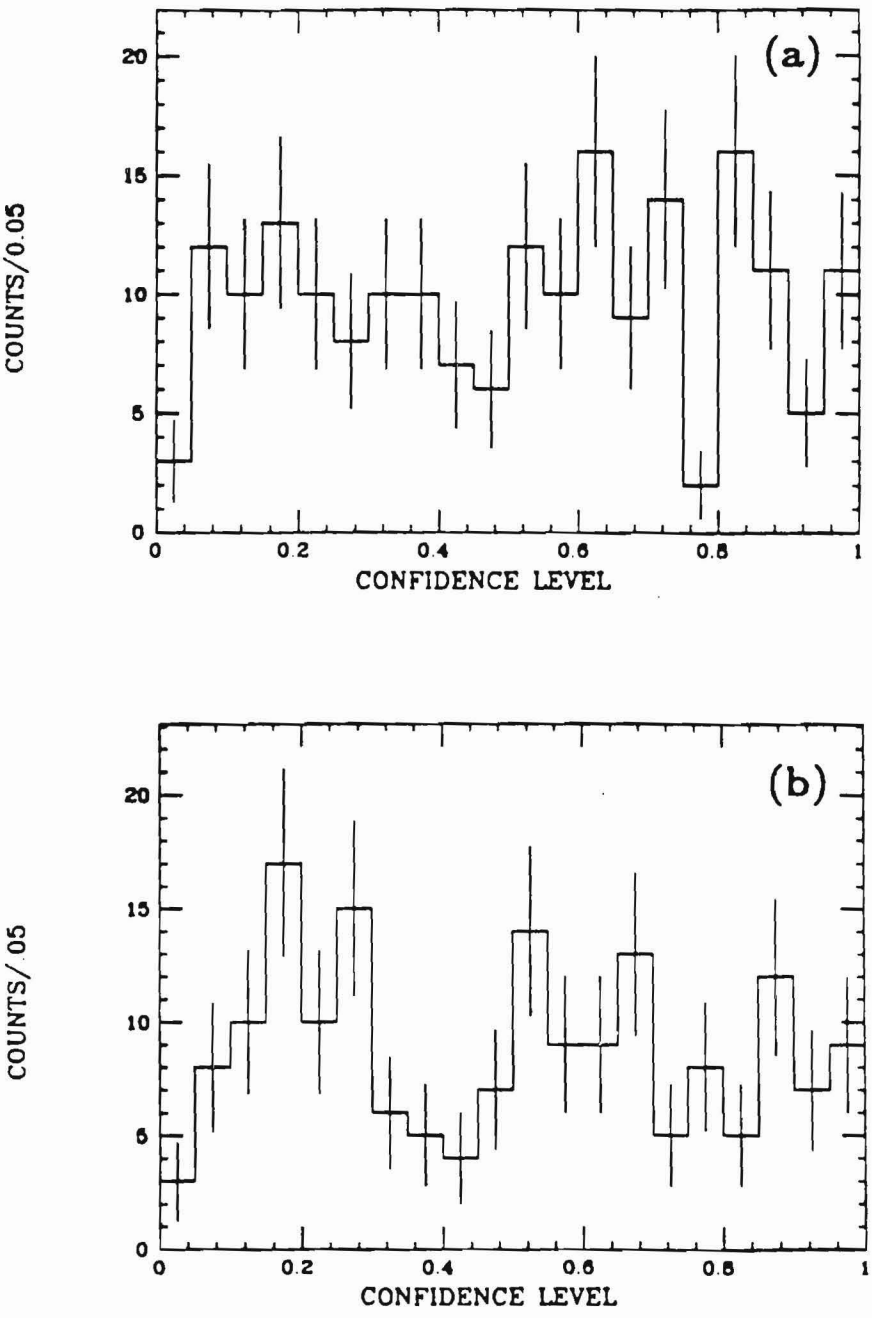

Figure 20: Confidence level distribution for $\chi_0 \to \pi_0\pi_0$ decays.

(a) Monte Carlo events; (b) $\psi' \to \gamma\pi^0\pi^0$ events.

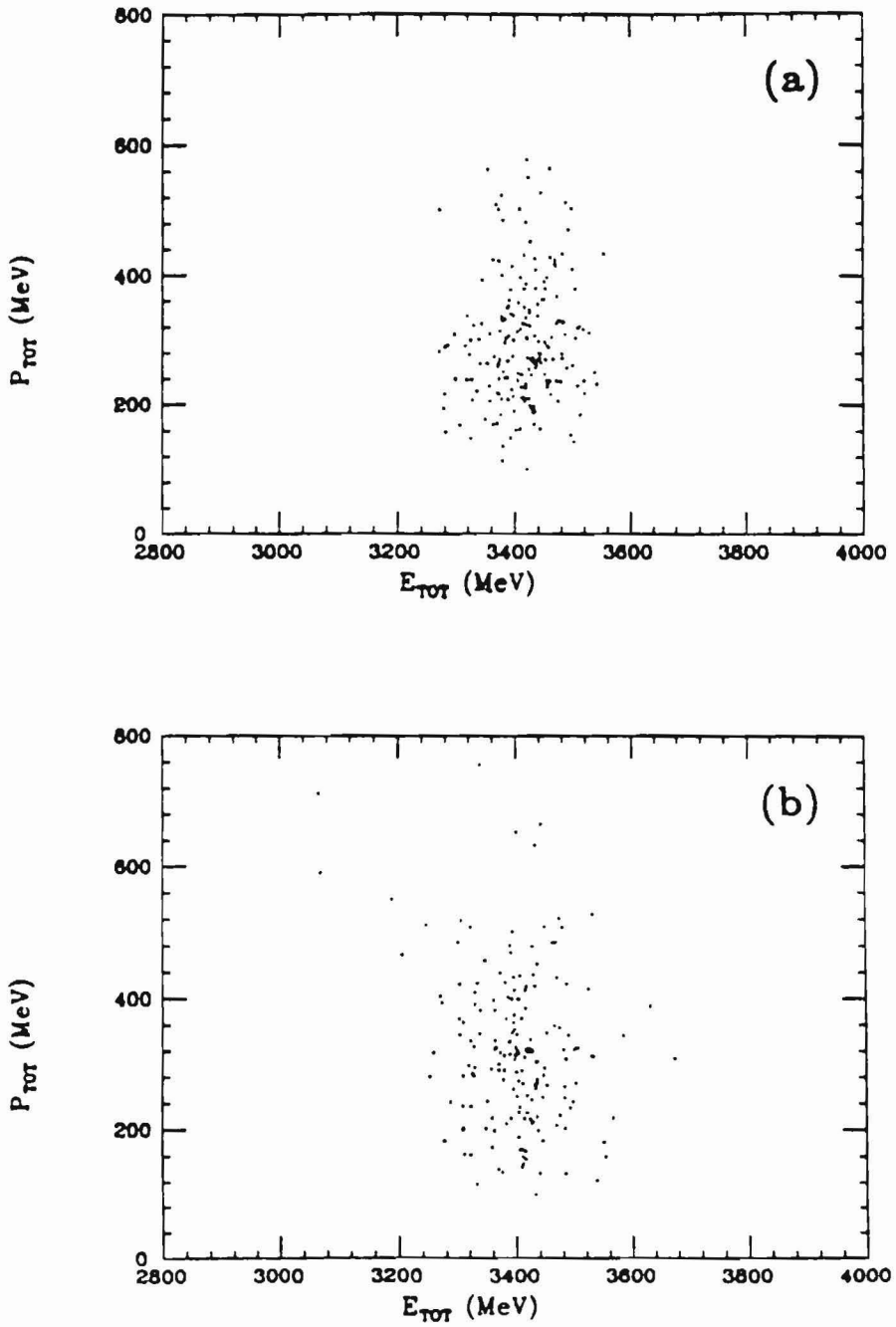

Figure 21: Scatterplot of P_{tot} versus E_{tot} for $\chi_0 \to \pi^0\pi^0$ decays.

(a) Monte Carlo events; (b) $\psi' \to \gamma\pi^0\pi^0$ events.

a scatterplot of P_{tot} versus E_{tot} for all events with a confidence level greater than 0.05. An obvious cluster of events is seen for E_{tot}≈3400 MeV, P_{tot}≈300 MeV, which is close to the values expected for χ_0 events. A similar cluster of events is seen in figure 21(a), which shows the same scatterplot for events from a Monte Carlo simulation of $\psi' \to \chi_0$, $\chi_0 \to \pi^0\pi^0$ decays. Figure 22 shows the P_{tot} distribution for events with $3100 < E_{tot}(MeV) < 3700$. The Monte Carlo and observed distributions are in reasonably good agreement, with both distributions showing a skew towards higher momenta. This skew is understood and occurs when the width of the P_{tot} distribution becomes comparable to the expected P_{tot}. Figure 23 shows the E_{tot} distribution for events with $P_{tot} < 600$ MeV. Both the Monte Carlo and the data show clear peaks for E_{tot}≈3400 MeV. The solid curves in figure 23 show the results of fitting a Gaussian line shape with a uniform background to the E_{tot} distributions. The magnitude of the background as well as the mean and magnitude of the Gaussian were allowed to vary in each fit. By allowing the width of the Gaussian to vary in the fit to the Monte Carlo E_{tot} distribution, the resolution on E_{tot} was determined to be 58 MeV. The observed E_{tot} distribution was then fit with the width of the Gaussian fixed at 58 MeV, giving a mean value for E_{tot} of 3403±5 MeV, which is within 0.5% of the expected value. Furthermore, the number of events in the signal is consistent with an estimate based upon previous measurements of the $\chi_0 \to \pi\pi$ branching ratio.[65]

The above analysis demonstrates that the analysis technique described above successfully finds $\chi_0 \to \pi^0\pi^0$ decays. Distributions of the confidence level and P_{tot} are in agreement with Monte Carlo predictions,

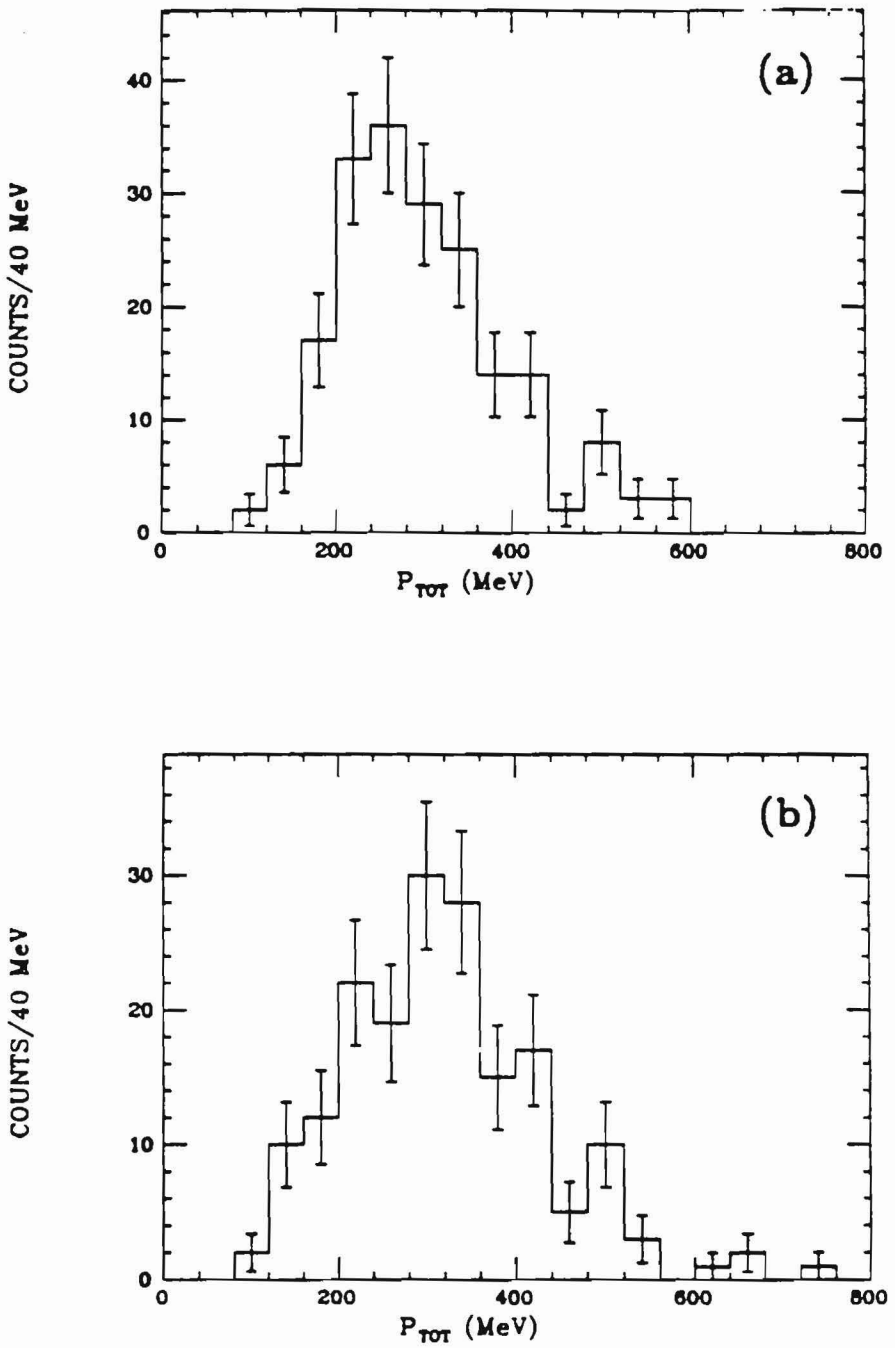

Figure 22: P_{tot} distribution for $\chi_0 \to \pi^0\pi^0$ decays.

(a) Monte Carlo events; (b) $\psi' \to \gamma\pi^0\pi^0$ events.

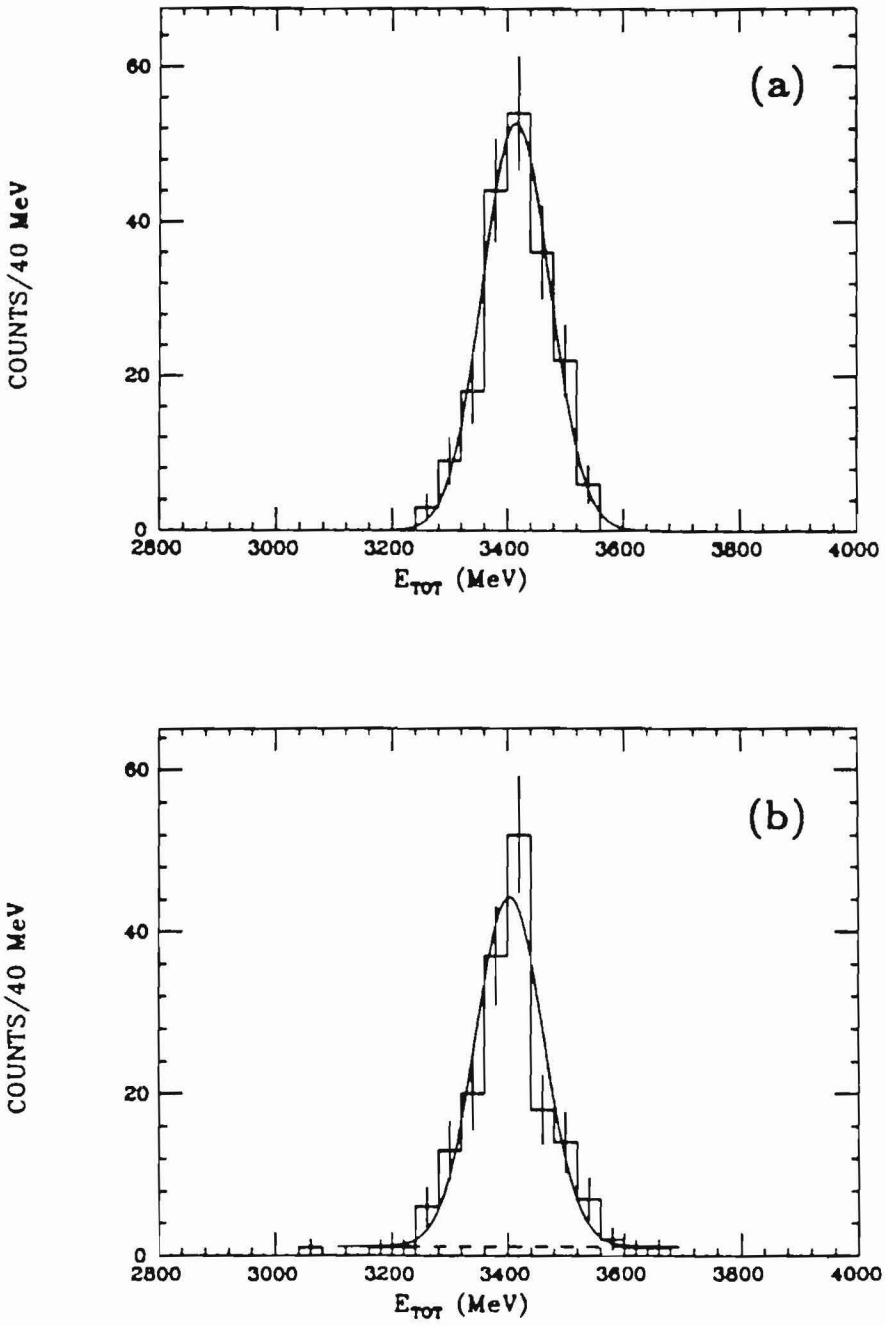

Figure 23: E_{tot} distribution for $\chi_0 \to \pi^0\pi^0$ decays.

(a) Monte Carlo events; (b) $\psi' \to \gamma\pi^0\pi^0$ events. The solid curve shows the result of a fit to the distribution, while the dashed line shows the background contribution.

and the E_{tot} distribution shows a narrow peak at the expected energy. This analysis also demonstrates that the energy scale for PIFIT tracks is accurate to ≈0.5% for E_π≈1700 MeV (the energy scale for photons is set by the Bhabha calibration). From these facts, it is reasonable to conclude that this analysis technique should be able to find decays of the D^0 into $\pi^0\pi^0$ and other similar final states if the branching ratios are large enough to produce measurable signals.

6.4.4 A search for the $\pi^0\pi^0$ final state

This section applies the above analysis technique to the ψ'' data sample in a search for the Cabibbo-suppressed decay $D^0\rightarrow\pi^0\pi^0$. The signature for a $D^0\rightarrow\pi^0\pi^0$ decay is very clean: a pair of energetic π^0s that are nearly back-to-back with a total energy near the beam energy and a total momentum of ≈290 MeV. To search for these decays, hadronic events from the ψ'' data sample were analyzed using the technique described above to calculate the total energy (E_{tot}), total momentum (P_{tot}), and the confidence level for each combination of two π^0s in the event. A Monte Carlo simulation of these decays was analyzed in an identical manner to serve as a guide to what $D^0\rightarrow\pi^0\pi^0$ decays should look like. The Monte Carlo events were also used to calculate the resolution on E_{tot} and the efficiency for reconstructing $D^0\rightarrow\pi^0\pi^0$ decays.

Figure 24 shows a scatterplot of P_{tot} versus E_{tot} for $\pi^0\pi^0$ combinations with a confidence level greater than 0.05. Observation of the decay $D^0\rightarrow\pi^0\pi^0$ would be indicated by a cluster of events with E_{tot}≈1886 MeV, P_{tot}≈287 MeV. No such clustering was observed anywhere in the vicinity of E_{tot}=1886 MeV, P_{tot}=287 MeV (see figure 24(b)).

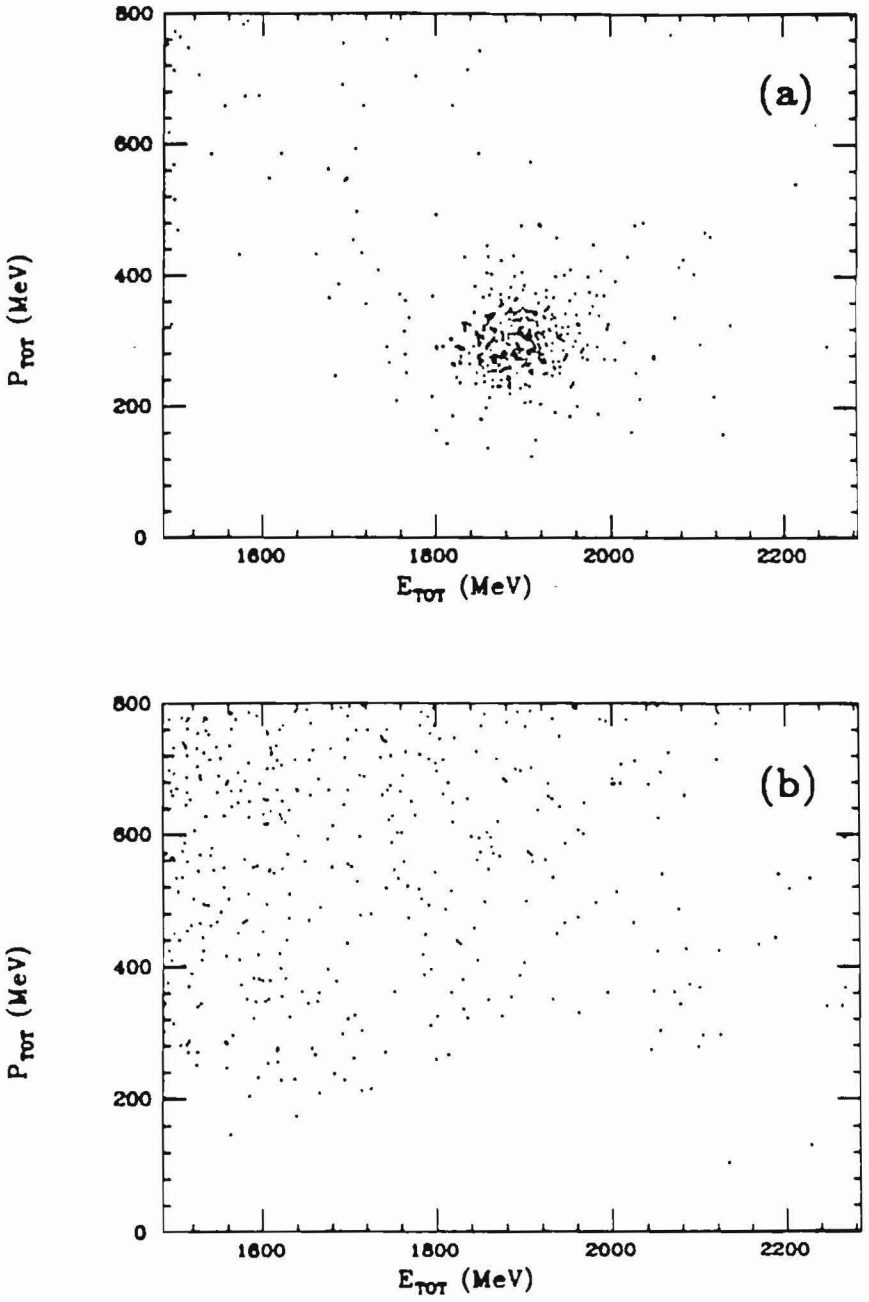

Figure 24: P_{tot} versus E_{tot} for $\pi^0\pi^0$ combinations.

(a) Monte Carlo events; (b) "ψ" events.

6.4.5 Cross checks

The absence of a signal in figure 24(b) indicates that either the branching ratio for $D^0 \to \pi^0\pi^0$ is below the sensitivity of this experiment or there is some reason why these decays failed to appear as expected on the basis of the Monte Carlo simulation shown in figure 24(a). The latter possibility was checked by constructing and testing several hypotheses that could account for a failure to observe a $D^0 \to \pi^0\pi^0$ signal. The following list describes the hypotheses that were considered and the reasons why they could be ruled out.

(1) Hypothesis: the Monte Carlo simulation is incorrect, and the analysis technique should not be expected to show the clustering exhibited by the Monte Carlo.

This hypothesis is extremely unlikely, since the same type of Monte Carlo simulation has been used successfully to model a wide variety of final states in the Crystal Ball detector. The good agreement between the Monte Carlo and the data for various distributions in the decay $\chi_0 \to \pi^0\pi^0$ is typical (see figures 20-23).

(2) Hypothesis: the detector was malfunctioning during the time the ψ'' data were taken.

To test this hypothesis, several checks were made on the detector operation. They included checking the mass and width of the π^0 and η mesons, the energy resolution for Bhabha events, and the collinearity of Bhabha events. All of these checks indicate that the detector performance was at least as good as for other running periods. Furthermore, data taken before and after the ψ'' data have been successfully analyzed without major problems.

(3) Hypothesis: there exist detector biases which are not correctly modeled by the Monte Carlo.

If this were the case, the $\chi^0 \to \pi^0\pi^0$ distributions would not be in such good agreement with the Monte Carlo. Also, Bhabha events were studied in detail to look for bias in the measurement of angles for back-to-back tracks. No such bias was found.

(4) Hypothesis: there is an error in the energy scale of the detector such that the signal appears in the wrong place.

It is well known within the Crystal Ball collaboration that the observed masses of the π^0 and η mesons are $\simeq$1% lower than their established values. This effect may be caused by small non-linearities in the response of the NaI crystals, photomultiplier tubes, or the associated electronics. This effect has also been observed in the ψ'' data sample, and it is estimated that the error in E_{tot} due to non-linearities is in the range of -1.5% to +0.5%. This effect would simply move the position of the cluster slightly, and cannot explain the absence of a signal in figure 24(b).

(5) Hypothesis: there was an error in the data analysis program.

This hypothesis can be ruled out because obvious signals are observed in the $D^0 \to \pi^0\pi^0$ Monte Carlo and the $\chi_0 \to \pi^0\pi^0$ analysis, both of which use the same analysis program.

On the basis of these cross checks, it was concluded that the branching ratio for $D^0 \to \pi^0\pi^0$ is below the sensitivity of this experiment.

6.4.6 The reconstruction efficiency for $D^0 \to \pi^0\pi^0$ decays

This section describes the method used to determine the efficiency for reconstructing $D^0 \to \pi^0\pi^0$ decays. Before the efficiency can be calculated, it must first be decided when an event is to be counted as a D^0 decay candidate. It was decided that the best way to count D^0 decays was to first make cuts on the confidence level and P_{tot} to help reduce background combinations, and then use the E_{tot} distribution to determine if there is an excess of events near E_{tot}=1886 MeV. Using the E_{tot} distribution to count D^0 decays has the advantage that E_{tot} is a simple sum of four photon energies, and accurately measuring photon energies is what the Crystal Ball does best.

Since no signal is observed in the data, it is necessary to rely on the Monte Carlo simulation to determine where cuts should be made. The background due to combinations with misidentified π^0 mesons was reduced by eliminating combinations with a low confidence level. Figure 25(a) shows the confidence level distributions for $\pi^0\pi^0$ combinations with $200 < P_{tot}(MeV) < 400$ and $1686 < E_{tot}(MeV) < 2046$. Since the confidence level distribution for Monte Carlo events is nearly flat for confidence levels greater than 0.05, it was decided to eliminate only those combinations with a confidence level less than 0.05. Note that a flat confidence level distribution suggests that the correct errors were used in the π^0 reconstruction. Since P_{tot} is required to be 287 MeV for D^0 decays, a cut can be made on P_{tot} to accept only those combinations which have a value of P_{tot} near 287 MeV. Figure 26(a) shows the Monte Carlo P_{tot} distribution for combinations with a confidence level greater than 0.05 and $1686 < E_{tot}(MeV) < 2046$. As expected, this distribution shows a clear

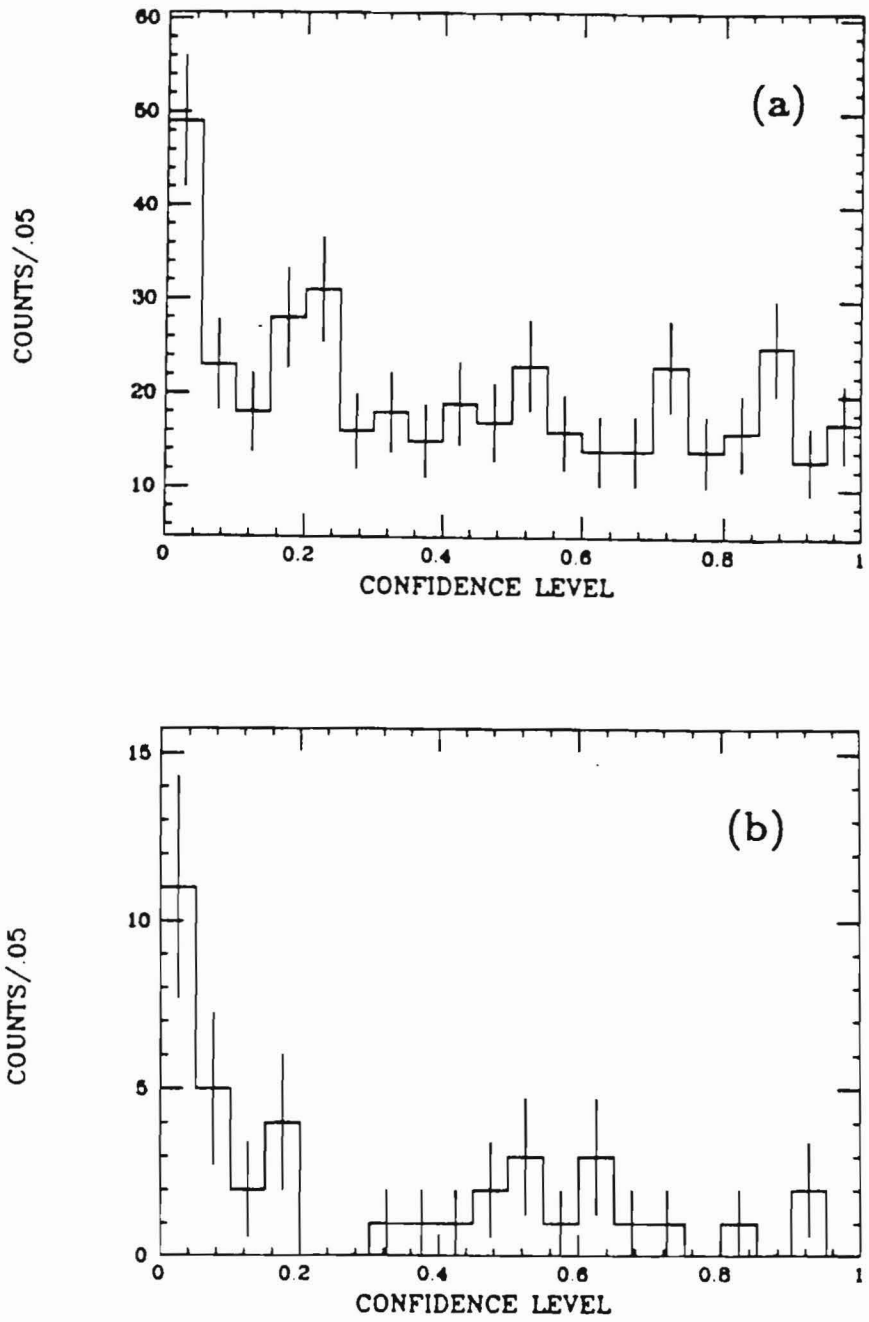

Figure 25: Confidence level distribution for $\pi^0\pi^0$ combinations.

(a) Monte Carlo events; (b) ψ'' events.

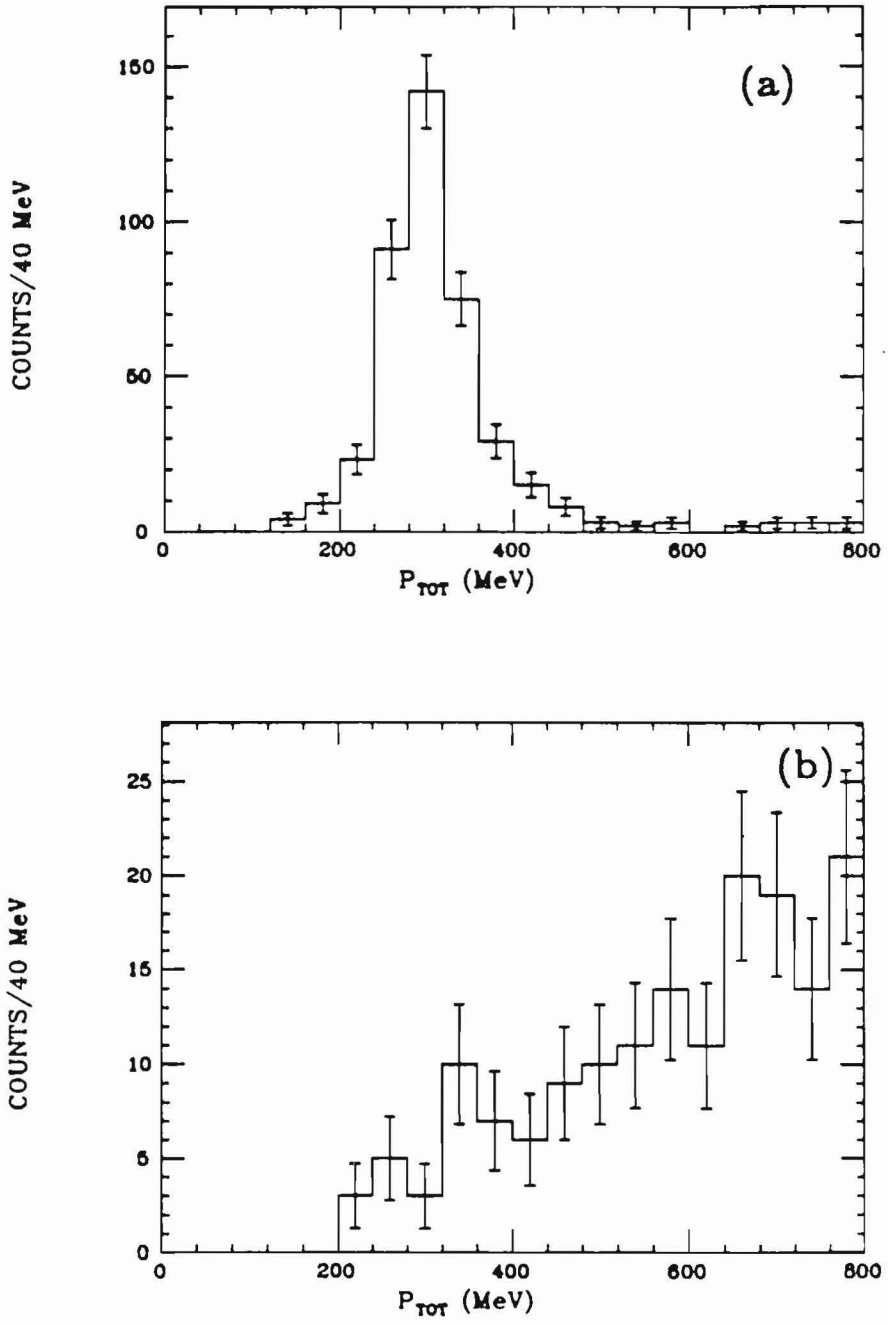

Figure 26: P_{tot} distribution for $\pi^0\pi^0$ combinations.

(a) Monte Carlo events; (b) ψ'' events.

peak at P_{tot}≅290 MeV. On the basis of figure 26(a), combinations were eliminated if they did not have 200<P_{tot}(MeV)<400.

Figure 27(a) shows the Monte Carlo E_{tot} distribution after making the above cuts. This distribution shows a narrow peak at the beam energy. To determine the efficiency for reconstructing $D^0 \to \pi^0\pi^0$ decays, a Gaussian line shape and a linear background term were fit to the peak in figure 27(a). The amplitude, mean, and width of the Gaussian, as well as the background parameters, were allowed to vary in the fit. The following results were obtained from the fit: the mean E_{tot} is 1893±2 MeV, the width of the E_{tot} distribution is 38±2 MeV, and the efficiency for reconstructing $D^0 \to \pi^0\pi^0$ is 0.324±0.020, where the errors are the statistical errors from the fit. These results show that the mean E_{tot} comes out approximately correct, the width of the E_{tot} distribution is in agreement with expectations based on the detector energy resolution, and there is a reasonably good efficiency for reconstructing $D^0 \to \pi^0\pi^0$ decays.

An important source of systematic error in the reconstruction efficiency is due to a lack of knowledge about how the other D^0 in the event decays. This second D^0 introduces an inefficiency when tracks from the second D^0 overlap with one or more of the photons from the $\pi^0\pi^0$ final state, causing the event to be incorrectly reconstructed. To estimate the magnitude of this inefficiency, Monte Carlo events were generated containing a single D^0 which was decayed to a $\pi^0\pi^0$ final state. The above analysis was repeated for these events, and an efficiency of 0.610±0.025 was obtained. Thus, nearly half of the D^0 mesons which could be reconstructed are lost due to overlap with tracks from the sec-

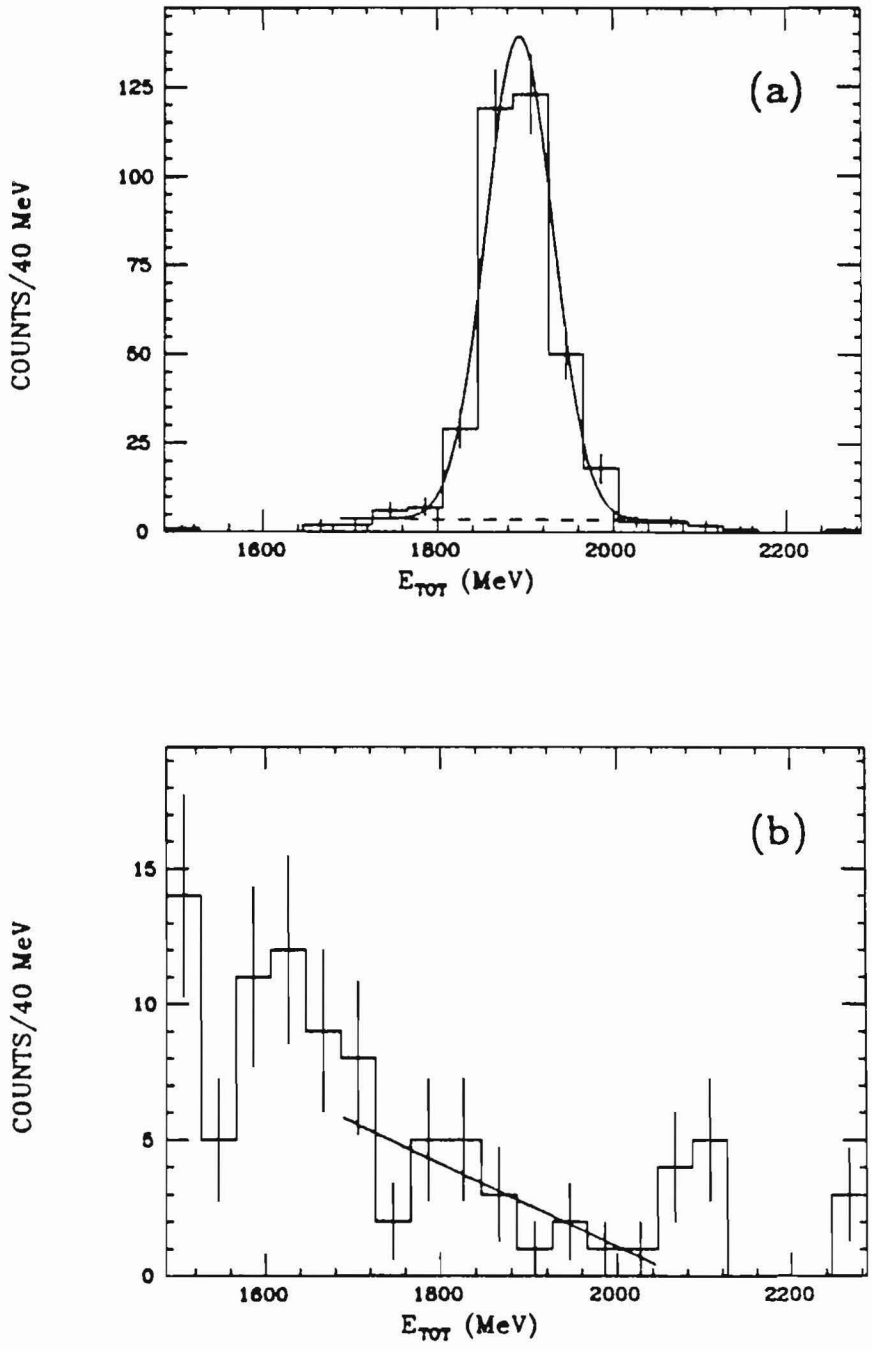

Figure 27: E_{tot} distribution for $\pi^0\pi^0$ combinations.

(a) Monte Carlo events; (b) ψ'' events. The curves show the results of fitting a Gaussian line shape and a linear background term to the distributions.

ond D meson. This comparison suggests that the Monte Carlo efficiencies are strongly dependent on the model used for generating decays of the second D^0 meson (see appendix B). The systematic uncertainty in the efficiency due to the model was estimated to be 30% of the efficiency for four-photon final states and 45% of the efficiency for six-photon final states. Including the systematic error gives an efficiency for reconstructing $D^0 \rightarrow \pi^0\pi^0$ events of 0.32 ± 0.10.

6.4.7 Determination of an upper limit on the branching ratio for $D^0 \rightarrow \pi^0\pi^0$

This section describes the procedure used to set an upper limit on the branching ratio for $D^0 \rightarrow \pi^0\pi^0$. Figures 25(b)-27(b) show the observed distributions for the confidence level, P_{tot}, and E_{tot} using the same cuts as were used for the Monte Carlo distributions above. As expected from the lack of clustering in the scatterplot of P_{tot} versus E_{tot} (figure 24(b)), no significant signals are seen in either the P_{tot} or the E_{tot} distributions. The solid curve in figure 27(b) shows the results of fitting a Gaussian line shape and a linear background term to the data. A binned likelihood fit using Poisson statistics was used because of the small number of events in most bins. The amplitude of the Gaussian and the background parameters were allowed to vary freely, though a penalty function was used to keep the background level positive in each bin. The mean of the Gaussian was allowed to vary from 1857 MeV to 1894 MeV, reflecting the uncertainty in the energy scale for E_{tot} (see section 6.4.5); the width was fixed at the resolution determined by the Monte Carlo, 38 MeV. Maximizing the likelihood gave the solid line in figure 27(b).

To determine an upper limit on the number of $D^0 \to \pi^0\pi^0$ decays in the data, the above fit was done with the amplitude of the Gaussian fixed at various values, giving the maximum likelihood as a function of the expected number of $D^0 \to \pi^0\pi^0$ events in figure 27(b). This maximum likelihood was integrated over the expected number of events, and the point where the integral reaches 90% of its total area is taken to be the 90% confidence level upper limit on the expected number of signal events. The result of this analysis is that a signal of 8 events in figure 27(b) is ruled out at the 90% confidence level. To obtain an upper limit on the product of the D^0 cross section and the branching ratio for the $D^0 \to \pi^0\pi^0$ decay mode, $\sigma_{D^0} \cdot BR(D^0 \to \pi^0\pi^0)$, the efficiency was folded into the likelihood function, giving a 90% confidence level upper limit of 0.019 nb. The D^0 cross section was previously measured to be $\sigma_{D^0} = 6.8 \pm 1.2$ nb (see section 4.5); dividing out σ_{D^0} gives an upper limit on the branching ratio: $BR(D^0 \to \pi^0\pi^0) < 0.2\%$ at the 90% confidence level.

6.4.8 A search for the $\eta\pi^0$, $\eta\eta$, $\pi^0\pi^0\pi^0$ and $\eta\pi^0\pi^0$ final states

This section describes the results of a search for D^0 decays into $\eta\pi^0$, $\eta\eta$, $\pi^0\pi^0\pi^0$, and $\eta\pi^0\pi^0$ final states. The analysis of these final states is almost identical to the analysis used for the $\pi^0\pi^0$ final state, so only the differences will be noted. Combinations with a confidence level less than 0.05 were eliminated, and scatterplots of P_{tot} versus E_{tot} were made for each decay mode (see figures 28, 30, 32, and 34). No obvious clustering in the vicinity of $P_{tot} = 290$ MeV, $E_{tot} = 1886$ MeV is observed in any of these scatterplots. To measure the efficiency and set upper limits on the branching ratios for these modes, a cut was

made to eliminate combinations with P_{tot} outside the range 200-400 MeV (except for the $\pi^0\pi^0\pi^0$ final state, where the range was extended to 440 MeV on the basis of the Monte Carlo distribution). The resulting E_{tot} distributions are shown in figures 29, 31, 33, and 35. The Monte Carlo distributions were fit to determine the reconstruction efficiency for each final state. Upper limits on the number of expected events, $\sigma_{D^0} \cdot BR$, and the branching ratio for the final state were set using the method described in section 6.4.8. The results of these measurements are summarized in table 5.

TABLE 5

Results of the Search for Neutral Decay Modes of the D^0

DECAY MODE	EFFICIENCY	EVENTS (90% CL)	$\sigma_{D^0} \cdot BR$ (90% CL)	BRANCHING RATIO (90% CL)
$D^0 \to \pi^0\pi^0$	0.32±0.10	<8	<0.019 nb	<0.28%
$D^0 \to \eta\pi^0$	0.11±0.03	<7	<0.05 nb	<0.74%
$D^0 \to \eta\eta$	0.04±0.01	<4	<0.07 nb	<1.0 %
$D^0 \to \pi^0\pi^0\pi^0$	0.16±0.08	<20	<0.11 nb	<1.6 %
$D^0 \to \eta\pi^0\pi^0$	0.06±0.03	<26	<0.45 nb	<6.6 %
$D^0 \to \bar{K}^0\pi^0$	0.02±0.01	<11	<0.52 nb	<7.6 %

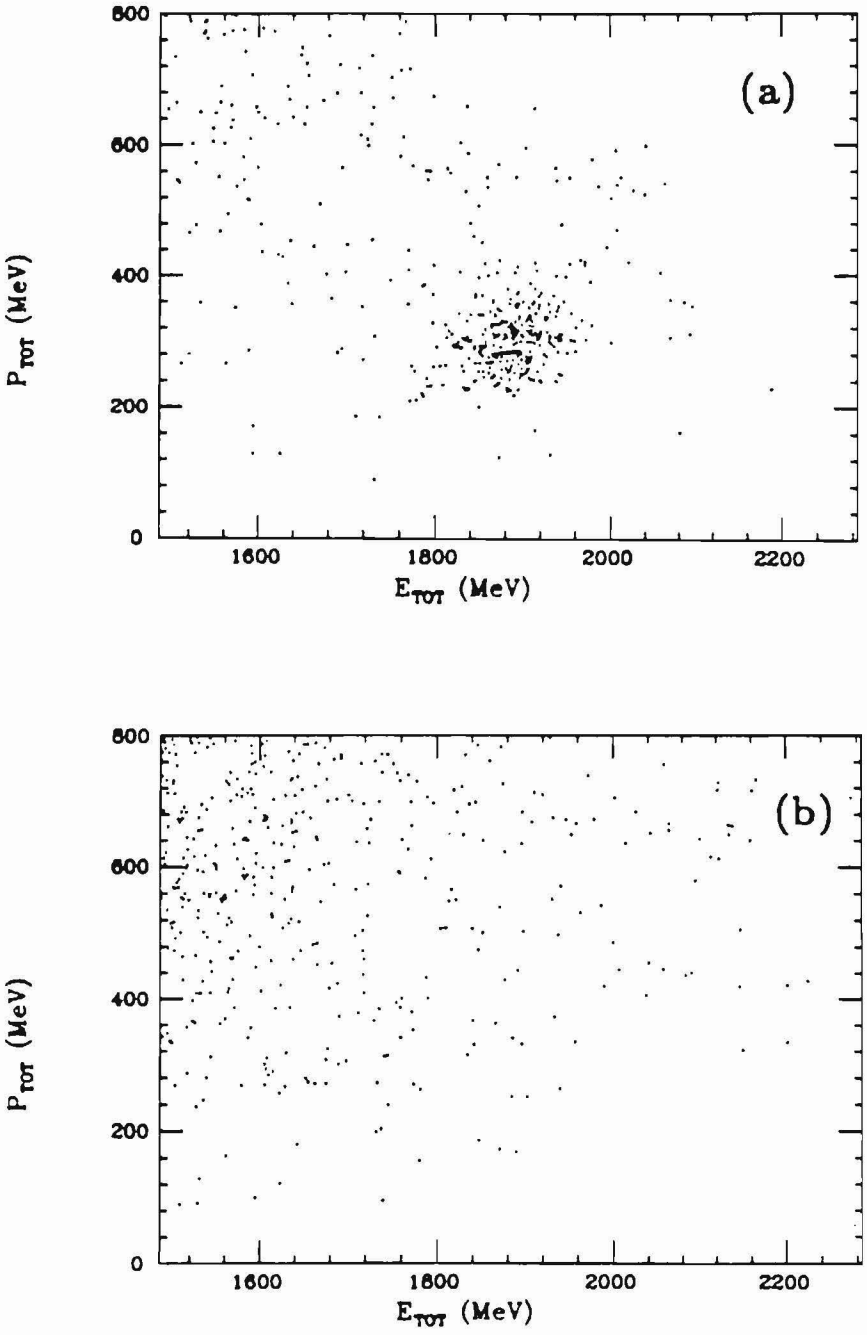

Figure 28: P_{tot} versus E_{tot} for $\eta\pi^0$ combinations.

(a) Monte Carlo events; (b) ψ'' events.

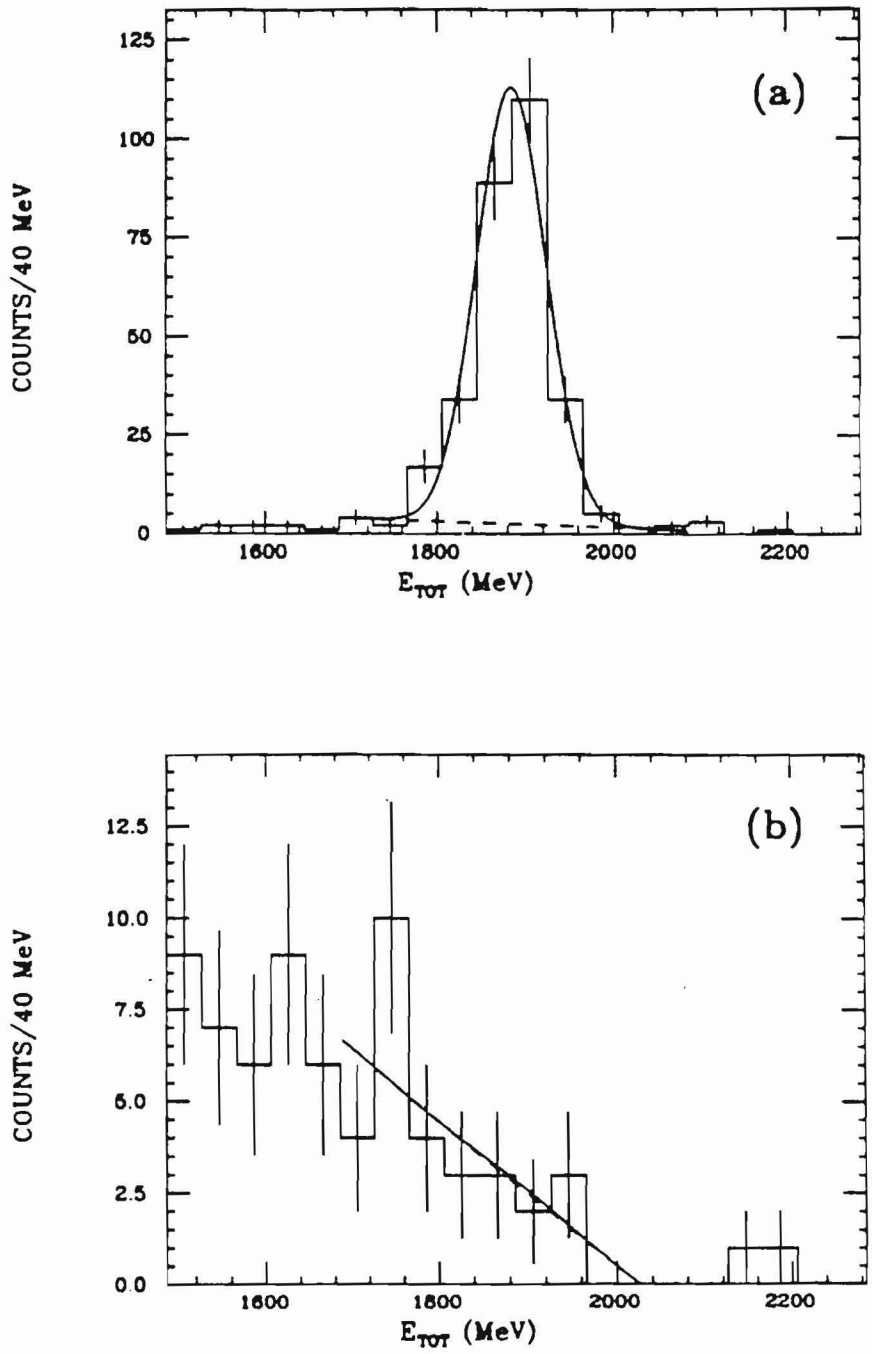

Figure 29: E_{tot} distribution for $\eta\pi^0$ combinations.

(a) Monte Carlo events; (b) ψ'' events. The curves show the results of fitting a Gaussian line shape and a linear background term to the distributions.

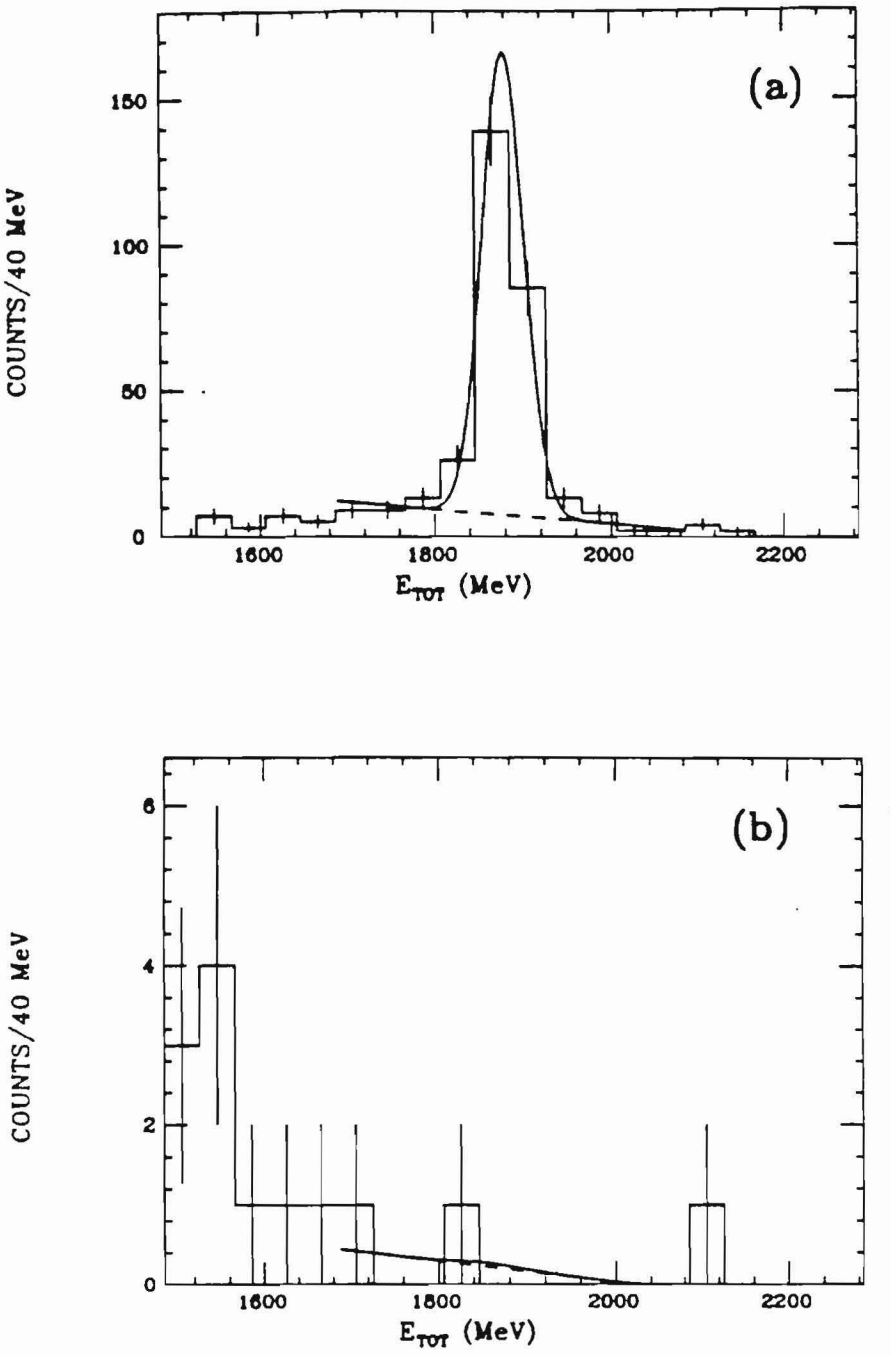

Figure 31: E_{tot} distribution for $\pi\pi$ combinations.

(a) Monte Carlo events; (b) ψ'' events. The curves show the results of fitting a Gaussian line shape and a linear background term to the distributions.

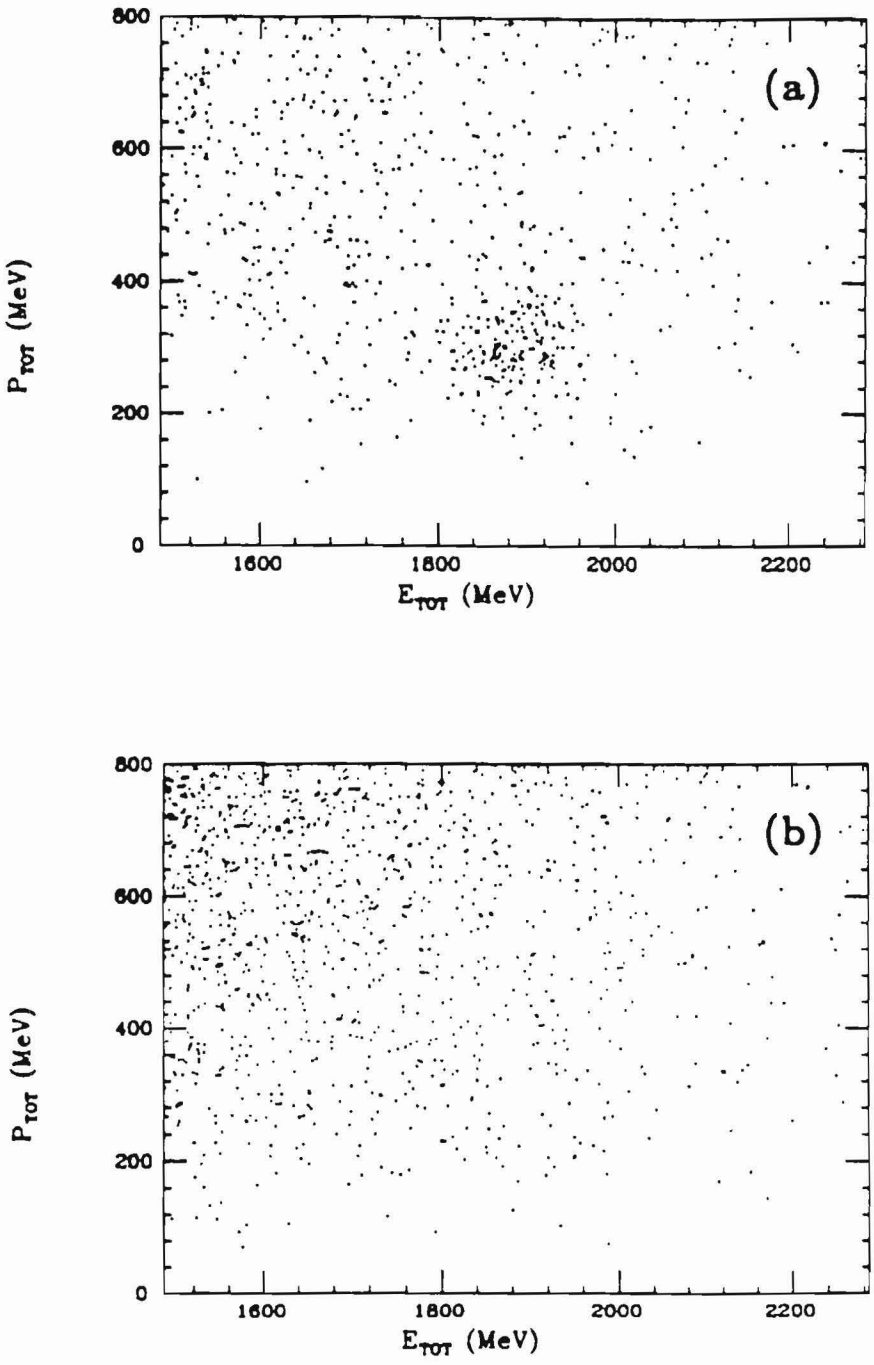

Figure 32: P_{tot} versus E_{tot} for $\pi^0\pi^0\pi^0$ combinations.

(a) Monte Carlo events; (b) ψ'' events.

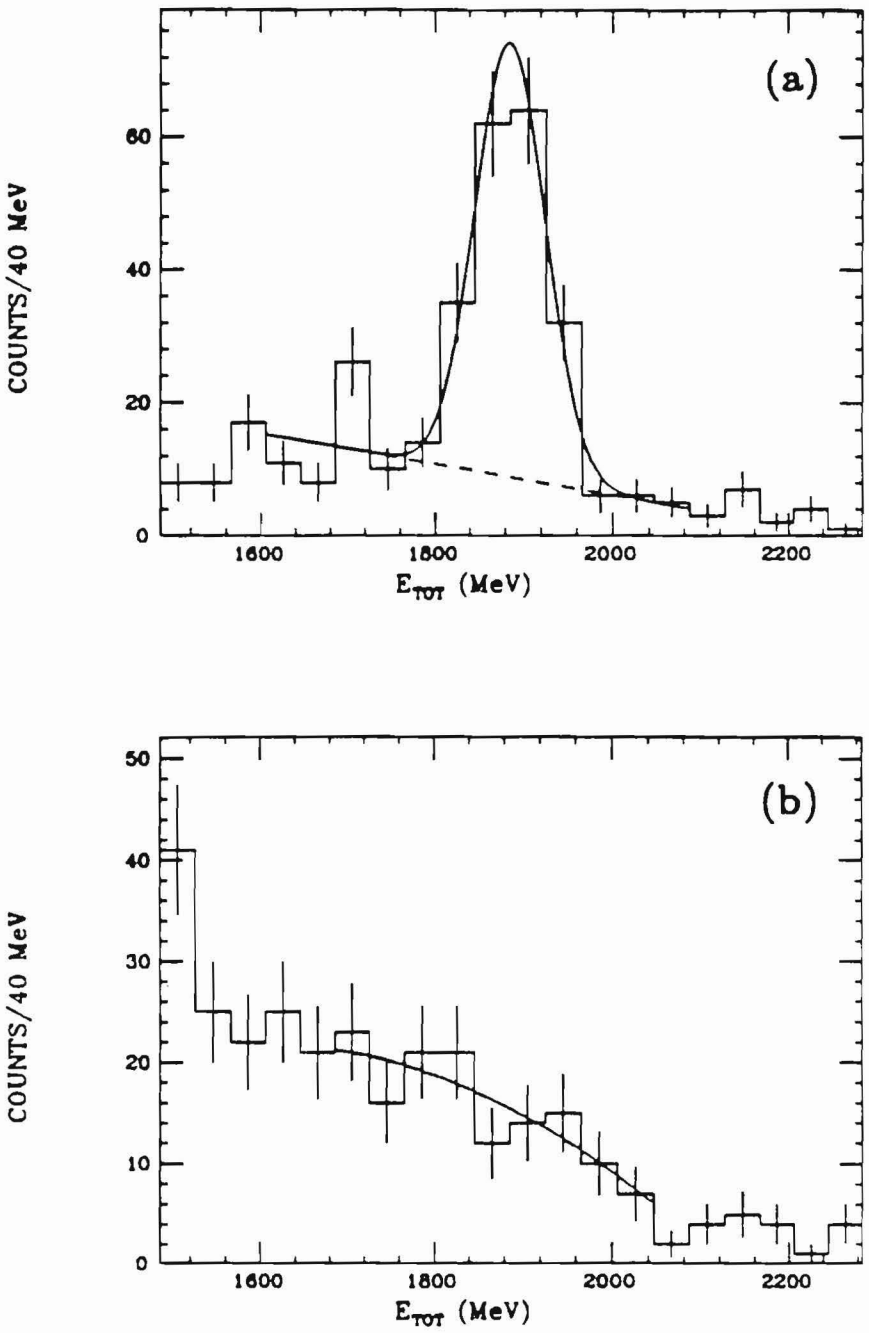

Figure 33: E_{tot} distribution for $\pi^0\pi^0\pi^0$ combinations.

(a) Monte Carlo events; (b) ψ'' events. The curves show the results of fitting a Gaussian line shape and a quadratic background term to the distributions.

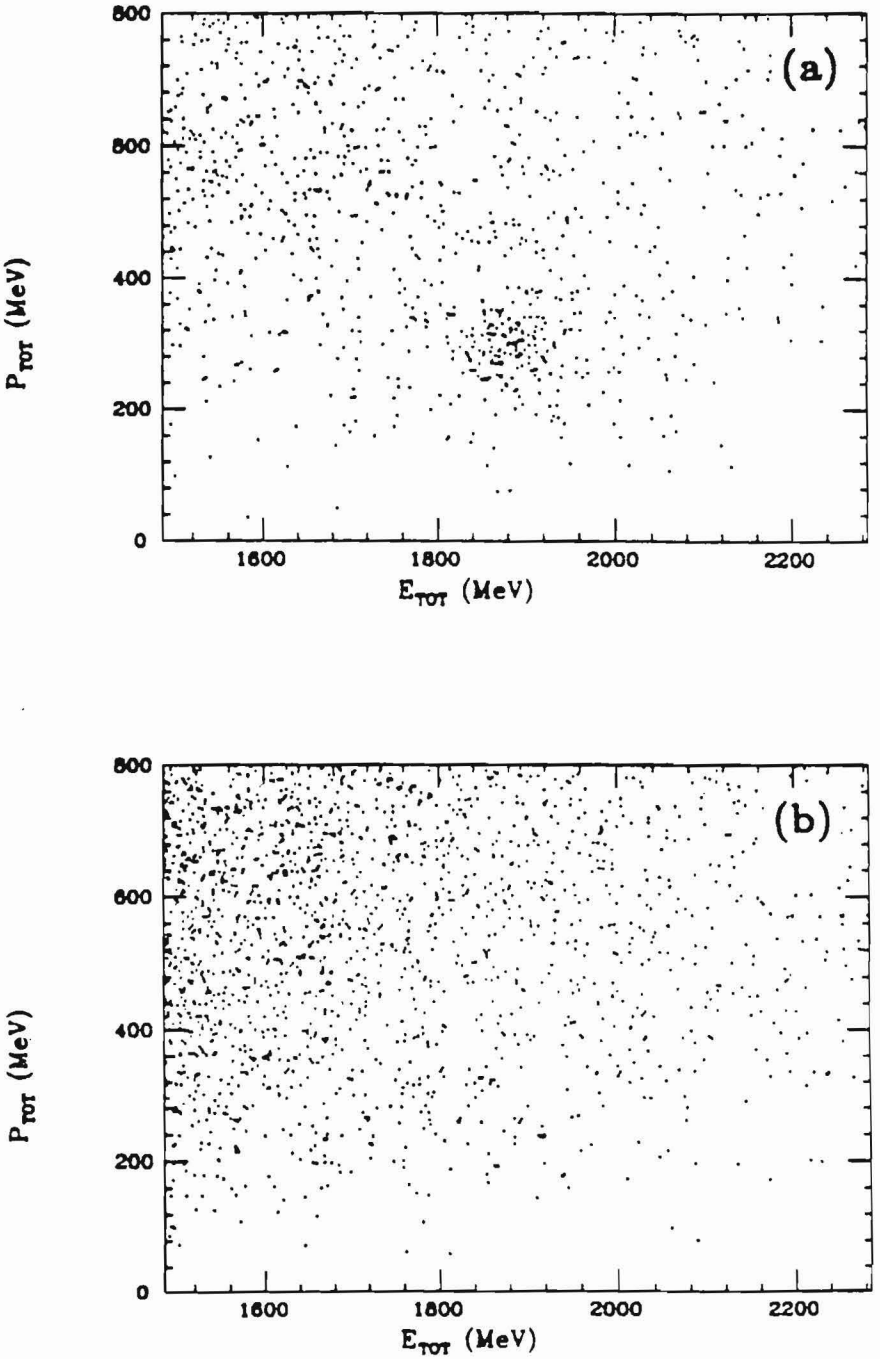

Figure 34: P_{tot} versus E_{tot} for $\pi\pi^0\pi^0$ combinations.

(a) Monte Carlo events; (b) ψ'' events.

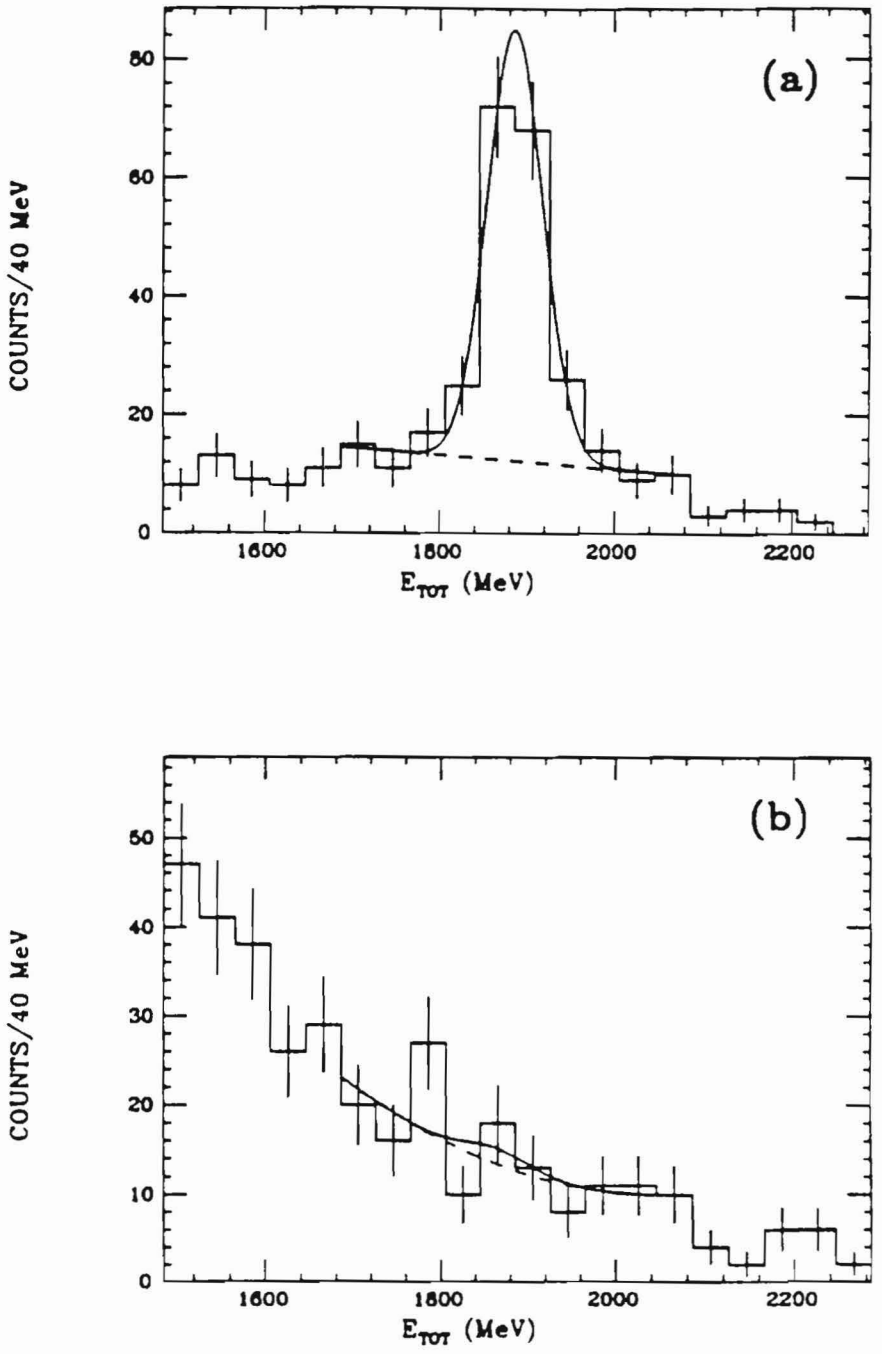

Figure 35: E_{tot} distribution for $\pi\pi^0\pi^0$ combinations.

(a) Monte Carlo events; (b) ψ'' events. The curves show the results of fitting a Gaussian line shape and a quadratic background term to the distributions.

6.4.9 A search for the $K_S\pi^0$ final state

This section describes a search that was made for the $K_S\pi^0$ decay mode of the D^0, where the K_S decays to $\pi^0\pi^0$. The only major difference between this final state and the $\pi^0\pi^0\pi^0$ final state is an additional requirement that one of the $\pi^0\pi^0$ pairs must be consistent with the K^0 mass. To demonstrate that the Crystal Ball can reconstruct the decay $K_S\rightarrow\pi^0\pi^0$, $K_S\pi^0$ Monte Carlo events were searched for $\pi^0\pi^0\pi^0$ combinations with a confidence level greater than 0.05, P_{tot} in the range 200-440 MeV, and E_{tot} in the range 1686-2086 MeV. Figure 36(a) shows the $\pi^0\pi^0$ mass distribution for these combinations, where all three $\pi^0\pi^0$ mass pairings were included in the distribution. A clear peak is seen near the K^0 mass. Combinations likely to have a $K_S\rightarrow\pi^0\pi^0$ decay were selected by requiring that the confidence level be greater than 0.05 and that at least one of the $\pi^0\pi^0$ combinations have a mass in the range 400-560 MeV. Figure 37 shows the scatterplot of P_{tot} versus E_{tot} for these combinations. A clear cluster at P_{tot}=290 MeV, E_{tot}=1886 MeV is observed for Monte Carlo generated events, but no significant clustering is observed in the data. Figure 38 shows the E_{tot} distribution after making the additional requirement that a combination must have P_{tot} in the range 200-440 MeV. No significant signal is observed in the data near E_{tot}=1886 MeV. An upper limit of 7.6% was obtained for the branching ratio $BR(D^0\rightarrow\bar{K}^0\pi^0)$ using the method described in section 6.4.7.

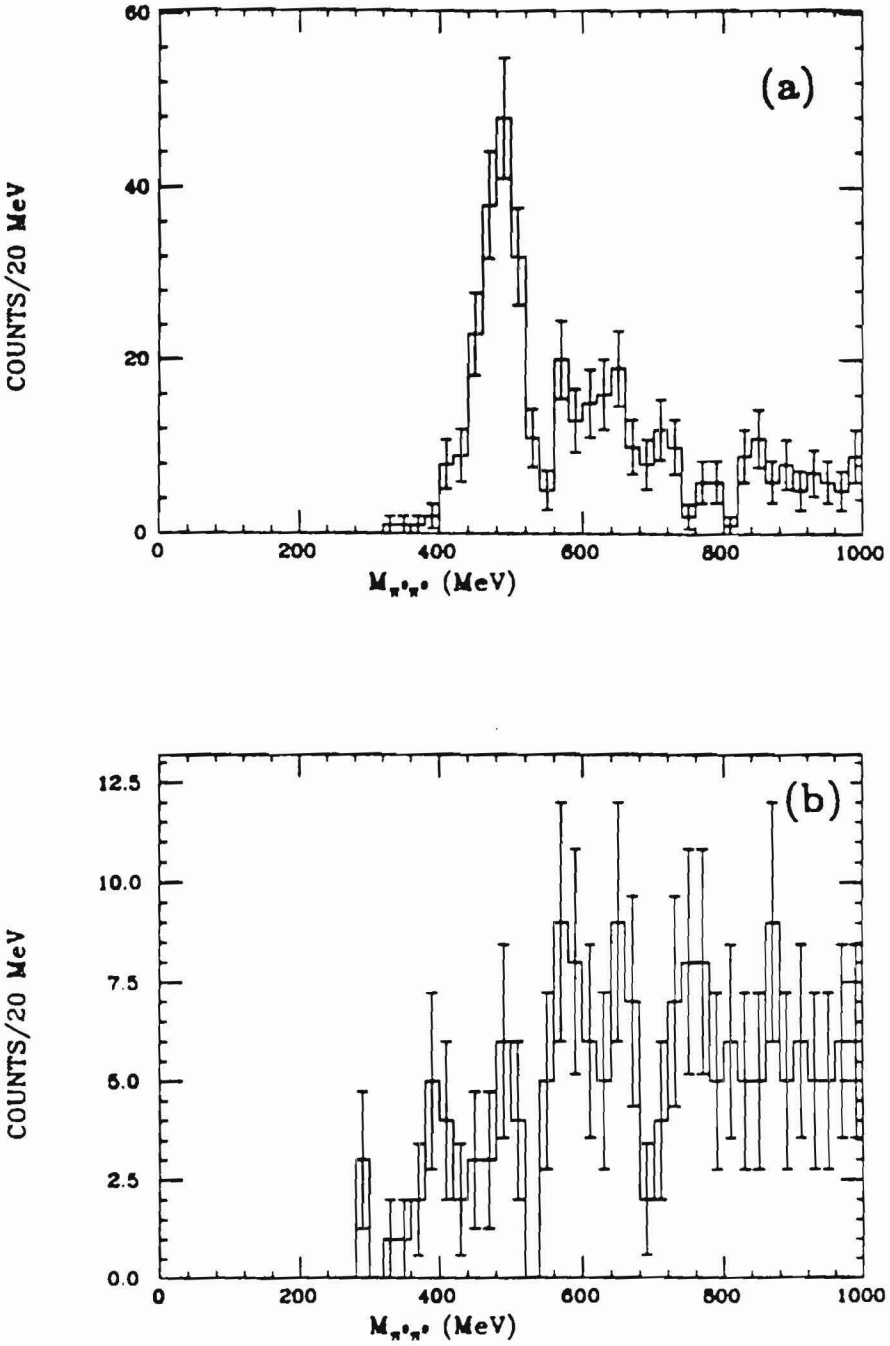

Figure 36: $M_{\pi^0\pi^0}$ distribution for $\pi^0\pi^0\pi^0$ combinations.

(a) Monte Carlo events; (b) ψ'' events.

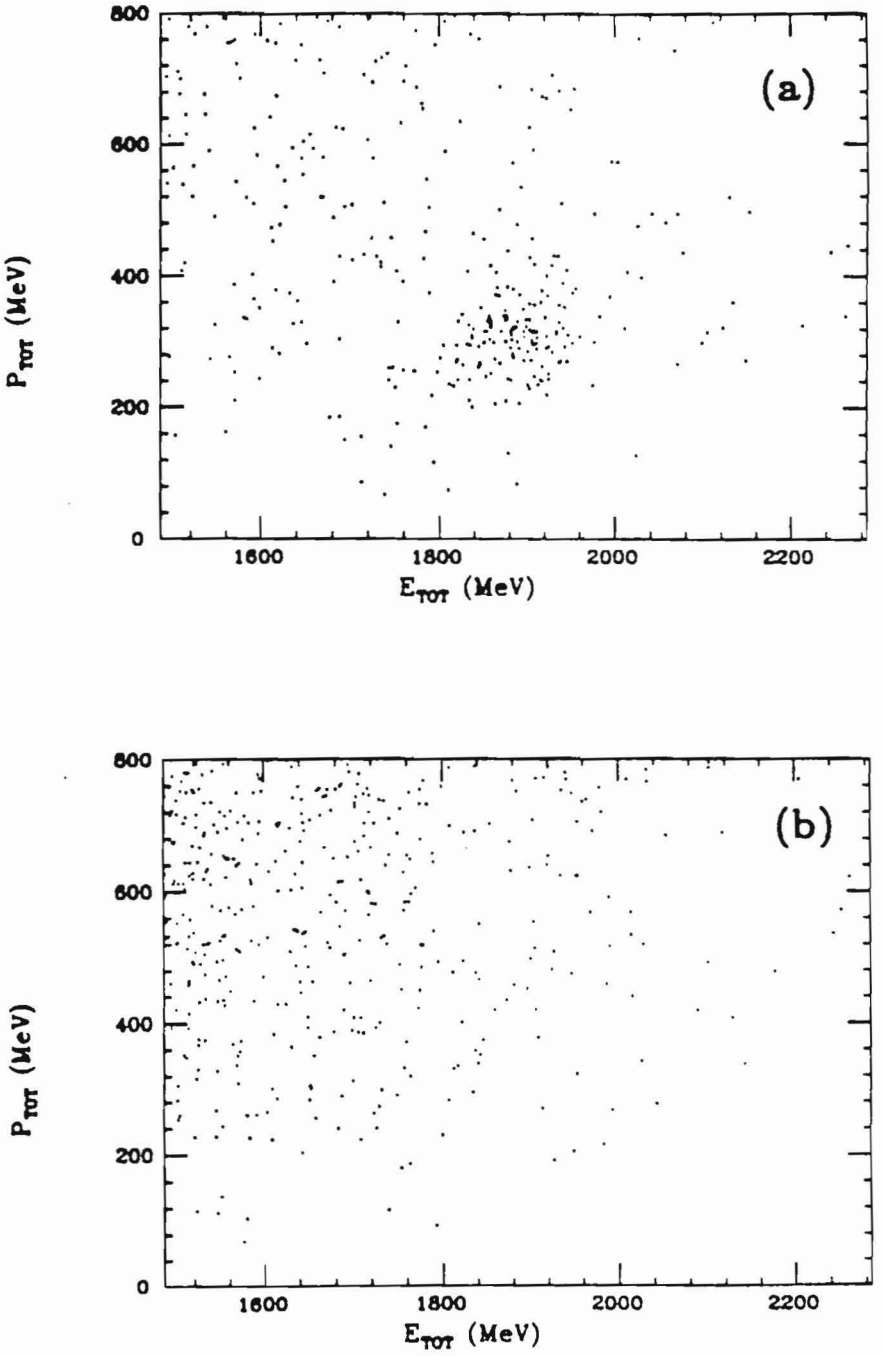

Figure 37: P_{tot} versus E_{tot} for $K_S\pi^0$ combinations.

(a) Monte Carlo events; (b) ψ'' events.

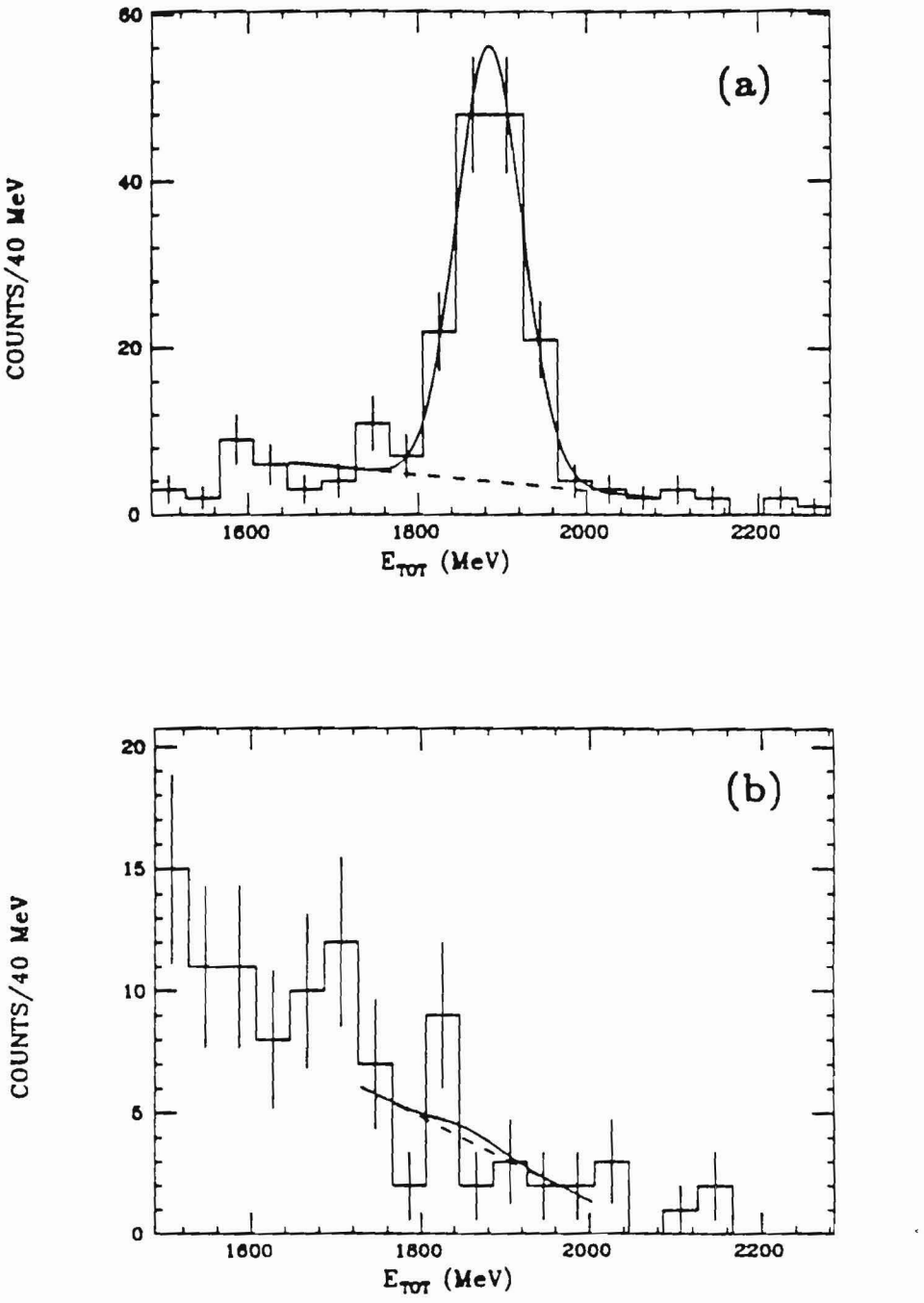

Figure 38: E_{tot} distribution for $K_S\pi^0$ combinations.

(a) Monte Carlo events; (b) ψ'' events. The curves show the results of fitting a Gaussian line shape and a linear background term to the distributions.

6.5 SUMMARY AND CONCLUSIONS

This chapter has described the results of a search for D^0 decays into four-photon and six-photon final states. No significant signals were observed in any of the channels investigated. The results of this search are summarized in table 5.

To help interpret the significance of these results, it is useful to compare the results with the predictions of the sextet dominance model.[56] Table 6 shows the limits set by this experiment relative to the rate for $D^0 \to K^-\pi^+$ determined by the Mark II experiment.[66] The relevant results of the Mark I and Mark II experiments[20,67] are also shown in table 6, as well as the predictions[68] of the sextet dominance model.

TABLE 6

Comparison of Rates for Several D^0 Decay Modes Relative to $K^-\pi^+$

Decay Mode	Sextet Dominance	Mark I	Mark II	Crystal Ball
$\bar{K}^0\pi^0$	0.500	<2.7	0.75±0.45	<2.2
K^+K^-	0.056	<0.07	0.113±0.030	-
$\pi^+\pi^-$	0.056	<0.07	0.033±0.015	-
$\pi^0\pi^0$	0.028	-	-	<0.08
$\eta\pi^0$	0.019	-	-	<0.21
$\eta\eta$	0.028	-	-	<0.29
$\pi^0\pi^0\pi^0$	-	-	-	<0.46
$\eta\pi^0\pi^0$	-	-	-	<1.9

Several conclusions can be reached from the data in table 6. The limits obtained for several S=0 final states (i.e., $\pi^0\pi^0$, $\pi^0\eta$, $\eta\eta$, and

$\pi^0\pi^0\pi^0$) support the hypothesis that these decay modes are suppressed relative to S=-1 final states such as $K^-\pi^+$. In particular, the decay $D^0\rightarrow\pi^0\pi^0$ is at least a factor of 12 less likely to occur than the decay $D^0\rightarrow K^-\pi^+$. The Mark I and Mark II experiments also observed a strong suppression of the S=0 final states they were sensitive to, such as K^+K^- and $\pi^+\pi^-$. In terms of the weak interaction couplings, these results imply that $|V_{cd}|^2 \ll |V_{cs}|^2$, as expected for the standard model.

Although the limits obtained by this experiment are consistent with the predictions of the sextet dominance model, they are not stringent enough to provide a rigorous test of the model. However, the Mark II measurements in table 6 show a puzzling feature: the rate for $D^0\rightarrow\pi^+\pi^-$ is considerably smaller than the rate for $D^0\rightarrow K^+K^-$. Note that the Crystal Ball limit on the $\pi^0\pi^0$ rate is also somewhat less than the K^+K^- rate. Models that assume SU(3) symmetry, including the sextet dominance model, predict equal K^+K^- and $\pi^+\pi^-$ rates. The observed discrepancy in decay rates suggests that these simple models are either wrong or in need of substantial modification; the limits obtained by this experiment may prove to be important constraints in solving this puzzle.

This experiment was begun with the hope of observing a small number of events in the Cabibbo-suppressed $\pi^0\pi^0$ final state. Unfortunately, the detection efficiency turned out to be substantially lower than was expected, primarily due to confusion caused by the other D^0 in the event. In addition, the background level proved to be somewhat higher than was anticipated for such a clean signature. These effects caused the experiment to be a factor of 2-3 less sensitive than was originally anticipated, which substantially reduced the significance of the measurements.

Appendix A

PIFIT: AN ALGORITHM FOR UNFOLDING TWO OVERLAPPING PHOTONS

If two photons strike the Crystal Ball in the same vicinity, their energy deposits will overlap and form a single connected region. When this happens, the less energetic photon is often missed completely by the BUMPS algorithm in the offline analysis program. Even if both photons are found by BUMPS, there are difficulties in accurately determining the energy and direction cosines of the two photons. This severely limits the ability of the offline analysis program to find π^0 decays when the π^0 has an energy greater than 700 MeV. The study of neutral decay modes of the D^0 requires the ability to detect π^0s in the energy range 700-1100 MeV with high efficiency. To achieve this, a new algorithm was developed that can identify connected regions in which two photons overlap and reconstruct the photons. This algorithm was incorporated into the subroutine PIFIT, and has proved to be very successful for π^0 energies up to 2 GeV. The purpose of this appendix is to describe in some detail the inner workings and capabilities of PIFIT.

In order to understand the PIFIT algorithm, it is instructive to first consider the problem of determining the direction cosines of a single photon in the detector. It will be seen later that reconstructing overlapping photon showers is just an extension of the techniques developed for a single photon. When a photon strikes the Crystal Ball, it usually deposits 50-80% of its energy in the crystal it enters, which

is referred to as the central crystal. Nearly all of the remaining energy is deposited in the 12 nearest neighbors of the central crystal.[27] The 13 energies in these crystals can be thought of as a pattern, and each way of distributing the photon energy among the 13 crystals will have a unique pattern associated with it.

Suppose a beam of fixed energy photons was aimed at the centroid of a particular crystal. This would generate a series of patterns, with each pattern exhibiting a fairly symmetrical distribution of energy around the central crystal. While there would be substantial fluctuations in the pattern from shower to shower, there would be an underlying tendency for the energies to be distributed in a symmetrical manner. By contrast, consider what would happen if the photons were directed at the corner of the crystal. Again there would be substantial fluctuations from shower to shower, but the patterns would no longer tend to be symmetrical about the central crystal. Instead, most of the energy would be deposited in the crystals nearest to the corner where the photon struck. This comparison shows that the pattern of energies contains significant information about the direction of the photon.

One way to utilize this information is to determine the probability of every pattern as a function of the energy and direction of the photon. Using this probability function, the energy and direction of any given photon can be accurately estimated by finding the energy and direction that has the highest probability for the observed pattern. The only problem is in determining the probability function, which is a function of 16 variables! This is, for all practical purposes, impossible; however, by making some simplifications and approximations, it is

possible to find a reasonable approximation for the probability function.

The major simplification that was made was to assume that the probability function can be factorized into the product of 13 separate probabilities, each of which is a function of the photon direction and the energy in a single crystal:

$$F(E_1, E_2, \ldots, E_{13}, E_\gamma, \theta_\gamma, \phi_\gamma) \approx \prod_i f_i(E_i, E_\gamma, \theta_\gamma, \phi_\gamma)$$

where F is the real probability function, f_i is the factorized probability function for crystal i, E_1-E_{13} are the crystal energies, E_γ is the photon energy, and θ_γ and ϕ_γ are the angles that determine the direction of the photon. The problem now is to determine the 13 factorized probability functions, each of which is a function of 4 variables. This is a much simpler problem because it ignores the correlations among the crystal energies. Only for special cases, such as Gaussian probability functions, is there a clear-cut way to factorize the problem and still keep the correlations. Although the accuracy of the PIFIT algorithm would undoubtedly improve if a way to include the correlations were found, the results obtained by factorizing the probability function are more than adequate for this thesis.

The probability functions were determined by studying the energy distributions of Monte Carlo photon showers. The CBALL Monte Carlo program, an adaptation of the EGS program[8,9] to the Crystal Ball geometry, was used to generate the showers. The EGS program incorporates almost all the physics involved in electromagnetic showers, and has been shown to reproduce accurately the effects of real showers. Nearly 100 sets of shower patterns were generated. Each set consists of 500 photon showers

with the energy and direction of the photons fixed. For a given energy, 16 sets of photon showers were generated by aiming the photons at the centroid of each of the 16 submodules of crystal number 25 (see section 3.2 for the definition of a submodule). Shower patterns were generated for energies of 50, 100, 200, 500, 1000, and 2000 MeV.

The Monte Carlo shower patterns can be used to determine an empirical form for the 13 factorized probability functions. The function f_i is just the probability of observing an energy E_i in crystal i for a particular combination of photon energy and direction. For a moment, consider a single set of Monte Carlo showers. The photons in the set have a fixed energy and direction, so f_i depends only on E_i. The function f_i is determined by the distribution of E_i obtained from a large number of showers. Thus, from each set of shower patterns, the function f_i can be found for the combination of photon energy and direction used to generate the patterns. The more general problem of determining f_i for an arbitrary photon energy and direction is just a matter of "interpolating" between shower sets.

To determine an explicit form for f_i, it is necessary to find a function which can be fit to the distribution of E_i. Ideally, this function will be simple and have a small number of parameters which can be adjusted to fit it to the E_i distribution for any combination of photon energy and direction. There are two cases which need to be distinguished: when the crystal i is a neighbor crystal and when it is the central crystal. Figure 39 shows a typical distribution of E_i for each

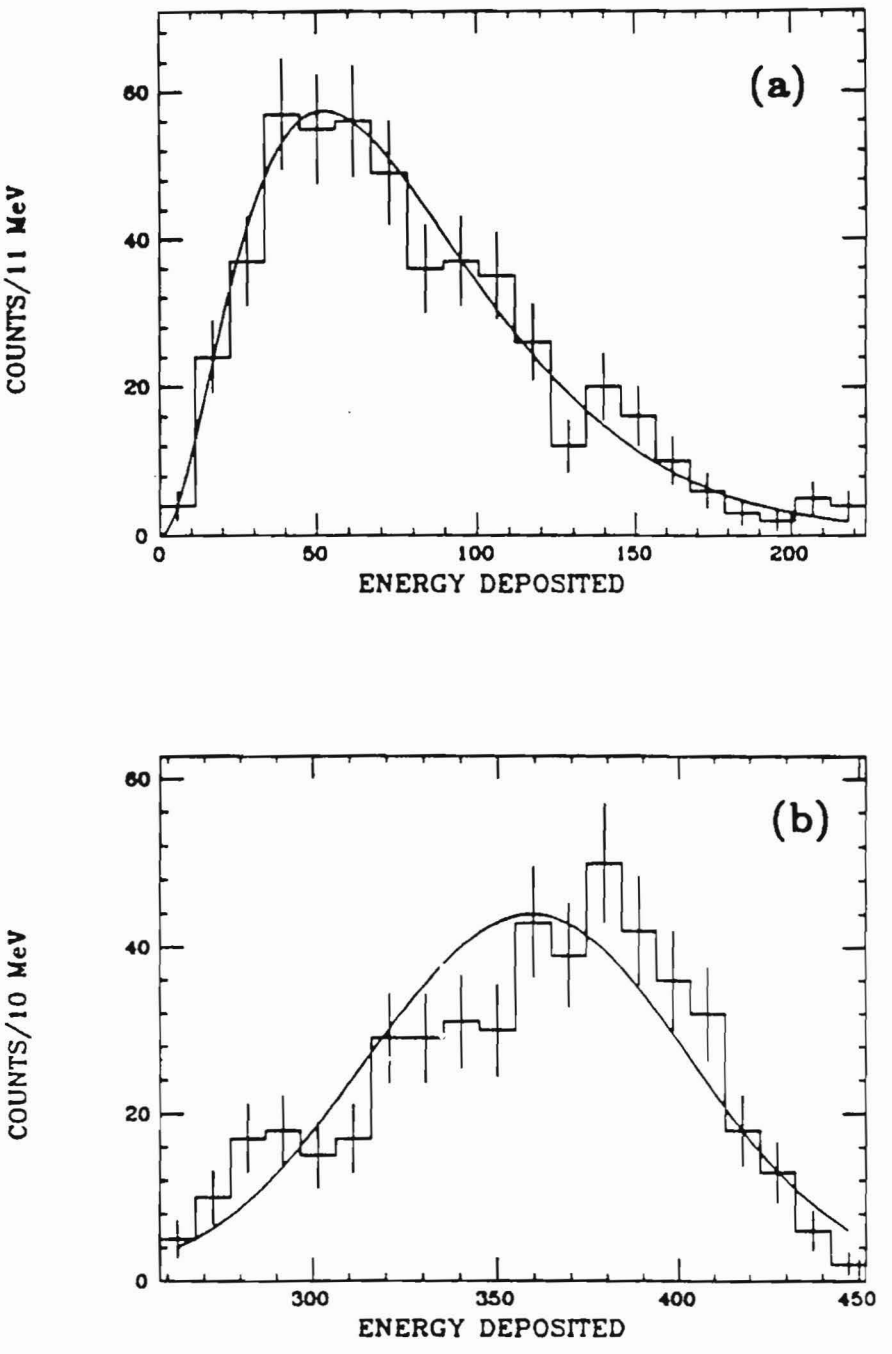

Figure 39: Crystal energy distributions for a 500 MeV photon.

(a) Distribution for a neighbor crystal; (b) Distribution for a central crystal. The solid lines shou the result of fitting the functional forms described in the text to the data.

case. When the crystal i is a neighbor crystal, the distribution of E_i is well represented by the following functional form:

$$f_i(E_i,\alpha,\beta) = \left[\frac{\beta^{\alpha+1}}{\Gamma(\alpha+1)}\right] E_i^{\alpha} \exp(-\beta E_i)$$

where $\alpha(E_\gamma,\theta_\gamma,\phi_\gamma)$ and $\beta(E_\gamma,\theta_\gamma,\phi_\gamma)$ are to be determined. When the crystal i is the central crystal, the distribution of E_i is adequately represented by a Gaussian:

$$f_i(E_i,\bar{E},\sigma) = \frac{1}{\sqrt{2\pi\sigma^2}} \exp\left[\frac{-(E_i-\bar{E})^2}{2\sigma^2}\right]$$

where $\bar{E}(E_\gamma,\theta_\gamma,\phi_\gamma)$ and $\sigma(E_\gamma,\theta_\gamma,\phi_\gamma)$ also need to be determined. These forms for f_i are normalized to unit probability:

$$\int f_i(E_i,\alpha,\beta)dE_i = 1$$

$$\int f_i(E_i,\bar{E},\sigma)dE_i = 1.$$

First consider the case when crystal i is a neighbor crystal. To simplify the discussion, the following results are for photons with an energy of 500 MeV; similar results are obtained for other photon energies. For a given shower set and neighbor crystal, the above function was fit to a histogram of the E_i distribution to obtain values for α and β. This was done for each of the 16 photon directions and each of the 12 neighbor crystals, giving a total of 192 fits. These fits have an average χ^2 of 23.9 for 18 degrees of freedom. Examining each of the 192 fits shows that the is a good representation of the Monte Carlo distributions. The fact that the χ^2/DOF is somewhat greater than 1 is partly due to each plot having a few bins with a very small number of events, causing the χ^2 to be overestimated.

Having determined 192 values for α and β, it is now desirable to find how these values depend on the direction of the photon. It is reasonable that α and β will depend on δ, the angle between the photon and the centroid of the crystal where the energy is deposited. Figures 40 and 41 show scatterplots of β and α versus $(1-\cos\delta)$. These figures show that beta is strongly correlated with $(1-\cos\delta)$, while α appears to correlated with $\ln(1-\cos\delta)$. On the basis of these plots, we will assume that α and β are given by

$$\alpha = \alpha_S \ln(1-\cos\delta) + \alpha_I$$

$$\beta = \mathrm{MAX}[\beta_S(1-\cos\delta) + \beta_I, \beta_H].$$

Only five parameters establish the dependence of f_i on the photon direction: α_S, α_I, β_S, β_I, and β_H. These parameters are determined by a simultaneous fit of the factorized probability function to the 192 different distributions of E_i for a given photon energy. The results for several different photon energies are given in table 7.

For the most part, the 192 distributions are well fit by this form for α and β. Since 3840 data points are being fit using only 5 parameters, it is not surprising that a few distributions give very poor fits. Figure 42 shows a typical fit and a very poor fit. The poor fits illustrate that α and β must also depend on other variables besides δ. Nevertheless, the present approach does a good job of describing the overall behavior of photon showers.

So far, only photons of various fixed energies have been considered. To determine α and β, and thus f_i, for an arbitrary photon energy, it is necessary to interpolate between energies in table 7 to arrive at values for α_S, α_I, β_S, β_I, and β_H. The function f_i for a neighbor crystal has now been completely specified.

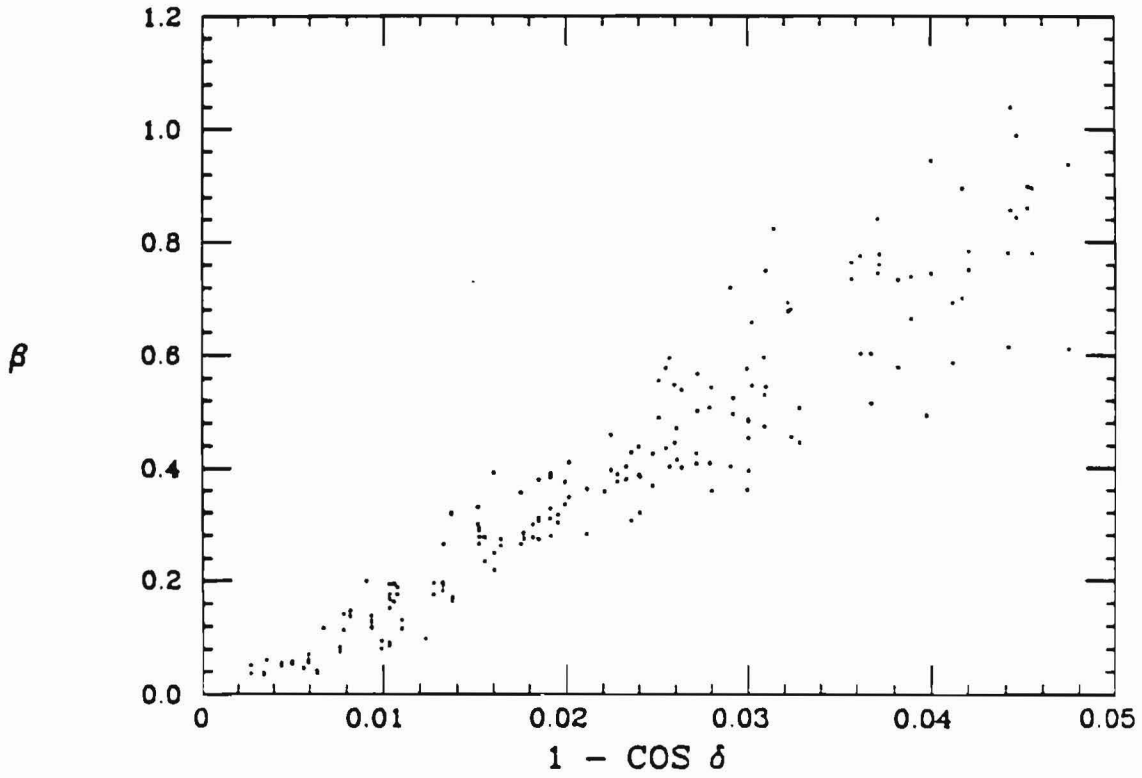

Figure 40: Scatterplot of B vs (1-cosδ).

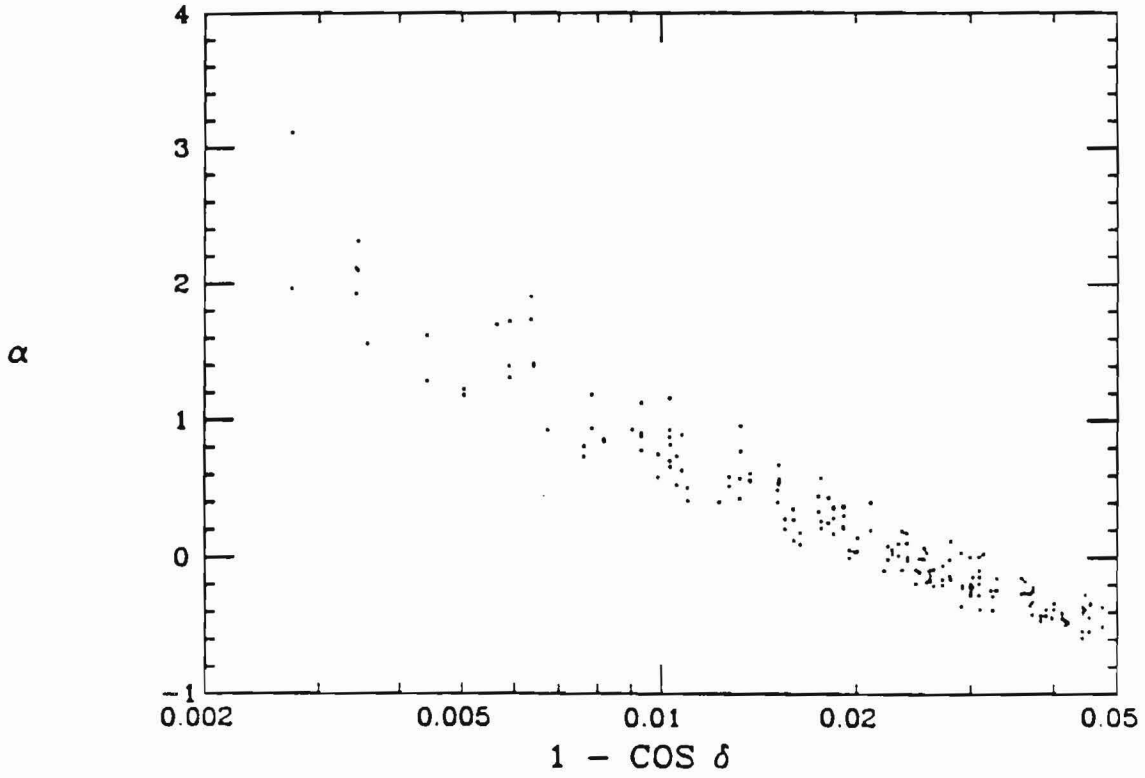

Figure 41: Scatterplot of α vs (1-cosδ).

TABLE 7

PIFIT Parameters for Several Different Energies

E_γ (MeV)	α_S	α_I	β_S (MeV^{-1})	β_I (MeV^{-1})	β_M (MeV^{-1})	$\bar{E}_S$	σ_S
100	-0.31	-1.9	23.8	-0.01	0.01	0.95	2.26
200	-0.38	-1.9	26.6	-0.10	0.04	0.96	1.88
500	-0.79	-2.9	24.6	-0.12	0.04	0.99	1.31
1000	-1.35	-4.2	20.2	-0.09	0.04	1.00	1.00
2000	-1.94	-5.4	15.8	-0.08	0.02	1.01	0.72

A similar approach is used to determine f_i for the central crystal. For a given photon energy and direction, a Gaussian was fit to a histogram of the energy E_i. This resulted in 16 values of $\bar{E}$ and σ for each energy. For 500 MeV photons, the average x^2 for the fits was 36 for 18 degrees of freedom. The symmetric form of the Gaussian does not properly account for a low energy tail on the E_i distribution, which is most noticeable for low energy photons. This is not a serious problem, but does explain the rather large x^2 for some of the fits. It was found that $\bar{E}$ was dependent on both δ, the angle between the photon direction and the centroid of the central crystal, and also on how close the photon was to the edge of the crystal. The latter quantity was parameterized by the quantity R, which is defined to be the angle between the photon direction and the nearest edge of the crystal divided by the

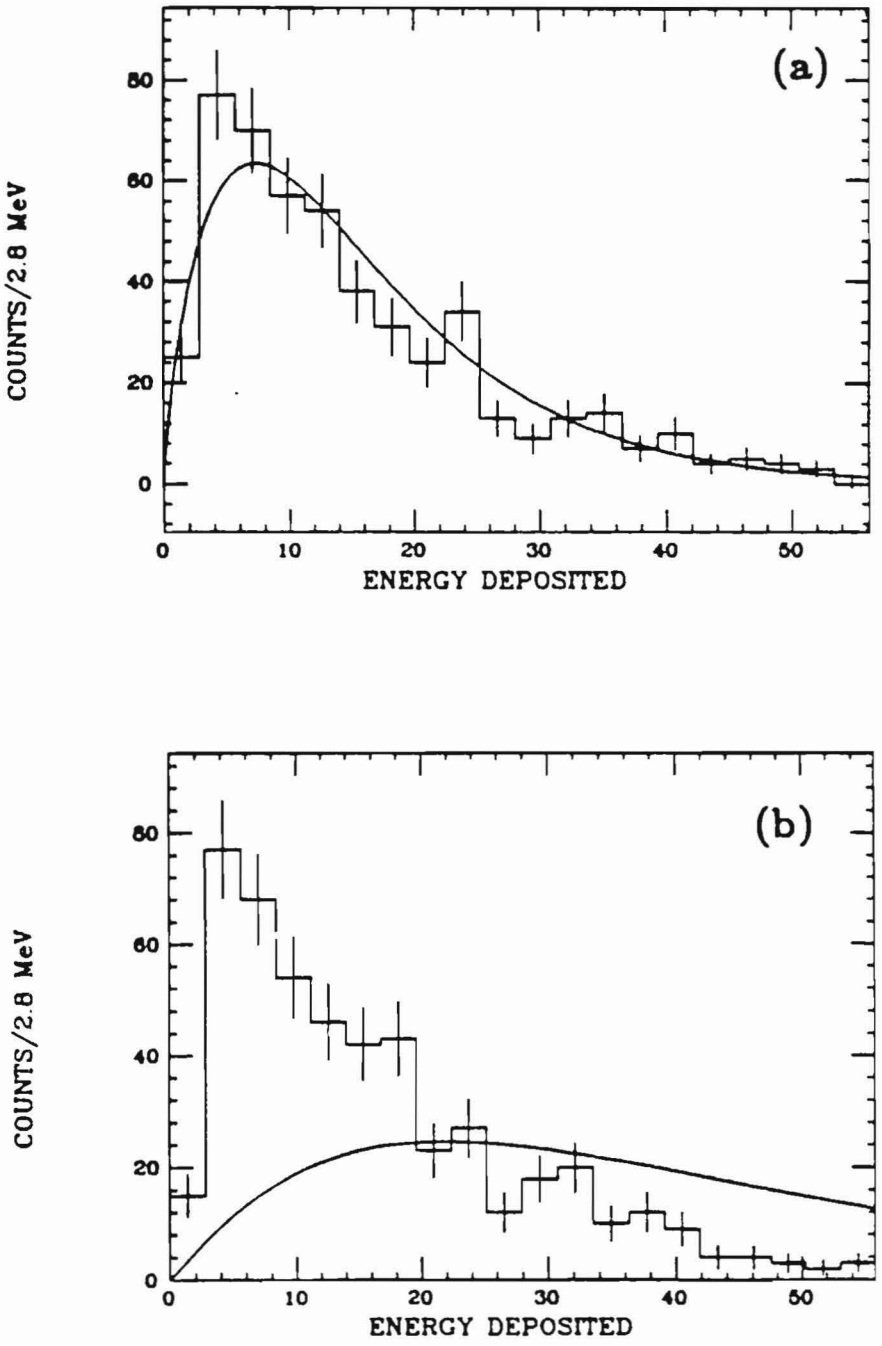

Figure 42: Fits to E_i distributions of neighbor crystals.

(a) A typical fit; (b) a poor fit.

angle between the centroid and the edge. The dependence of $\bar{E}$ on δ and R was consistent with the following form:

$$\bar{E} = \bar{E}_S E_\gamma [.86 - 40(1-\cos\delta) - .02/R]$$

where $\bar{E}_S$ is a scale factor dependent on the photon energy. The width of the Gaussian was found to have a linear relationship to the mean:

$$\sigma = \sigma_S [.204 E_\gamma - .2\bar{E}]$$

where σ_S depends on the photon energy. The values of $\bar{E}_S$ and σ_S for several different photon energies are given in table 7. For an arbitrary energy, $\bar{E}_S$ and σ_S are found by interpolation. The factorized probability function is now completely specified for all 13 crystals in a shower pattern.

Once the probability function is determined, estimating the direction of a photon is straightforward. The energy of the photon is well measured by summing the energy of the central crystal and its neighbors:

$$E_\gamma = \sum_i E_i .$$

The direction of the photon is estimated by finding the direction with the highest probability for the observed pattern. This is done by minimizing the quantity LL:

$$LL \equiv -2 \sum_i \ln(f_i)/NXTAL$$

where NXTAL is the number of crystals being summed over (13 for a single photon). The minimization is done using a simplex method, which has the advantage of not requiring any derivatives. The starting value for the photon direction is taken to be the centroid of the central crystal. The accuracy of this method can be estimated from samples of Monte Carlo photons. The angular resolution in the polar angle, σ_θ, is shown in table 8 for various photon energies (the angular resolution in ϕ is

given by $\sigma_\phi = \sigma_\theta / \sin\theta$). These results show that the photon angular resolution decreases as the energy increases, which reflects the fact that shower fluctuations become less significant at higher energies. An independent determination of the angular resolution using Bhabha events gave good agreement with the Monte Carlo estimates.

TABLE 8

Angular Resolution for Single Photons

E_γ (MeV)	σ_θ (mrad)
100	31
200	26
500	19
1000	16
1500	12
2000	10

The algorithm developed above can also be applied to the situation where the energy deposits are due to two photons with overlapping shower patterns. In this case, there are two central crystals and up to 24 neighbor crystals. Since each crystal can receive energy from both photons, it is necessary to define a new probability function which is the convolution of the single photon probability functions for each of the photons. If g_i is the factorized probability function for having an energy E_i in crystal i when γ_1 has an energy E_1 and direction θ_1, ϕ_1,

and γ_2 has an energy E_2 and direction θ_2, ϕ_2, then

$$g_i(E_i,E_1,E_2,\theta_1,\theta_2,\phi_1,\phi_2) = \int_0^{E_i} f_i(E,E_1,\theta_1,\phi_1)f_i(E_i-E,E_2,\theta_2,\phi_2)dE$$

where f_i is the single photon probability function from above.[69] The two-photon fit can be done in much the same way as the single photon fit. The direction of both photons and the ratio E_1/E_2 are allowed to vary, while the sum E_1+E_2 is fixed at the sum of the energy in the central crystals and all their neighbors. The definition of LL is changed to use the convoluted probability functions, g_i, instead of the single photon functions. Minimizing LL gives estimates for the energies and directions of the photons. From this information, the mass of the two photons can be computed and compared to the π^0 mass. Figure 43 shows the mass distribution for a set of 1000 MeV photons and a set of 1000 MeV π^0s generated using the CBALL Monte Carlo. There is nearly complete separation between the photon sample and the π^0 sample when the connected region energy is less than 2 GeV. Table 9 shows the angular and mass resolutions for Monte Carlo π^0s reconstructed by PIFIT as a function of the π^0 energy.

An empirical fit to the PIFIT mass resolution for merged π^0s gives

$$\sigma_M(\text{MeV}) = 6 + E_{\pi^0}(\text{MeV})/100$$

where σ_M is the mass resolution for merged π^0s and E_{π^0} is the π^0 energy.

TABLE 9

Angular and Mass Resolutions for Merged π^0s

E_{π^0} (MeV)	σ_θ (mrad)	σ_M (MeV)
750	19	13
1000	17	16
1500	16	20
1750	16	23
2000	16	27

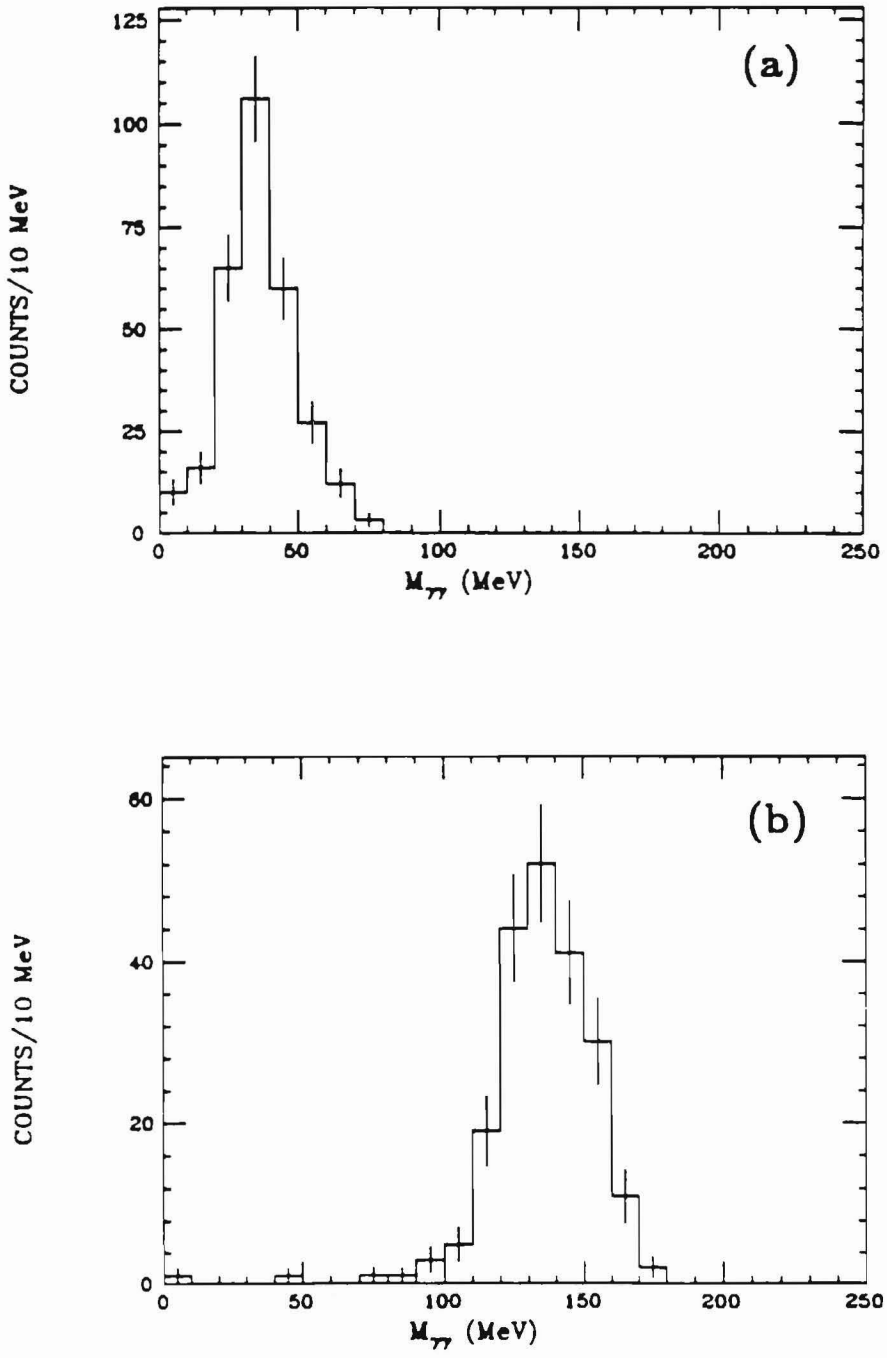

Figure 43: Mass distributions from PIFIT for photon and π^0 samples

(a) Mass distribution for a sample of Monte Carlo photons; (b) mass distribution for a sample of Monte Carlo π^0s.

Appendix B

A MODEL FOR SIMULATING D MESON DECAY

This appendix describes a model that was used to simulate the decay of D^0 and D^+ mesons in the Crystal Ball detector. Such simulations played an important role in determining the detection efficiency for many of the processes studied in this thesis.

There are three different types of D meson decays:

(1) Hadronic decays - These decays have final states composed entirely of hadrons.

(2) Semileptonic decays - These decays have final states composed of a lepton, an antineutrino, and one or more hadrons.

(3) Leptonic decays (D^+ only) - These decays have final states composed of a lepton and an antineutrino.

The leptonic decay modes are expected to have branching ratios much less than 1%, and were not included in the model.

The first decision the model must make is whether to generate a hadronic decay or a semileptonic decay. The total semileptonic branching ratio was taken to be 0.1 for the D^0 meson and 0.4 for the D^+ meson. These branching ratios were based on measurements made by previous experiments.[20,21] Once the type of decay was chosen, a specific final state was chosen using the branching fractions given below, and the kinematics of the final state were determined by a phase space Monte Carlo.[70]

Most of the D^0 decays and a majority of the D^+ decays are hadronic decays. Since the D mesons can decay into many different hadronic final states, only a few of which have well-measured branching ratios, a theoretical model was used to predict the branching fractions for the hadronic decay modes. The model used in this thesis is the constant matrix element model.[71] This model starts out with the sextet dominance predictions for the relative rates to a pair of pseudoscalers (see section 6.2), includes a constant factor in the matrix element for each additional π meson in the final state, and uses a statistical averaging over the possible isospin states to determine the relative rates for the different charge states. Cabibbo-suppressed decays were ignored in the model. The hadronic branching fractions are given in table 10.

The semileptonic branching fractions were determined in an ad-hoc manner, where emphasis was placed on low multiplicity final states. The semileptonic branching fractions are given in table 11. Note that the symbol ℓ^+ is used in table 11 to denote a lepton, with equal weight given to choosing a muon or an electron.

As a cross check of the model, the charge multiplicity distributions generated by the model were compared with measurements made by previous experiments.[20,72] The model was found to be in good agreement with the measured multiplicity distributions. The dependence of the efficiencies on the branching fractions used in the model was studied and included in the systematic error for each efficiency.

TABLE 10

Hadronic Branching Fractions Used in the Monte Carlo

D^0		D^+	
Decay Mode	Branching Fraction (%)	Decay Mode	Branching Fraction (%)
$K^-\pi^+$	5	$\bar{K}^0\pi^+$	12
$\bar{K}^0\pi^0$	5	$K^-\pi^+\pi^+$	17
$\bar{K}^0\pi^+\pi^-$	17	$\bar{K}^0\pi^0\pi^+$	26
$K^-\pi^+\pi^0$	15	$\bar{K}^0\pi^+\pi^+\pi^-$	14
$\bar{K}^0\pi^0\pi^0$	6	$K^-\pi^+\pi^+\pi^0$	11
$K^-\pi^+\pi^+\pi^-$	8	$\bar{K}^0\pi^+\pi^0\pi^0$	10
$\bar{K}^0\pi^+\pi^-\pi^0$	15	$K^-\pi^+\pi^+\pi^+\pi^-$	2
$K^-\pi^+\pi^0\pi^0$	6	$\bar{K}^0\pi^+\pi^+\pi^-\pi^0$	4
$\bar{K}^0\pi^0\pi^0\pi^0$	2	$K^-\pi^+\pi^+\pi^0\pi^0$	2
$\bar{K}^0\pi^+\pi^+\pi^-\pi^-$	2	$\bar{K}^0\pi^+\pi^0\pi^0\pi^0$	1
$K^-\pi^+\pi^+\pi^-\pi^0$	3	$K\pi\pi\pi\pi\pi$	1
$\bar{K}^0\pi^+\pi^-\pi^0\pi^0$	3		
$K^-\pi^+\pi^0\pi^0\pi^0$	1		
$K\pi\pi\pi\pi\pi$	0.7		
$\bar{K}^0\eta$	1		
$K^-\pi^+\eta$	1		
$\bar{K}^0\pi^0\eta$	1		
$K\pi\pi\pi\eta$	0.6		
$\bar{K}^0\eta'$	6		
$K^-\pi^+\eta'$	1		
$\bar{K}^0\pi^0\eta'$	1		

TABLE 11

Semileptonic Branching Fractions Used in the Monte Carlo

D^0		D^+	
Decay Mode	Branching Fraction (%)	Decay Mode	Branching Fraction (%)
$K^-\ell^+\bar{\nu}_\ell$	45	$\bar{K}^0\ell^+\bar{\nu}_\ell$	45
$K^-\pi^0\ell^+\bar{\nu}_\ell$	20	$K^-\pi^+\ell^+\bar{\nu}_\ell$	20
$\bar{K}^0\pi^-\ell^+\bar{\nu}_\ell$	20	$\bar{K}^0\pi^0\ell^+\bar{\nu}_\ell$	20
$K^-\pi^+\pi^-\ell^+\bar{\nu}_\ell$	5	$\bar{K}^0\pi^+\pi^-\ell^+\bar{\nu}_\ell$	5
$\bar{K}^0\pi^-\pi^0\ell^+\bar{\nu}_\ell$	5	$K^-\pi^+\pi^0\ell^+\bar{\nu}_\ell$	5
$K^-\pi^0\pi^0\ell^+\bar{\nu}_\ell$	5	$\bar{K}^0\pi^0\pi^0\ell^+\bar{\nu}_\ell$	5

REFERENCES

1. J. J. Aubert *et al.*, Phys. Rev. Lett. **33**, 1404 (1974); J.-E. Augustin *et al.*, Phys. Rev. Lett. **33**, 1406 (1974).
2. G. S. Abrams *et al.*, Phys. Rev. Lett. **33**, 1453 (1974).
3. W. Braunschweig *et al.*, Phys. Lett. **57B**, 407 (1975).
4. W. Tanenbaum *et al.*, Phys. Rev. Lett. **35**, 1323 (1975).
5. G. J. Feldman *et al.*, Phys. Rev. Lett. **35**, 821 (1975).
6. R. Partridge *et al.*, Phys. Rev. Lett. **45**, 1150 (1980); T. M. Himel *et al.*, Phys. Rev. Lett. **45**, 1146 (1980).
7. C. Edwards *et al.*, Phys. Rev. Lett. **48**, 70 (1982).
8. J. E. Gaiser, Unpublished Ph.D. thesis, Stanford University, 1983.
9. T. Appelquist and H. D. Politzer, Phys. Rev. Lett. **34**, 43 (1975); A. De Rújula and S. L. Glashow, Phys. Rev. Lett. **34**, 46 (1975).
10. B. J. Bjorken and S. L. Glashow, Phys. Lett. **11**, 255 (1964); S. L. Glashow, J. Iliopoulos, and L. Maiani, Phys. Rev. D **2**, 1285 (1970).
11. T. Appelquist, A. De Rújula, H. D. Politzer, and S. L. Glashow, Phys. Rev. Lett. **34**, 365 (1975); E. Eichten, K. Gottfried, T. Kinoshita, J. Kogut, K. D. Lane, and T.-M. Yan, Phys. Rev. Lett. **34**, 369 (1975).
12. Mary K. Gaillard, Benjamin W. Lee, and Jonathan L. Rosner, Rev. Mod. Phys. **47**, 277 (1975).
13. S. Okubo, Phys. Lett. **5**, 165 (1963); G. Zweig, unpublished work (1964); J. Iizuka, Suppl. Prog. Theor. Phys. **37-38**, 21 (1966).

14. G. Goldhaber et al., Phys. Rev. Lett. 37, 255 (1976); I. Peruzzi et al., Phys. Rev. Lett. 37, 569 (1976).

15. P. A. Rapidis et al., Phys. Rev. Lett. 39, 526 (1977); W. Bacino et al., Phys. Rev. Lett. 40, 671 (1978); R. H. Schindler et al., Phys. Rev. D 21, 2716 (1980).

16. J. Siegrist et al., Phys. Rev. Lett. 36, 700 (1976); J. Burmester et al., Phys. Lett. 66B, 395 (1977); R. Brandelik et al., Phys. Lett. 76B, 361 (1978).

17. E. Eichten, K. Gottfried, T. Kinoshita, K. D. Lane, and T.-M. Yan, Phys. Rev. D 17, 3090 (1978); E. Eichten, K. Gottfried, T. Kinoshita, K. D. Lane, and T.-M. Yan, Phys. Rev. D 21, 203 (1980).

18. A detailed comparison of theory and experiment is given by John E. Gaiser in Proceedings of the XVIIth Rencontre de Moriond, Les Arcs (1982).

19. V. A. Novikov, L. B. Okun, M. A. Shifman, A. I. Vainshtein, M. B. Voloshin, and V. I. Zakharov, Phys. Rep. 41C, 1 (1978).

20. M. Piccolo et al., Phys. Lett. 70B, 260 (1977); I. Peruzzi et al., Phys. Rev. Lett. 39, 1301 (1977); D. L. Scharre et al., Phys. Rev. Lett. 40, 74 (1978); G. S. Abrams et al., Phys. Rev. Lett. 43, 481 (1979); R. H. Schindler et al., Phys. Rev. D 24, 78 (1981).

21. R. Brandelik et al., Phys. Lett. 70B, 387 (1977); J. M. Feller et al., Phys. Rev. Lett. 40, 274 (1978); W. Bacino et al., Phys. Rev. Lett. 43, 1073 (1979); W. Bacino et al., Phys. Rev. Lett. 45, 329 (1980).

22. M. Sands, SLAC Report No. 121, 1970.

23. There is an indication that the energy scale of SPEAR may be ≈2 MeV low at the ψ'' (see A. A. Zholentz, et al., Phys. Lett. 96B,

214 (1980)). Such a shift in the energy scale would not significantly alter any of the results from this experiment.

24. A thorough discussion of the scintillation process can be found in J. B. Birks, The Theory and Practice of Scintillation Counting (Pergammon Press Ltd., Oxford, 1967).

25. Y. Chan et al., IEEE Trans. Nucl. Sci. 25, 333 (1978).

26. G. I. Kirkbride et al., IEEE Trans. Nucl. Sci. 26, 1535 (1979).

27. The crystals which lie at the vertices of major triangles have only 11 neighbors.

28. R. Horisberger and B. Pollock, Crystal Ball Note (unpublished) and private communication.

29. A. D. Liberman and F. Bulos, Crystal Ball Note 127 (unpublished).

30. The angular resolution is 40 mrad for low energy photons (E_γ<100 MeV) and 25 mrad for high energy photons (E_γ>1000 MeV). For intermediate energies, a linear interpolation is made. The resolution in theta is somewhat worse if the z coordinate of the interaction point is not measured for the event. See Mark Oreglia, Unpublished Ph.D. thesis, Stanford University, 1981.

31. Bill Lockman, Crystal Ball Note 157 (unpublished).

32. The hadron selection cuts are the same as the cuts in ref. 31 except that the QED cut is relaxed slightly and the charged particle requirement is dropped. These changes remove a potential bias against ψ'' events when there is a decay of a D^0 into an all neutral final state.

33. In principle, a fourth parameter is necessary: the partial width for the decay of the resonance to hadrons, Γ_{had}. It is assumed that non-hadronic decays of the ψ'' are so small that $\Gamma_{had}=\Gamma_{tot}$.

An example of a non-hadronic decay is $\psi'' \to e^+e^-$, which has a branching ratio of approximately 10^{-5}.

34. The uncertainty in this probability is dominated by the changes which occur under different assumptions for the branching ratios to the unmeasured τ decay modes (only $\approx$20% of the τ branching fraction is into unmeasured decay modes).

35. The non-charm term will also have a small contribution from two photon, cosmic ray, and beam-gas events which manage to survive the hadron selection cuts. The contribution to R from these residual events is expected to be nearly constant over the energy range of the data.

36. Particle Data Group, Phys. Lett. 111B (1982).

37. John M. Blatt and Victor F. Weisskopf, Theoretical Nuclear Physics (Wiley, New York, 1952), pp. 311-441.

38. This value of the radius of interaction is similar to the value determined by Angela Barbaro-Galtieri, in Advances in Particle Physics, edited by R. L. Cool and R. E. Marshak (Wiley, New York, 1968), vol. 2, pp. 197-199.

39. G. Bonneau and F. Martin, Nucl. Phys. B27, 381 (1971); J. D. Jackson and D. L. Scharre, Nucl. Instrum. Methods 128, 13 (1975).

40. In principle, the radiative corrections to the non-charm term have contributions from very low center of mass energies where the efficiency falls off. However, these effects will merely change the non-charm contribution by a constant factor which is absorbed into the magnitude of the non-charm term.

41. John Gaiser, Crystal Ball Note 132 (unpublished).

42. The Delco and Lead Glass Wall experiments have not published meas-

urements of the ψ'' cross section. The values given for these experiments are estimates based upon the published data.

43. The radiative photon will be monochromatic only if the charmonium states are narrow relative to the detector resolution.

44. The transition rates to the χ states were obtained by correcting the rates in reference 11 (E. Eichten et al.) for the known mass differences. Since the 1^1D_2 state has not yet been observed, it is not known whether it lies above or below the ψ''. The transition rate to this state was calculated under the assumption that the 1^1D_2 state lies 100 MeV below the ψ''. The transition rates to the η_c and η_c' states are expected to be very small because the transition requires $\Delta L=2$.

45. The errors in the recoil masses do not include the ±4 MeV uncertainty in the SPEAR energy calibration.

46. The photon energy is mismeasured when another track deposits energy in one or more of the 13 crystals used to calculate the photon energy. If this extraneous energy is large compared to the photon energy resolution, the photon will no longer lie in the peak and will not be counted by the fit.

47. The photon detection efficiencies used in this analysis are based upon the techniques and measurements of reference 8.

48. Richard L. Ford and Walter R. Nelson, SLAC Report No. 210, 1978.

49. This upper limit is based upon a small excess of events near 130 MeV. Although this excess may be due to doppler shifted transitions from radiatively produced ψ' events to the χ_2 state, the observed excess is a 2 standard deviation effect and is not statistically significant. Note that since only ≈30% of the hadron

events are ψ'' events, this upper limit corresponds to a 3% rate for all events, which is in good agreement with the earlier estimate of the experimental sensitivity.

50. Charm changing neutral currents could couple the charm quark to the up quark. For limits on the strength of this coupling, see F. Buccella and L. Oliver, Nucl. Phys. B162, 237 (1980).

51. Sheldon L. Glashow, Nucl. Phys. 22, 579 (1961); Steven Weinberg, Phys. Rev. Lett. 19, 1264 (1967); Abdus Salam, in Elementary Particle Theory, Proceedings of the Eighth Nobel Symposium, edited by Nils Svartholm (Almqvist & Wiksell, Stockholm, 1968), p. 367.

52. Makoto Kobayashi and Toshihide Maskawa, Prog. Theor. Phys. 49, 652 (1973).

53. E. Fernandez et al., Phys. Rev. Lett. 51, 1022 (1983); N. S. Lockyer et al., Phys. Rev. Lett. 51, 1316 (1983).

54. K. Kleinknecht and B. Renk, Phys. Lett. 130B, 459 (1983).

55. A further complication in understanding the hadronic decay modes is the possibility of final state interactions. See, for example, John F. Donoghue and Barry R. Holstein, Phys. Rev. D21, 1334 (1980).

56. R. L. Kingsley, S. B. Treimain, F. Wilczek, and A. Zee, Phys. Rev. D11, 1919 (1975); Martin B. Einhorn and C. Quigg, Phys. Rev. D12, 2015 (1975).

57. Harald Fritzsch and Peter Minkowski, Phys. Lett. 90B, 455 (1980).

58. G. Altarelli and L. Maiani, Phys. Lett. 52B, 351 (1974); M. K. Gaillard and Benjamin W. Lee, Phys. Rev. Lett. 33, 108 (1974); G. Altarelli, N. Cabibbo, and L. Maiani, Nucl. Phys. B88, 285 (1975).

59. Harry J. Lipkin, Phys. Rev. Lett. 46, 1307 (1981).

60. The opening angle error was obtained by adding in quadrature the angular resolutions for the photons, taken in the γ-γ plane.

61. The merged π^0s were not kinematically fit to the π^0 hypothesis because the photons reconstructed by PIFIT have large and unknown correlations in the error matrix.

62. The D^0 mass is from measurements made at SPEAR,[20] which eliminates any error in the D^0 momentum due to the uncertainty in the SPEAR beam energy.

63. Milton Abramowitz and Irene A. Stegun, editors, Handbook of Mathematical Functions (Dover, New York, 1972), pp. 940-941.

64. This analysis of the decay $\chi_0 \to \pi^0\pi^0$ is intended only to be an illustration. A detailed study of this decay is in progress (Roger Lee, private communication).

65. Roger Lee, private communication.

66. The Mark II experiment has measured $\sigma_{D^0} \cdot BR(D^0 \to K^-\pi^+)$ to be 0.24±0.02 nb for the same center of mass energy as this experiment. See reference 20 (R. H. Schindler et al.).

67. The limit for $D^0 \to \bar{K}^0\pi^0$ obtained by the Lead Glass Wall experiment (reference 20, D. L. Scharre et al.) was listed under the Mark I column. Although the collaboration and detector configuration of the Lead Glass Wall experiment were somewhat different than the original Mark I experiment, the experiments were considered similar enough to be grouped together.

68. A Cabibbo angle given by $\sin\theta_C = 0.231$ was used to calculate the rates for Cabibbo-suppressed decay modes.

69. The convolution of probability functions is not done when a crystal is a central crystal for one photon and a neighbor crystal for

the other. In this case, the probability function is taken to be the central crystal probability function. This is expected to be a good approximation for all situations where identifying both photons is feasible.

70. Jerry Friedman, SLAC Computation Group Technical Memo No. 145.

71. C. Quigg and Jonathan L. Rosner, Phys. Rev. D17, 239 (1978).

72. V. Vuillemin et. al., Phys. Rev. Lett. 41, 1149 (1978).